MECHANICS OF NANOSCALE FIBER NETWORKS AND THEIR COMPOSITES: A THREE-DIMENSIONAL MULTISCALE STOCHASTIC MODELLING STUDY

by

RAJNI CHAHAL

Presented to the Faculty of the Graduate School of
The University of Texas at Arlington in Partial Fulfillment
of the Requirements
for the Degree of

DOCTOR OF PHILOSOPHY

THE UNIVERSITY OF TEXAS AT ARLINGTON
December 2020

Copyright © by Rajni Chahal 2020

All Rights Reserved

To Bhapa & Bibi, my late grandparents

ACKNOWLEDGEMENTS

I would like to express my gratitude to Dr. Ashfaq Adnan for his encouragement and understanding on multiple levels as an advisor. His belief in me kept setting new goals for me that I worked towards, failed at, and hopefully achieved throughout my PhD. I must thank him to set me free to invest my time in interning at Idaho National Laboratory (INL) and embarking upon glider pilot training. I would also like to thank my committee members: Dr. Rassel Raihan, Dr. Ye Cao, Dr. Kent Lawrence, and Dr. Kamesh Subbarao for investing their time in reviewing my work and providing valuable suggestions. I am thankful to Dr. Gorakh Pawar and Dr. Bjorn Vaagensmith from INL, who allowed me to add the research performed at INL in my PhD dissertation and have given me an opportunity to work as a part of their team and providing funding. I will thank Dr. Terry Ring and Dr. Jesse Reeves for being part of the INL-UTA meetings and for their valuable comments. Thanks to UTA MAE department for Enhanced Graduate Teaching Assistant funding and Dr. Reifsnider for encouragement, Abaqus access and computing resources.

I will thank a stranger from YouTube, Dr. Lucy Kissick, for sharing her experiences and ‘behind-the-scenes’ struggles in a PhD that are usually overshadowed by success stories. I am grateful to Mohit, my friends at UTA, abroad, MMPL lab members and SGI-Buddhist group for their support. Thanks to Dr. Vamsee Vadlamudi for helping with Abaqus. I am inspired by my glider instructor, Mr. Eric Anderson, learning from whom has broadened my perspective and has made me a better researcher.

Most of all, I am grateful and forever indebted to my parents, brother, and sisters for always blessing, entrusting, and investing in my dreams. Finally, I would like to remember my late grandparents today, who I know have prayed for, worked for, and dreamed of this day and much more for me.

November 30, 2020

For all your days prepare

And meet them ever alike

When you are the anvil — bear

When you are the hammer — strike

(Dr. A.P.J. Abdul Kalam)

ABSTRACT

MECHANICS OF NANOSCALE FIBER NETWORKS AND THEIR COMPOSITES: A THREE-DIMENSIONAL MULTISCALE STOCHASTIC MODELLING STUDY

Rajni Chahal, PhD

The University of Texas at Arlington, 2020

Supervising Professor: Ashfaq Adnan

Three-dimensional fiber networks and their composites are commonly observed as bird nests in nature, collagen in biological systems, papers, respiratory face masks filters, water filter cartridges, and air purification meshes, etc. The overall properties and mechanics of fiber networks are governed by the morphological parameters such as fiber length, diameter, orientation, waviness, agglomeration, and inter-fiber interactions. In this study, two different fiber network systems: electro spun silica nanofiber mats (stand-alone networks) and carbon nanotube (CNT) reinforced nanocomposites (network-based composites) are considered. Most of the available literature assumes idealized network parameters, perfect interphase, and two-dimensional modelling approaches. In this study, we have proposed a novel computational modelling approach which can incorporate above-mentioned parameters and their stochastic variations towards the construction of a three-dimensional model. The modeling scheme involves molecular dynamics simulation to evaluate component level and interfacial properties, and finite element analysis to obtain network level properties. The stochastic nature of the network has been modeled with a Python-based scheme. Future guidelines to enhance current modelling technique to study the failure properties of these materials are discussed.

Table of Contents

List of Illustrations

List of Tables

CHAPTER 1 INTRODUCTION

Background

Fibrous networks are found everywhere. They are commonly observed as bird nests in nature, collagen in biological systems, papers, respiratory face masks filters, water filter cartridges, and air purification meshes, etc. The overall properties and mechanics of fiber networks are governed by the morphological parameters such as fiber length, diameter, orientation, waviness, agglomeration, and inter-fiber interactions. Electrospun silica nanofiber mat is an example of such stand-alone fibrous mats, where the porosity/inter-fiber distance and above-mentioned parameters can be used to tune their overall properties.

In network-based composites, the network of fibrous material is embedded inside a matrix medium and enhance the properties of overall composite. For instance, the polymer matrices are not electrically conductive; but when a ‘percolated’ network of carbon nanotube (CNT) bundles is inserted into the polymer, the resulting composite material shows high electrical conductivity. In a similar fashion, the thermal conductivity of a polymer-based composite is achieved. Furthermore, due to remarkable mechanical properties of CNTs, more load can be withstood by CNTs when embedded in the comparatively less stiff and less strong polymer material. Several other studies report the enhancement in piezo resistivity [1][2][3], structural damping [4][5] properties of CNT reinforced polymer materials. As mentioned earlier, as CNT networks are embedded in a matrix medium, their mechanical properties are also influenced by CNT-matrix interfacial properties [6].

In this study, two different fiber network systems: electro spun silica nanofiber mats (stand-alone networks) and CNT reinforced nanocomposites (network-based composites) are considered.

Most of the available literature assumes idealized network parameters, perfect interphase, and two-dimensional modelling approaches. In this study, we have proposed a unique Python-based modelling approach which can incorporate above-mentioned parameters and their stochastic variations towards the construction of a three-dimensional network model, which is later embedded in the epoxy matrix to represent CNT/epoxy nanocomposite. Three-phase model will be generated to account for the effect of variable *interphase* stiffness. To gain more insight, atomistic simulations are used to study the CNT/epoxy interfacial region. Future guidelines to enhance current modelling technique to account for CNT agglomeration and to study the failure properties of these materials are discussed.

Same Python algorithm is used to generate three-dimensional network of silica nanofibers. This proposed model is a multiscale model in the sense that the size-dependent mechanical properties of silica nanofiber (NF) are evaluated using Molecular Dynamics simulations to be input in the finite element model. Using molecular dynamics, the effect of interface formation between the fibers arranged at different configurations (aligned and junction model) will be studied. The effect of silanol formation on the nanofiber surface during hydroxylation will be evaluated using atomistic simulations. Size-dependent thermal stability of NFs is investigated. The multiscale three-dimensional network model will be enhanced by allowing fiber-fiber interactions based on the cut-off distance. Future guidelines to account for higher fiber volume fractions will be provided. Also, the inter-fiber interaction failure to account for local network failure leading to the overall network failure will be discussed.

Motivation

Carbon Nanotube Nanocomposites

Since the discovery of carbon nanotubes (CNTs) in 1991 [7], CNTs have become a popular reinforcement material for polymers. CNTs are the filler materials of nanoscale dimensions which when added to the polymer matrix form a strong yet light-weight multifunctional composite material. Polymer nanocomposites reinforced with CNTs have been fabricated and mechanically tested to investigate their potential as strong, and lightweight materials [8][9][10]. Owing to their excellent properties, CNT composites can find great applications in electronics [11], drug delivery [12], electromagnetic shielding [13], strong-yet-lightweight aerospace materials [10], etc. Thus, it becomes critical to evaluate their multifunctional properties before bringing them to the application.

It is a known fact that excellent properties of fibers do not necessarily translate into excellent properties of the composites. Previous studies found that the overall properties of the CNT composites are greatly influenced by the CNT-matrix interface properties [14][15][16] and CNT morphological parameters such as CNT orientation, dispersion, waviness, diameter, inter-CNT spacing, etc. [17][18][19][20].

Due to the multifunctional properties of CNTs, the CNT based composites hold various applications. A few of them are discussed in this section.

Rugged Electronics Interconnect materials

Typical electronics packages are assembled by integrating various parts on printed circuit boards (PCB). Traditional interconnect materials in electronics packages are not suitable for DoD electronics because in many DoD extremely transient conditions, mechanical failures of the whole packages invariably occur due to interconnect junction failures.

Due to their excellent mechanical, electrical, and thermal properties, Carbon nanotube reinforced polymer composites have been identified as potential candidate to replace the traditional materials.

Space Elevators

“Our dreams of everyday life in space and its promise for a better life on Earth are hostage to the high cost of space transportation”, a 2008 NASA fact sheet says. However, upon the invention of Carbon nanotubes in 1991, a hope for lower space transportation cost originated. It is derived by the imagination of a Russian rocket scientist Konstantin Tsiolkovsky in 1895 who dreamed about a giant ‘Space elevator’ extending for earth’s surface to its Geostationary orbit (**Fig. 1.1**).

The mechanical properties of carbon nanotubes ignited the hope among NASA scientists and US Department of energy (DOE) national laboratories to consider the possibility of Space elevators as future space transportation.

Despite of the posed risks in their functionality such as structural instability, space debris etc., it is exciting to know that such a structure can be built in the future with more research.

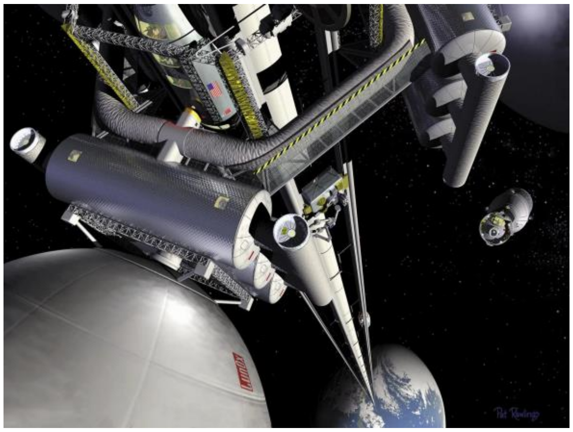

Fig. 1.1 *An Illustration of Space Elevator, NASA MSFC*[21]

Electromagnetic Interference (EMI) Shielding

Lightweight EMI shielding protects the workspace and sensitive circuits from radiations coming from computers and telecommunication equipment. It is especially important for the deep human space exploration mission, such as Mission to Mars, to protect the systems and the astronauts from the deadly carcinogenic radiations in the space.

CNT based composites also have shown their potential in the EMI shielding in the ranges of GHz.

Carbon Nanotube blankets for composites manufacturing and repair

As progress is still being made to more evenly distribute the CNTs with the use of dispersants, companies like Veelo have started investing into the non-structural applications of CNTs. Research is ongoing to use them in curing conventional composites using CNT blankets and utilizing their electrothermal properties towards the development of de-icing devices for aircrafts and drones.

The carbon-fiber reinforced and other composites are commonly used in aerospace industry. Conventionally, the aircraft components ranging from massive fuselages to tail fins have to be cured in warehouse-sized ovens or autoclaves during curing. In order to cure the components, both pressure and heat in the autoclave have to be controlled. During this, a large air volume around the components ends up being heated pointlessly, which adds up to the energy usage during composite curing. To put it into perspective, it might be interesting to know that the energy consumption involved in running the autoclaves and ovens is almost half as much as the cost of manufacturing a composite part. Thus, to lower down the manufacturing cost incurred during curing, Veelo in collaboration with Massachusetts Institute of Technology (MIT) is investing in developing a CNT-based heating blanket as an alternative to curing inside the autoclaves or ovens.

Such blankets can be put directly on the component that needs to be cured and hence resulting in heating only the selective area instead of heating up the entire oven volume. Because of excellent thermal conduction properties of CNTs, this process is estimated to need three orders of magnitude lesser energy compared to the conventional autoclaves.

Similarly, the smaller versions of these blankets can be used to re-cure the repaired area of the composite structure during maintenance. Currently, the lesser efficient and relatively ineffective metal wire-based blankets are used, which could be replaced by CNT-doped blankets in future.

Carbon nanotube as electrothermal de-icing devices

CNTs are under research to be used in next-generation de-icing devices built into aircraft wings and other potential ice-buildup surfaces. Currently, chemical sprays on the wings surfaces before takeoff and the electrically heated copper wire meshes under aircraft wings (used by Boeing 787) during in-flight are used to protect the aircraft against ice buildup. The copper wire meshes have disadvantages such as high weight and they are subjected to slow and uneven heating of the leading edges. CNT blankets are under research motivated by their low weight ratio and their ability to heat up about 10 times faster for a given area. Also, due to their enhanced electrothermal properties, they are estimated to use 10 times less energy compared to conventional de-icing devices. The energy saved can be crucial for battery-powered drones where saving this amount of energy can take it few extra miles. According to a recent article in AIAA magazine [22], these de-icing devices are under testing currently by U.S. Navy, Embraer, Collins Aerospace, etc.

Carbon nanotube outfitted sensors as damage sensing ‘spies’

CNTs have also shown promising results as sensors embedded within aircraft wings, that could be used as material health monitoring devices. It could register changes in a baseline level of electrical resistance, which might be caused by structural fatigue or damage during operation.

Electrospun Silica Nanofiber Mat

Silica nanofiber (NF) mat can be formed by electrospinning a fluid comprising a silica precursor and a polymer [23]. During this process, a portion of polymer from the electrospun fibers is removed leaving behind a stand-alone silica nanofiber mat. Upon annealing, individual nanofibers preserve an amorphous structure and the overall mat consists of a network of silica nanofibers bonded together. It might be noted that previously discussed morphological parameters such as NF length, diameter, waviness, orientation, dispersion, inter-fiber bonding, etc. can also be observed in an electrospun silica NF mat (**Fig. 1.2**). In addition, the mechanical properties of individual NFs of varied sizes also need to be investigated.

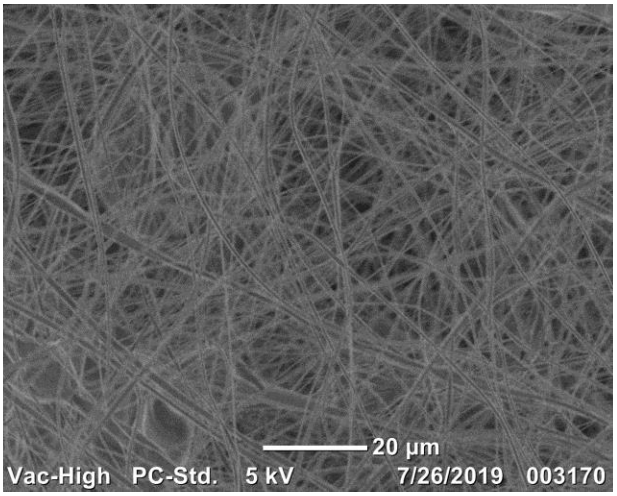

Fig. 1.2 *Scanning Electron Microscope (SEM) image of electrospun silica nanofiber mat*

These materials can find applications as high-voltage transformers insulator materials [23], optical fibers for telecommunications [24][25], etc. Power transformers are crucial components of an electric grid and are susceptible to premature failure due to exposure of electromagnetic pulses associated with nuclear blasts and geomagnetic disturbances (GMD). Such events can induce higher-than-normal currents in transformers, leading to elevated temperatures and voltages compromising the insulation of transformers. Such events can lead to loss of capital investments, and human lives.

Currently used insulation materials in transformers and other electrical components include polymers, cellulose, micro-fiber-based temperature-sensitive binding matrices. As these materials are susceptible to thermal instabilities at high temperatures and are mechanically compliant, more stiff temperature-resistive electrospun silica NF mats could be a successful alternative to the insulation materials in transformers and other potential applications.

Current Challenges

Carbon Nanotube-based Nancomposites

It is established that CNTs possess remarkable electrical, thermal, and mechanical properties with contrast to the traditional composite reinforcement materials such as carbon fiber, glass fiber, nanowires, etc. Also due to the increased surface area and higher aspect ratio of CNTs, the reinforcement effect of CNTs is expected to be enhanced [6]. However, despite their advantages over traditional composites CNT composites are further challenged by additional factors such as fiber dispersion, orientation, waviness and fiber-matrix interfacial properties. Previous studies found these properties to be significantly influenced by the morphology of CNTs embedded in the matrix. In general, long CNTs become wavy and randomly oriented when dispersed in the matrix material. Collectively, they form an interconnected network. Over the past several decades, many theoretical and computational studies have been carried out to capture the mechanics of CNT-reinforced nanocomposites. In most of these models, CNTs are modeled as straight fibers. In addition, a perfect interphase between CNT and epoxy is generally assumed. As such, these models may not capture the realistic morphology of CNT reinforced composites.

Electrospun Silica NF Mat

Due to the nature of electrospinning process, not all fibers are created equal. At continuum level, a three-dimensional stochastic model of the nanofiber mat needs to be studied to understand and model the overall network mechanics. Typically, a variation of morphological parameters such as NF length, diameter, waviness, orientation, distribution, dispersion, etc. can also be observed in a typical electrospun silica NF mat. These parameters are crucial towards the mechanical integrity and performance of the NF mats and need to be incorporated towards stochastic modelling of nanofiber mats. Additionally, the inter-fiber interactions between the different fibers need to be accounted for to model the local mechanical response of the network. Eventually, the failure of these inter-fiber bonds needs to be account for to simulate local failure in the network ultimately leading to the whole network failure.

At nanoscale level, undercoordinated atoms present on the surface of the NF can form an interface when placed at a certain distance and in certain configurations. Such inter-fiber interactions at molecular scale can affect the local failure of the mat and might contribute to a significant load transfer due to the covalent bonding between dangling bonds. The newly formed interfaces can influence the structure-property relationship of the silica NF mat, which could be difficult to obtain from the experimentation.

Moreover, there is an unsettled argument about the brittle-to-ductile transition (BDT) behavior of silica nanofibers as their sizes go down [26][27]. More investigation might be needed to reach at a conclusion.

Furthermore, as the prepared mats might encounter GMD incidents leading to higher-than-normal temperatures, the size-dependent thermal stability of NFs should be studied.

Research Approach

In order to address the highlighted challenges in predictive modelling of CNT composites, we have contributed to developing a method to construct stochastic three-dimensional finite element models of wavy CNT reinforced epoxy nanocomposites. Later, we have worked towards *three-phase model* that accounts for the displacement and stress discontinuities at the CNT-matrix interface. This is known as the *interphase layer* method, in which an interphase region of a given thickness with a given modulus can be incorporated between CNT and polymer matrix phase. The developed algorithm is then used to include CNT agglomerates inside the RVE. Later, a more advanced method called *spring layer* will be discussed, in which the interphase layer is replaced by discrete springs representing the bonding between the CNT and polymer matrix. Such a model can be advanced by infusing an atomically informed displacement-based failure criterion (bond stretching) to study the interface-driven failure properties of the CNT composites.

Molecular dynamics will be used to evaluate the nanoscale properties, such as size-dependent mechanical properties as well as thermal stability, effect of hydroxylation and NF interface on the mechanical properties. Thus obtained elastic properties of individual NFs will then be input into continuum-scale three-dimensional random NF network model. Thereafter, the developed Python algorithm will be enriched by incorporating distance-based cut-off criteria to allow for inter-fiber interactions. A force or displacement-based failure criterion will be assigned to the elastic springs representing inter-fiber interactions.

Thesis Outline

As Molecular dynamics and Finite element method are crucial part of the work performed, it might be significant to provide a step-by-step guideline on these methods. The underlining principles of these methods/ governing physics, their assumptions and limitations, boundary condition implementations, and finally extraction of properties of interest will be discussed in Chapter 2. In the remaining chapters, original research findings obtained during the doctorate will be discussed. Each chapter will be arranged in a self-contained manner in which the relevant literature, simulation procedures, results and concluding remarks will be presented.

In Chapter 3, we will be using ReaxFF force field to study the interfacial properties of CNT/EPON 862-DETDA nanocomposite system. CNT, crosslinked epoxy, and eventually CNT/epoxy nanocomposite material system will be generated. CNT pull-out simulations will be performed to evaluate the interfacial shear stress using LAMMPS code[28]. This chapter is part of the work published at American Society of Composites 32nd Conference [29].

In Chapter 4, first we formulated a two-dimensional network of randomly oriented CNTs using an in-house developed MATLAB script. The generated images will be converted to vector form using a series of laid-out steps, and then will be imported in Abaqus []. The mechanical properties such as Young’s modulus, Poisson’s ratio, and shear modulus of this nanocomposite will be evaluated. Finally, Halpin-Tsai equations will be used to compare and validate the values obtained from the finite element analysis. This study is part of the work published at American Society of Composites 32nd Conference [19]. The developed MATLAB script is published online for free usage [30]. Thereafter, the generation of a complete stochastic three-dimensional aligned/random carbon nanotube/matrix model will be discussed. A realistic three-dimensional stochastic model is developed using in-house built Python script. Morphological parameters such as CNT orientation, dispersion, waviness, and inter-CNT spacing are incorporated, while the effect of increase in waviness angle for the randomly oriented CNT composites will be studied. Finite element models with maximum CNT waviness angles of 0º (straight), 10º, 20º, & 30º will be generated for CNT volume fractions ranging from 0.1% to 1%. The obtained values will be compared with the theoretical models available in the literature. Finally, a three-phase model including CNTs, CNT/epoxy interphase and epoxy matrix will be studied to evaluate the effect of ‘soft’ (E_i =10%–75% E_m) as well as ‘hard’ interphase (E_i =110%–175% E_m) on the composite modulus. The effect of CNT waviness and the presence of imperfect interphase on the matrix to CNT load transfer phenomenon will be discussed. This work is published by Springer Nature in Multiscale Science and Engineering [31].

Chapter 5 discusses the effect of size, hydroxylation, and nanofiber (NF) interface on the mechanical properties of silica. Large-scale reactive molecular dynamics simulations will be utilized to obtain the amorphous structure and finally tensile properties of bulk silica and silica NF at different strain rates. Further, aligned NF configuration with average interspace distance ($d^{\parallel}$=1.5 Å, 3.5 Å, 6.5 Å) and NF junction model will be considered to study the effect of NF interface on the tensile properties of each NF. Thereafter, NF pullout simulations will be used to characterize the NF interface at different arrangements. Later, the size-dependent thermal stability of silica nanowires is studied. The procedure for performing the melting simulations using ReaxFF in molecular dynamics will be laid out. The *optimum* heating rate to melt the NF will be calculated. The effect of NW size on the thermal stability or melting temperature of NW will be discussed. The existence of Melting Point Depression (MPD) due to *surface effect* will be discussed. This research work discussed in this chapter will be to submitted for publications shortly [32][33][34].

Finally, the main findings of this work will be presented in Chapter 6. The future work to advance the developed models will be outlined. The generation of agglomerates in the RVEs will be discussed along with showing the sample agglomerated models. The idea of replacing perfect CNT/matrix interface with the spring layer will be discussed. Also, the extension of developed Python algorithm to model three-dimensional stand-alone NF mat will be laid out.

CHAPTER 2 SIMULATION APPROACH & METHOD

Introduction

The central goal of the current research is to capture the governing physics and underlying mechanics of nanoscale network and their composites.

Here, the basic concepts of Molecular dynamics modelling technique and Finite element approach will be laid out in the current chapter. A brief background is added to get an overview of property calculation from both MD and FEM. The corresponding simulation procedures will be discussed in the specific chapters.

Molecular Dynamics Simulation

In this section, we will only be discussing the ensembles, force-field parameters, property calculation, etc. which will be used in upcoming chapters in order to keep the discussion brief. The details of fundamentals of molecular dynamics calculation can be found elsewhere [35].

Statistical Ensembles

In order to start an MD simulation, there are certain ‘‘controllers’’ that allow to setup for the virtual ‘’test’’ environment. These “controllers” are basically a set of thermodynamic variables which are also known as *ensembles*. Most commonly used ensembles in the MD are NVT (canonical), NPT (Isothermal-Isobaric), NVE (microcanonical). In this, N stands for number of particles, V is the volume of the simulation domain, P is the pressure, T is the temperature, and E represents total energy of the system.

The choice of these ensembles must be carefully made during an MD simulation. NVT can be used when the volume of the system has to be maintained constant while also maintaining or changing its temperature between a certain start and end point using an appropriate thermostat. Typically, Nosé-Hoover [36] thermostat (controls temperature) works well with the constant volume ensemble. Melting of a material inside a constant volume container is an example where NVT will be appropriate choice. In order to simulate atmospheric conditions at room temperature, it would be recommended to use NPT ensemble maintained at atmospheric pressure and 300 K temperature. Generally, Berendsen [37] barostat (controls pressure) and Berendsen thermostat work well with this ensemble. It should be noted that the boundaries where pressure control is applied cannot be treated as a ‘fix’ type boundary.

In LAMMPS, currently two barostat (Nosé-Hoover and Berendsen) methods are available. However, for thermostats, several different methods such as Nosé-Hoover, Berendsen, langevin, etc. are built in. The time constant/ damping parameter or thermostat (*Tdamp*) and barostat (*Pdamp*) should be carefully chosen in order to allow for a smooth relaxation.

ReaxFF Force-field

ReaxFF uses bond distance to determine the bond order between two atoms, i.e. a switching from sp^3 to sp^2 during the simulation based on the bonding environment would now be possible unlike the case with traditional force-fields. When modeling the failure of a material under large strain or modeling the chemical reactions among material constituents, it becomes important for a force-field to autonomously predict changes in bond configuration. All of this was lacking in the traditional fixed-bond potentials. As ReaxFF assigns the bond orders for all the relevant pair of atoms based on their interatomic distances, the interatomic forces are determined based on the assigned bond order. Based on the changes in interatomic distances, bond orders are updated throughout a simulation which allows for formation and breaking of bonds within the simulation. All the parameters used by ReaxFF are optimized *a priori* to reproduce results from quantum mechanics computations for selected small molecular systems. The non-bonded energy contribution in ReaxFF comes from van der Waals and electrostatic/columbic interactions interactions. As the break formation and breaking may take place in a particular simulation, the non-bonded interactions have to be calculated among all the bonded as well as non-bonded atoms. This enables ReaxFF to be applied for both predominantly covalent and ionic materials without user input. Other energy terms in ReaxFF functional form represent bond, over-coordination, under-coordination, valence angle, double-bond valence angle penalty, torsion conjugation energies.

By default, the cut-off distances for non-bonded interactions are set to be 10 Å, while for the covalent range is typically taken to be 5 Å-which is sufficient for most elements to capture even the weakest of covalent interaction. But the values can be changed. A charge equilibration scheme is employed at each iteration to calculate the partial atomic charges, which are then used to calculate Coulombic interactions.

ReaxFF force-field was initially developed by van Duin et al [38] for hydrocarbon system in 2001. But now, there has been significant number of materials that can be modeled by ReaxFF parameters optimized for those materials [39].

Property Calculation

In molecular dynamics, in order to do the property calculation the system must become an ergodic system whose accumulated trajectories eventually cover all the possible states in the entire phase space. In order to achieve such fully evolved system, we normally allow the system to relax many times longer than the actual relaxation time for any specific property to settle. Such a system can be assumed to have closely satisfied ergodic principle. Thereafter, any observable property can be calculated by taking the temporal average of the trajectories under equilibrium.

Stress Calculation

It is important to note that the definition of stress tensor is different for continuum mechanics and at atomistic scale. In continuum scale, a stress vector is defined at a mathematical point but at atomic scale, a representative volume must be selected. Inside this chosen representative volume, all the atoms *j* lying at distance r_{ij} around a specific atom exert forces f_i on atom 1 and hence contributes to the stresses experienced by the atom *i*. It represents the part of the virial stress that comes from the potential part. In addition to this part, the momentum flux of the atoms within the material or the thermal vibrations of the atom also adds up to the stresses in the material. Therefore, it can be said that at atomic scale, the stress tensor comprises of a kinetic part (first term in equation (2.1) as well as a potential part (virial stress). It can further be noticed that for a solid material, the contribution from the kinetic part of the stresses is very small compared to the part of stresses that comes from the intra and inter-atomic interactions between the atoms. Equation (2.1) shows the stress tensor for an atom or stress/atom, where *i* and *j* takes the values *x, y, z* to generate nine components of the stress tensor. Equation (2.2) elaborates on the virial stress per atom component. To obtain the stresses for entire system, the per atoms stresses can be summed up for all the atoms and then divided by the system volume. It should be noted that the stresses obtained will be the average stresses for the volume of the system.

$$\sigma_{ij} = -mv_i v_j - W_{ij} \tag{2.1}$$

$$
\begin{aligned}
W_{\mathrm{ij}} = {} & \frac{1}{2}\sum_{n=1}^{N_p}\left(r_{1_i}F_{1_j} + r_{2_i}F_{2_j}\right) + \frac{1}{2}\sum_{n=1}^{N_b}\left(r_{1_i}F_{1_j} + r_{2_i}F_{2_j}\right) \\
& + \frac{1}{3}\sum_{n=1}^{N_a}\left(r_{1_i}F_{1_j} + r_{2_i}F_{2_j} + r_{3_i}F_{3_j}\right) \\
& + \frac{1}{4}\sum_{n=1}^{N_d}\left(r_{1_i}F_{1_j} + r_{2_i}F_{2_j} + r_{3_i}F_{3_j} + r_{4_i}F_{4_j}\right) \\
& + \frac{1}{4}\sum_{n=1}^{N_i}\left(r_{1_i}F_{1_j} + r_{2_i}F_{2_j} + r_{3_i}F_{3_j} + r_{4_i}F_{4_j}\right) \\
& + Kspace\left(r_{1_i}, F_{1_j}\right) + \sum_{n=1}^{N_f} r_{1_i}F_{1_j}
\end{aligned}
\tag{2.2}
$$

In equation (2.2, the notations N_p, N_b, N_a, N_d, and N_i correspond to pairwise, bonded, angle, dihedral, and improper interactions that atom 1 is part of. *Kspace* term corresponds to coulombic interactions, while N_f takes into accounts of the applied *fixes* to the atom 1.

It might be interesting to think if the stress tensor defined for atomic scale is equivalent to Cauchy's mechanical stress tensor at continuum scale. Costanzo et al. [40][41], Zhou [42] and Shen and Atluri [43] concluded that the atomic stress and Cauchy stress only coincide at absolute zero temperature as the velocity term in stresses vanish under these conditions.

Strain Calculation

In Molecular dynamics, a material can be strained by applying incremental constant or variable displacement to a set of fixed atoms along the desired direction. In this work, all the strain fields refer to *engineering strains* unless specified. It should be noted that the strain is not applied instantaneously to the system, and that a specified number of steps is allowed for material relaxation in between each displacement increment. In this study, the strain is applied until the material fractures.

Finite Element Method

In this section, like before, we will only be focusing on the elements, elastic property calculation, etc. that will be utilized in the next chapters. The details on fundamentals of finite element technique can be found elsewhere [44].

Elements Selection

In Abaqus, C3D20 brick elements will be used to model Carbon nanotubes. Each element has 20 nodes and there are three translational degrees of freedom associated with each node. Parts with complex geometry (e.g., interphases and degenerated matrix in this study) are convenient to generate using C3D10 tetrahedral elements. C3D10 element has 10 nodes with three translational degrees of freedom per node.

For three-dimensional silica NF network, 3D beam elements are chosen. Solid circular profile of chosen diameter is assigned to each element in a fiber.

Elastic Properties Calculation

Elastic Modulus

To evaluate the elastic Modulus, a displacement resulting in 1% strain is applied on the face perpendicular to the direction of calculation of elastic moduli, while keeping the opposite face fixed. Necessary accommodations are made to allow for the poison’s ratio effect in the loading in transverse directions. The average normal stress ($\bar{\sigma}$) can be calculated using either of the following expressions:

$$\bar{\sigma} = \frac{1}{V}\int_V \sigma dV \qquad (2.3)$$

$$\bar{\sigma} = \frac{\sum_i^N F_i^R}{A} \tag{2.4}$$

where F_i^R is the reaction force in the direction of applied displacement, N is number of nodes on the surface where displacement is applied, A corresponds to the cross-sectional area and V is element volume. In FEM, stresses are evaluated from derivatives of **u** and hence are less accurate and take longer to converge. Therefore, equation (2.4 can be preferred to evaluate average stresses. The effective modulus ($E_{eff,ii}$) of the composite can then be obtained from the ratio of average normal stress to the applied strain (ΔL/L).

Poisson's Ratio

Effective Poisson's ratio is given as the ratio of lateral strain to normal stress, and is calculated from a uniaxial tensile test using equation(2.5):

$$\nu_{eff,ij} = -\frac{\varepsilon_{jj}}{\varepsilon_{ii}} \quad (i \neq j) \tag{2.5}$$

Shear Modulus

In order to calculate the effective shear modulus, the degrees of freedom for one edge of the RVE can be completely fixed, while the opposite end is subjected to shear deformation resulting in 1% shear strain. The volume averaged shear stress and shear strain can be substituted in equation (2.6) to calculate shear modulus.

$$G_{eff,ij} = \frac{\int_V \tau_{ij} dV}{\int_V \gamma_{ij} dV} \quad (i \neq j) \tag{2.6}$$

CHAPTER 3 INTERFACE PROPERTIES OF CNT/EPOXY NANOCOMPOSITES: A MOLECULAR DYNAMICS STUDY

Introduction

In pursuit of our research goal to develop a predictive computational model to evaluate mechanical properties of CNT/polymer composites, we first seek to obtain the elastic properties of the nanocomposites. Properties at the interface between CNT/polymer are critical to determine mechanical properties of these nanocomposites [6].

While CNTs provide some reinforcement of the polymer matrix in the form of enhanced moduli relative to polymer matrix alone, a detailed understanding of the CNT/polymer interfacial region remains fundamental to the optimization of the mechanical behavior of these composites. The interface plays a significant role in the load transfer from matrix to fiber. A *better* interface results in consequent improvements in the nanocomposite stiffness and strength. Characterization of the CNT/polymer interfacial interactions during pull-out will be the focus of this study.

In the present study, we have used reactive force field (ReaxFF) to study the interfacial properties of CNT/EPON 862-DETDA nanocomposite system. Because molecular-level failure events can play a significant role in epoxy mechanical behavior, the ReaxFF can be used as an ideal tool for MD simulations involving crosslinked epoxies. Pull out simulations are performed to characterize the CNT/polymer interfacial interactions. Pull out energy is used to calculate the interfacial shear strength of CNT/polymer nanocomposite.

Having a good understanding of the interaction between the CNT's and polymer matrix is key to being able to apply the benefits of SWCNT to composite materials. Molecular

Dynamics (MD) research by Komuves et al. showed that the addition of 0.1% SWCNT weight fraction resulted in the Young’s modulus of the SWCNT-EPON 862 composite roughly 20% higher compared to the pure EPON 862 matrix [45]. Similar MD results were achieved by Zhu et al [46], who showed that the addition of (10,10) SWCNT to pure a EPON 862 matrix resulted in a composite that was 10 times stiffer and increased the Young’s modulus by 20% over the pure EPON 862 matrix. The EPON 862 matrix is the polymer that holds the fibers in composites together and is often simply referred to as resin.

Liao et al. used pull-out simulations to find Interfacial characteristics of a carbon nanotube–polystyrene composite system [47]. Gou et al. found the interfacial bonding of single-walled nanotube (SWNT) reinforced epoxy composites was investigated using a combination of computational and experimental methods [16]. Frankland et al. performed MD study on CNT/Polyethylene system to evaluate the interfacial properties of nanocomposites using Lennard-Jones Potential [14]. Chowdhury et al. [48] employed hybrid potential to simulate CNT pullout from PE matrix. Li et al. used COMPASS (Condensed-Phase Optimized Molecular Potential for Atomistic Simulation Studies) to pull CNT out of PE matrix, while taking into account only the van der Waals interactions between CNT/PE [49]. Ingvason et al. [50] used COMPASS force-field parameters to study interfacial interactions at CNT/Epoxy interface.

Whereas traditional force fields are unable to model chemical reactions because of the requirement of breaking and forming bonds (a force field's functional form depends on having all bonds defined explicitly), Reax Force Field (ReaxFF) eschews explicit bonds in favor of bond orders, which allows for continuous bond formation/breaking. In the ReaxFF, the potential energy is defined as a function of bond order with energy penalties for nonequilibrium configurations. The ReaxFF was initially developed to model bond dissociation and formation in carbon-based materials [38]. Odegard et al [51] proved ReaxFF to be working for bulk epoxy system using parameters obtained by Liu et al [52].

Molecular Structure of a Nanotube/Epoxy System

Carbon Nanotube (CNT)

A CNT is made from pure Carbon atoms. This is constructed out of a sheet of aromatic Carbon rings that has been rolled up into a tube. The SWCNT that we chose for the pull-out test, it is a (8,8) armchair SWCNT. DL-POLY [53] is used to make CNT of diameter 10.85 Å and length 62.87 Å, shown in **Fig. 3.1**. It is further equilibrated using ReaxFF force-field parameters.

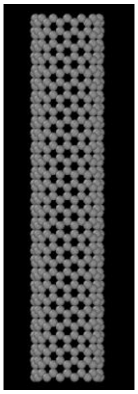

Fig. 3.1 *A (8,8) Armchair SWCNT [16]*

Epoxy

Based on its molecular structure, epoxy is generally categorized under *network polymers* due to its highly cross-linked three-dimensional network structure. With regard to the material behavior at raising temperature, epoxies fall under *thermosetting polymer.* Epoxies possess covalent bonding between their adjacent molecular chains (cross-links). During the heat treatments, the cross-link bonds anchor the chains together to resist the vibrational and rotational motions at high temperatures. Therefore, the material does not soften upon heating unlike *thermoplastic polymers.* The excessive heating of thermosets causes the breaking of cross-link bonds leading to polymer degradation. Thermosets generally have higher melting point due to network formation and are harder and are stronger than thermoplastics, rendering their use as aerospace materials. Their higher melting point (T_m) compared to that of linear polymers is due to the presence of aromatic rings in the polymer chain. Also, due to covalent bonding between the chains, the lack of rotational freedom and flexibility tend to restrict molecular rotation and leads to high value of T_m.

Epoxies have excellent combination of mechanical properties and corrosion resistance. Due the 3-D network structure, they are dimensionally stable. They act as good adhesives and have good electrical properties in addition to being relatively inexpensive. They are commonly used for electrical moldings, sinks, adhesives, protective coatings and as an embedding material for the fiber composites.

The modeled epoxy system was composed of 8 EPON 862 (Diglycidyl ether of Bisphenol F) crosslinked with 4 DETDA (Diethylene Toluene Diamine) molecules provided by Kelkar et al.[5]. **Fig. 3.2** shows the molecular structure of EPON 862 monomer & DETDA before crosslinking. During the crosslink process, each amine group in DETDA can react with two epoxide groups in EPON 862. Therefore, a molar ratio of 2:1 of EPON 862 to DETDA molecules is necessary for a stoichiometric mixture.

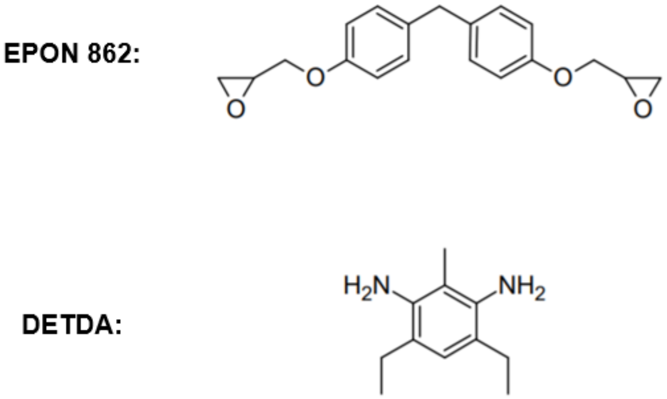

***Fig. 3.2** Molecular Structures of EPON 862 and DETDA monomers*

The crosslink density can be defined as the number of reactions performed (between epoxide and amine as shown in **Fig. 3.3** during crosslinking divided by the maximum number of theoretical reactions possible to happen. For 8 such EPON and 4 DETDA molecules were crosslinked in similar manner. However, the crosslink density achieved is approximately 75%. **Fig. 3.4**(a) shows typical molecular structure of these equilibrated and crosslinked EPON-DETDA molecules. 8 EPON-862 & 4 DETDA molecules are put in a larger box and is equilibrated using ReaxFF with the parameterizations of Liu et al.[15]. The initial density of the system was 0.3 g/cc. The model was further allowed to shrink under NPT ensemble for nearly 150 ps, using 0.1 fs of timestep. After this step, the final density of epoxy system was 1.15 g/cc, which is fairly close to the target density, 1.2 g/cc. To release the residual stresses in the system, equilibration and minimization is performed in NVT ensemble for 10 ps at the same timestep. Residual stress after this step is ~ 0.37 GPa, which can be overlooked safely. **Fig. 3.4**(b) represents the epoxy system at final density of 1.15 g/cc.

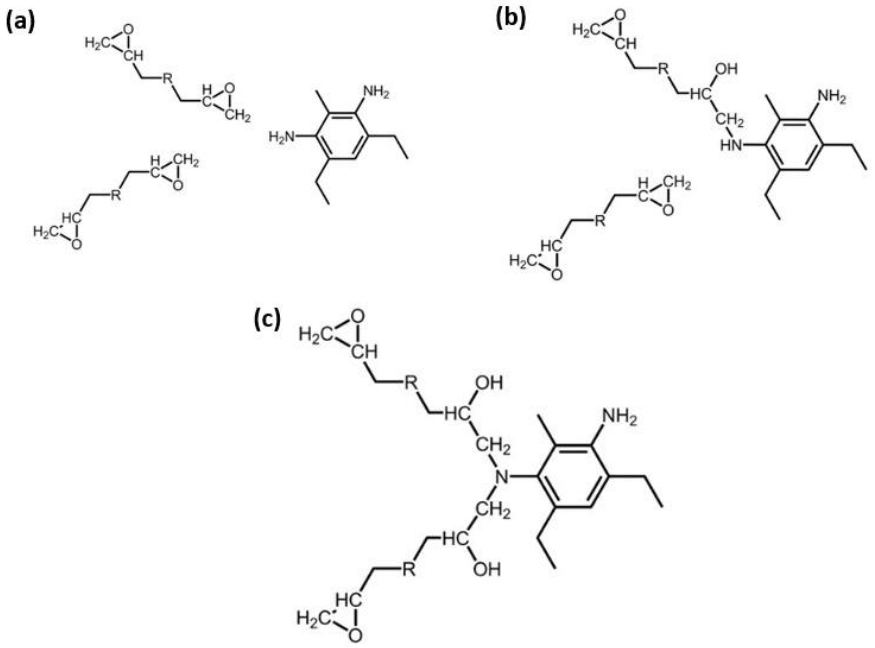

Fig. 3.3 *Crosslink reaction between epoxide from EPON and amine from DETDA molecules*

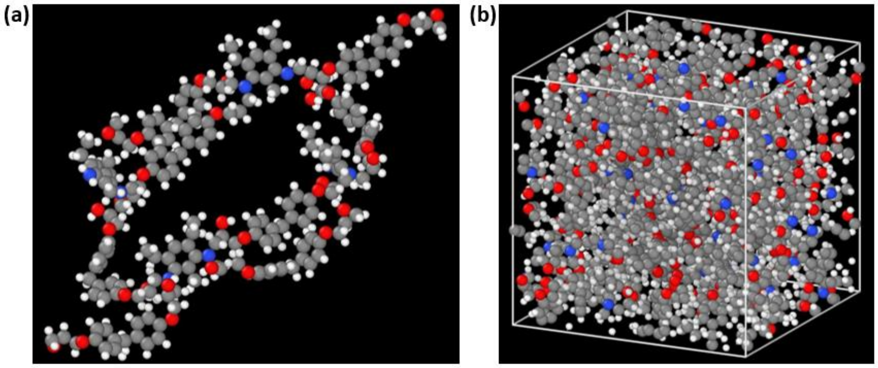

Fig. 3.4 *Molecular structure of (a) 8-EPON 4-DETDA Crosslinked molecules, (b) equilibrated and densified MD model with ReaxFF. Coloring scheme: APK [17]*

CNT/EPON 862-DETDA System

Several researchers have observed and reported the role of matrix stiffness on the reinforcing effect of CNTs [54][55][56]**.** Loos et al [55] observed that lower crosslinking degree in epoxy polymers result in shorter epoxy chains and may be able to better interact with CNTs by embedding and coating the SWCNTs with a polymer sheet that leads to a more stable CNT-epoxy interface. Ci et al. [57] showed that CNT reinforcement effect decreases when reinforcing unfunctionalized CNTs in the matrices stiffer than 2 GPa.

The nano-scale material system in this study is composed of carbon nanotube (CNT) and EPON 862-DETDA matrix. Specifically, a (8,8) CNT is embedded in polymer matrix. Previously equilibrated and small epoxy molecules system are put around a cylindrical wall representing CNT as shown in **Fig. 3.5**. The wall is set to interact with the surrounding epoxy particles using *lj 93* formulation defined by the following equation:

$$\mathrm{E} = \varepsilon\left[\frac{2}{15}\left(\frac{\sigma}{\mathrm{r}}\right)^{9} - \left(\frac{\sigma}{\mathrm{r}}\right)^{3}\right] \quad \mathrm{r} < \mathrm{r_c} \qquad (3.1)$$

The parameters ε = 0.5 kcal/mole, σ = 0.2 Å, and $r_c = 2.5$ Å that were chosen arbitrarily. The *wall/lj93* interaction is derived by integrating over a 3d half-lattice of Lennard-Jones 12/6 particles. Thus, it is a weak interaction when compared to L-J 12-6 formulation.

This model is slowly compressed to the desired density using *fix deform* command in LAMMPS using NVT time integration at 300 K temperature. Once the final density is achieved, the wall is replaced with a (8,8) CNT and the whole system is equilibrated in NPT ensemble at 300 K for 50 ps in order to release the build-up stresses in the system.

The final model contains 12,460 atoms including 700-C-atom CNT, 192 EPON 862 & 96 DETDA molecules. The dimensions of the system are ~5 x 5 x 5.3 nm. Average density of the system is ~ 1.06 g/cc.

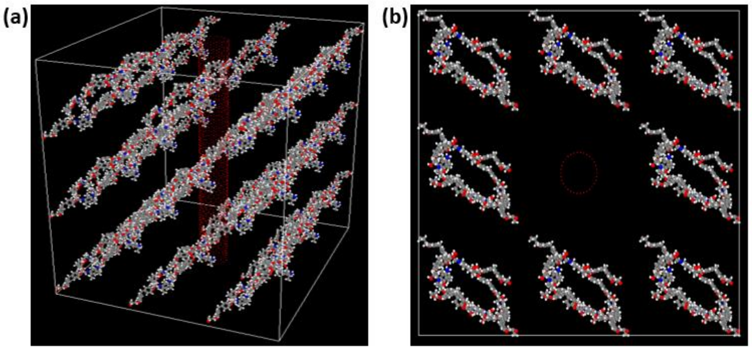

Fig. 3.5 *Molecular model of CNT/epoxy in Preparation (a)Perspective view, (b)Top view. Coloring scheme: CPK* [58]

In the molecular dynamics, the entire material system is represented with the ReaxFF potential. The system is replicated across periodic boundaries in each of the 3-dimensions, thereby making CNT & polymer chains infinitely long. This model is further equilibrated for 30 ps at a timestep of 0.1 fs. After equilibration, a minimization is performed to find configuration that will hopefully be in local potential energy minimum, and the new atom positions to be computed. **Fig. 3.6** shows the final CNT/epoxy model, which is ready for pull-out simulations.

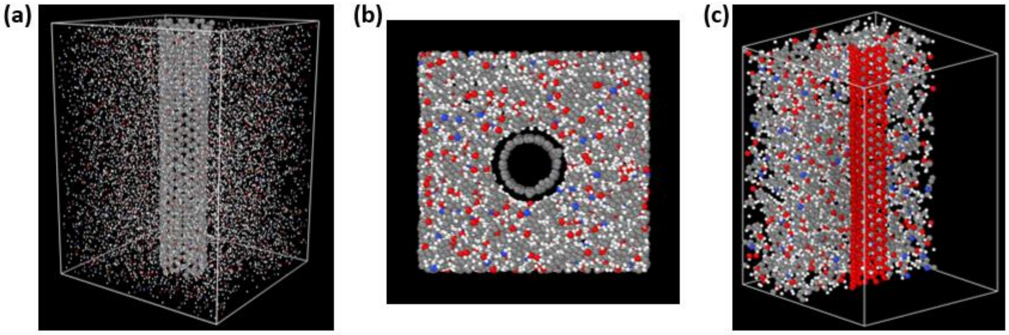

Fig. 3.6 *Final Molecular model of CNT inside epoxy matrix (a) Perspective view, (b) Top view, (c) Section view. Coloring scheme: CPK* [58]

Mass densities were computed using the “fix/ave” spatial command in LAMMPS [18], which sums the per-atom densities and averages them for slices of a specified thickness along a specified axis. A slice thickness of 0.4 Å stacking along the y-axis was chosen to observe the density change moving away from CNT surface oriented in the x-z plane. **Fig. 3.7** shows the average mass density profile for the polymer molecules along the radial distance from CNT center. It is plotted using *chunk/atom* command in LAMMPS, that allows to construct a density distribution plot by measuring the local densities of epoxy at various radial distances starting from the center to half-length of the periodic box. Interface region depicted from **Fig. 3.7** is extended up to nearly 10 Å from CNT surface. It can be noted that in this region, the density of epoxy is 105% higher than that of neat polymer system. Outside of this region (away from the CNT), the density profile oscillates about 1.15 g/cc, which was calculated as the average density for neat polymer system.

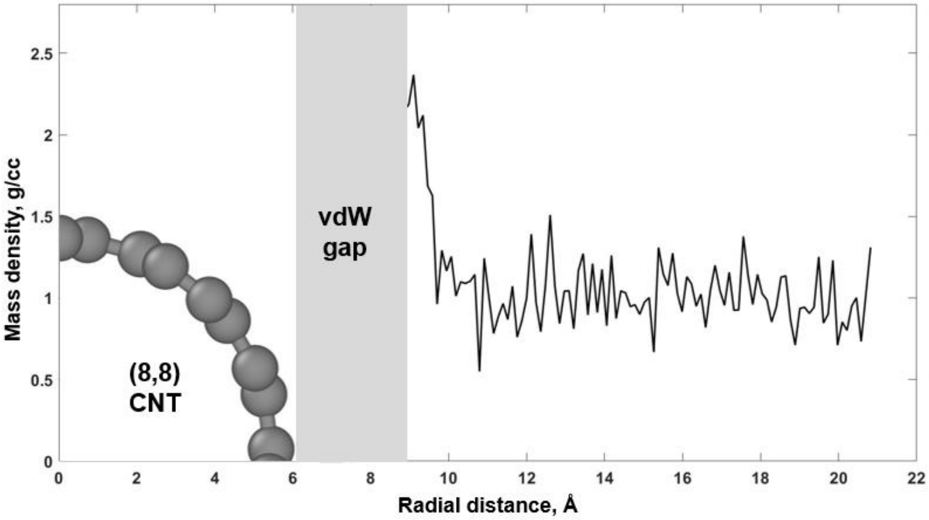

Fig. 3.7 *Radial density profile of CNT/epoxy Composite*

Pullout Simulations

The simulation cell with periodic boundary condition in x-y plane as shown in **Fig. 3.8** is composed of a fragment of open-ended CNT totally embedded inside EPON-DETDA matrix. To capture the complete pull-out of CNT from epoxy matrix, periodic condition has been removed in the axial direction of CNT (i.e. z direction). This eliminates the interactions between upper and lower end of CNT. Size of simulation cell in axial direction of CNT is chosen to be slightly larger than the CNT length. This prevents CNT from going out of the simulation cell after it has been completely pulled out of epoxy matrix. Box dimensions are 5 x 5 x 11 nm.

The pull-out simulations of CNT from epoxy matrix are carried out by applying a constant velocity of 0.01 Å/fs to approximately 5 Å layer of carbon atoms at the lower end of CNT. Nearly 5 Å upper and lower part of epoxy matrix is held fixed during the pullout. The simulation is run for ~ 60,000 MD time steps of 0.1 fs.

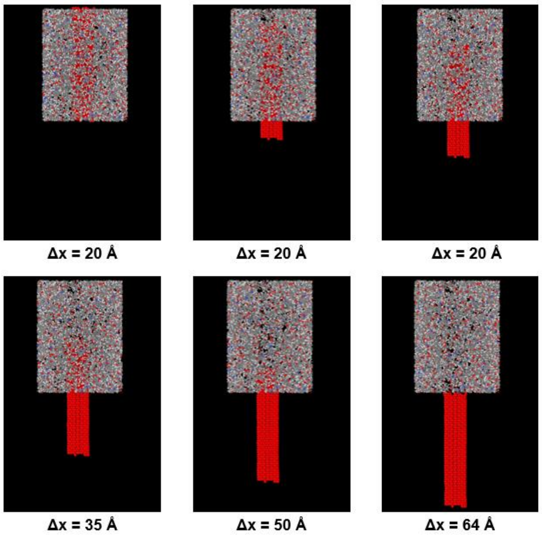

Fig. 3.8 *Snapshots from the MD Simulation of SWCNT during pullout (Epoxy matrix is made slightly transparent for better CNT visualization)*

Results & Discussions

In order to evaluate the interfacial bond strength, typically methods such as matrix Poisson effect, fiber pullout, fiber push-through, short-beam-horizontal shear, transverse tensile, dynamic modulus, broadband dielectric spectroscopy[59], and photoelasticity. More elaborative discussion is presented in the reviews by [60][61]. As fiber pullout test is perhaps the most easy and common test to evaluate interfacial strength, we have used it in this work. It is most convenient method to evaluate average bond strength. The common limitation of this method arises from the fact that for the fiber to be pulled out from the matrix, the 'expected' interfacial shear strength (ISS) of the interface should be less than the ultimate tensile strength of the fiber. It can be noted that if the above condition is not satisfied, the fiber will break rather than being pulled out! Fiber pullout test experimentation is challenged by the cost involved, difficulties in the sample preparation of single fiber coupons, non-uniform shear stress distribution along the interface and large data scatter. However, molecular dynamics can be used as an efficient tool to perform these simulations.

In the nanotube composites, the bonding strength between the nanotube and epoxy resin can be evaluated by interfacial bonding energy. In this work, the nature of interfacial bonding energy comes from the electrostatic and van der Waals forces (unbonded), and other bond-dependent terms included in the reactive force-field formulation.

The initial total potential energy of the pullout simulation is -1456703.7 kcal/mol. The potential energy of the SWNT/epoxy resin composite system increased (became less negative) as the nanotube was pulled out of the epoxy resin, as shown in **Fig. 3.9**. In the pullout simulation, the entire nanotube and epoxy resin were not held fixed. The potential energy of the nanotube and epoxy resin increased due to the changes of their configurations during the pullout. The deformation of the nanotube and epoxy resin during the pullout has influence on the pullout energy [16]. After the pullout, the potential energy increased to -1456213 kcal/mol.

Gou et al [16] and Liao et al [62] defined the pullout energy as:

$$E_{Pullout} = E_{Final} - E_{Initial} \tag{3.2}$$

In the same references, the energy difference between the fully embedded NT and the completely pulled out NT configuration is equated to the work required (W) for fiber pullout (Equation (3.2).

$$E_{Pullout} = W = \int_{x=0}^{x=L} 2\pi r(L-x)\,\tau_i dx \tag{3.3}$$

Based on it, a relation between pullout energy and interfacial shear strength can be defined as:

$$\tau_i = \frac{E_{Pullout}}{\pi r L^2} \tag{3.4}$$

Where, L = Embedded length of the SWCNT and r = radius of the SWCNT. It should be noticed that τ_i is the average shear stress value across the CNT/epoxy interface.

Using (3.2, the pullout energy is calculated to be 490.7 kcal/mol (0.00341 fJ). From Equation (3.2 & (3.4, the interfacial shear strength between the nanotube and resin was calculated to be about 50.61 MPa.

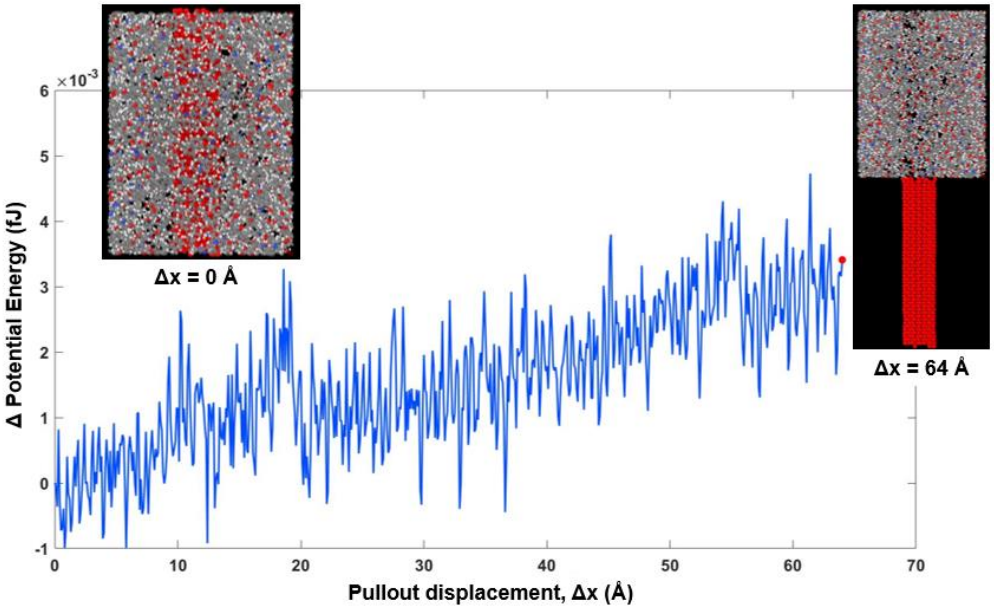

Fig. 3.9 *Variation of change in potential energy during the pull-out of (8,8) CNT (Epoxy matrix is made slightly transparent)*

Conclusion

This computational study of interfacial bonding of SWNT reinforced epoxy composites indicates that there could be an effective stress transfer from the epoxy resin to the nanotube. The interfacial bonding was predicted using molecular dynamics simulations based on a cured epoxy resin model, which was constructed by incorporating the three-dimensional cross-links formed with curing agent molecules. Reactive force-field (ReaxFF) is used to consider the bond formation and dissociation during CNT pullout from crosslinked epoxy matrix. The pullout simulations of a SWNT from the epoxy resin showed that the interfacial shear stress was calculated to be 50.61 MPa.

It can be noted that the change in cross-link density, density of epoxy system, CNT diameter, CNT length, pullout rate, number of walls in MWCNT, etc. can lead to different values of interfacial shear stress. Elaborative studies about the effect of these parameters can be found in other literatures [14][48][49].

CHAPTER 4 MECHANICS OF CNT NETWORK AND ITS COMPOSITES

Introduction

Carbon nanotubes (CNTs) are the filler materials of nanoscale dimensions which when added to the polymer matrix form a strong yet light-weight multifunctional composite material. They possess remarkable electrical, thermal, and mechanical properties with contrast to the traditional composite reinforcement materials such as carbon fiber, glass fiber, nanowires, etc. Due to the increased surface area and higher aspect ratio of CNTs, the reinforcement effect of CNTs is expected to be enhanced [6]. Owing to their excellent properties, CNT composites can find great applications in electronics [11], drug delivery [12], electromagnetic shielding [13], strong-yet-lightweight aerospace materials [10], etc. Thus, it becomes critical to evaluate their multifunctional properties before bringing them to the application. However, despite their advantages over traditional composites CNT composites are further challenged by additional factors such as fiber dispersion, orientation, waviness and fiber-matrix interfacial properties. The theoretical, experimental and multiscale modelling aspects of CNT based polymer composites are reviewed extensively by [63]–[68]. Depending upon the CNT orientation, there can be random [17], [69]–[72] as well as aligned [73]–[76] CNT composites. Previous studies found that the properties of these composites are greatly influenced by the morphological parameters such as CNT orientation, dispersion, waviness, diameter, inter-CNT spacing, etc. [17], [69]–[71][75][20][19]. Notably, such morphological parameters also play role in piezoresistive [77] and electrical properties [78] of similar network-based composites.

Over the past few years, efforts have been made to obtain the morphological parameters for aligned and random CNT composites from their micrograph images. In their pioneer work, Fisher et al. [1] observed the significant curvature of CNTs in TEM images obtained by Qian et al. [72] and studied their effect on elastic properties of the composite. This study revealed that the degradation of elastic properties by a factor of two or more. Motivated by these results, Natarajan et al. [2] developed an energy-filtered technique to describe all the morphological parameters for aligned CNT composites as a function of CNT volume fraction. A more detailed discussion about three-dimensional visualization of carbon nanotube networks can be found in the review by Liu [79]. To mimic the CNT morphology theoretically, Stein et al. [3] used a theoretical framework to put CNT waviness in relation to inter-CNT spacing and volume fraction for aligned CNT composites. Both studies emphasize on quantifying morphology measures as the volume fraction of CNTs in polymer matrix evolves, whereas no discussion about their effect on elastic properties is provided. This gap is later filled by Stein et al. [4] by incorporating the obtained distributions to the three-dimensional computational model, which highlighted their impact on the elastic properties of Aligned CNT composites.

Similar studies are also performed for Random CNT composites. For instance, Islam et al. [5] generated a three-dimensional finite element model capable of generating CNTs up to volume fraction as high as 50 % at varying aspect ratios and is aiming to further use this model to calculate the elastic properties of random CNT composites. Nevertheless, the model could only generate straight fibers, which is barely observed in the case of CNTs. The CNT waviness is further included by Herasati et al. [70] along with CNT orientation by developing their own MATLAB algorithm to generate the three-dimensional finite element model, which is further exploited to calculate elastic properties of the composites. Considering several cases by varying the parameters, they concluded the CNT alignment to be a more influencing parameter than the CNT waviness while predicting elastic properties of random CNT composites. It is further supported by results obtained by Bhuyian et al. [80][18] who also incorporated less-studied parameters such as a soft CNT/polymer interphase and CNT agglomeration. Fiber/matrix interface has been discussed to be of importance by Reifsnider et al. [6]. A significant number of atomistic studies using molecular dynamics simulations have primarily focused on evaluating the interfacial shear stress for CNT-polymer composites [63][14]–[16], [48], [81]. Comparatively fewer studies utilized multiscale models to evaluate the effect of CNT-matrix interface on the mechanical properties of the composites [68][81][82]. However due to the limitation on the model size, the morphological parameters of the CNTs could not be captured holistically. Gou et al [83] and many other [64][84][85] studies discussed theoretical approach to study the interfacial shear stress in CNT-polymer composites. Several finite element studies have also focused on evaluating the effect of fiber/matrix interphase modulus ('soft' and 'hard' interphase), interphase thickness and its profile for the idealized CNT morphology [86]–[89]. Several researchers confirmed that the increase in the density of the polymer matrix in the vicinity of the fiber reinforcement [90]–[93] as well as the increased covalent bonding at the interface due to the surface functionalization of the fibers [91][93] can lead to the formation of a 'hard' interphase. Later in their studies, Bhuyian et al [80] [18][94] [95] used AFM and SEM to confirm the presence of voids, and hence represented CNT/matrix interphase as a 'soft' interphase.

On the analytical side, micromechanics-based models such as Mori-Tanaka model [96], have been previously developed and modified later to explain the load transfer mechanisms between fiber and matrix [97] for cylindrical fiber phases embedded in the matrix. Although these models work well for misaligned short fibers with small aspect ratios [85], they were developed for the straight inclusions. Later, some attempts have been made to incorporate the CNT waviness [17][98], such as the analytical-numerical model proposed by Bradshaw et al [99][17]. However, their model treated the short CNT fibers as continuous fibers to avoid fiber end effects [100]. Moreover, the CNT waviness was defined by an in-plane sinusoidal wavy shape, which, in reality can have more complex and irregular wavy contour. Despite these efforts, finding strain-displacement relations for the Mori-Tanaka model is a tedious task [96][17].

It is evident from the literature that morphological parameters have significant influence on the elastic properties of CNT/polymer composites[17]. Yet, the underlying mechanisms through which these parameters contribute to the overall elastic behavior of the nanocomposites are not clearly understood.

In this chapter, first we have developed a simplified MATLAB script to allow for generating 2D images for randomly oriented short and wavy short fiber composites. Such 2D fiber network can be a representative of a case of more “in-planar” distributed fibers in a matrix. The elastic modulus obtained from the computational model will be compared to 2D in-plane random fiber micromechanical model available in the literature. A methodology will be laid out to allow generating fiber/matrix interphases using the developed MATLAB script.

Later to construct three-dimensional RVEs, we have followed a unique approach for the prediction of Elastic Moduli of CNT based composites. Randomly oriented CNTs composites are constructed with CNT volume fraction of 0.1% to 1% and are studied at the maximum ‘allowable’ waviness angles (θ_{max}) of 0º (straight), 10º, 20º and 30º. The elastic modulus obtained from the three different computational models are compared to quantify the effect of fiber waviness on the elastic behavior of the composites. Later, a three-phase model is used to study the effect of ‘hard’ as well as ‘soft’ CNT/epoxy interphase on the elastic modulus of wavy CNT nanocomposite.

Random Fiber Composite Modelling

2D Model Generation

Based on Statistical Geometry of Fibrous Network [101], a MATLAB script is developed to generate two-dimensional network of randomly distributed fibers. **Fig. 4.1** shows a flowchart describing code algorithm [30]. The first part of the code allows us to generate random fiber model (**Fig. 4.2**). To obtain this model, random number generator is used to locate fiber centers (x_i,y_i) on a 2D plane of pre-determined dimension. Knowing the length of fibers (*L*) and considering fiber orientation (θ_i) to be random, following geometric formulation can be included to obtain the fiber co-ordinates (X_i, Y_i):

$$\boldsymbol{X_i = x_i \pm \left(\frac{L}{2}\right) \cos\theta} \tag{4.1}$$

$$Y_i = y_i \pm \left(\frac{L}{2}\right) \sin\theta \tag{4.2}$$

Fig. 4.2 presents code inputs and generated random fiber network. **Fig. 4.2**(b) displays the local fiber density in the selected grid regions. In other words, each color represents average fraction of CNT in a particular region/grid. The maroon region in the plot shows highest v_f of fiber in that region/grid. It could be used as an indication of agglomeration in that particular region. It could be noticed that a more uniform color plot would be representative of better fiber distribution. In other words, such a color plot can be used as a qualitative analysis of the fiber dispersion and distribution in an RVE.

This random fiber network can be closely approximated as more 2D (in-plane) carbon nanotubes (CNTs) randomly dispersed on a polymer sheet.

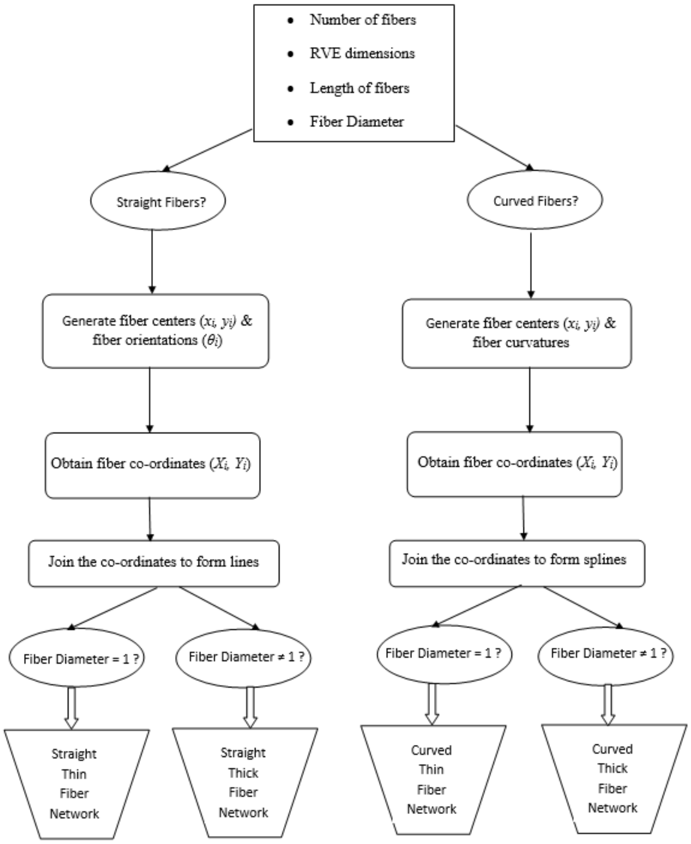

Fig. 4.1 *Flowchart Describing Algorithm to Generate Straight Random Fiber Network*

[101]

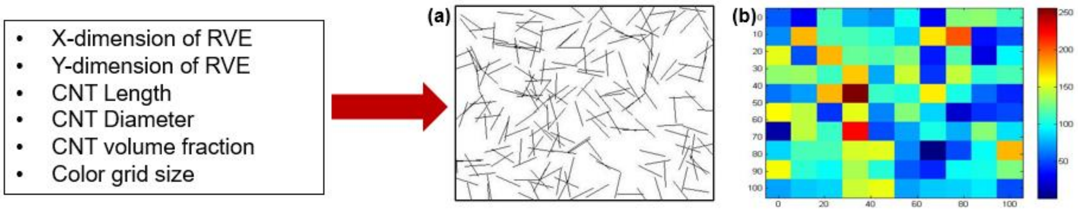

Fig. 4.2 (a)*Straight Random Fiber Network, (b)Color Map showing local fiber density for given network*

Three-Dimensional Stochastic Modelling of Wavy CNTs

A wavy CNT is treated as a robotic arm with n_p+1 number of hinges/connectors joining n ($=l_{cnt}/n_p$) number of segments with length l_{seg}. In order to generate the first segment of each CNT, random values for CNT orientation angles (α_i, β_i) are chosen. Each subsequent segment can be generated with respect to the reference plane of previously generated segment. Hence, in order to assign a certain waviness characteristic to a CNT, relative waviness angle can be assigned to each subsequent segment as shown in **Fig. 4.3**. For a defined volume fraction and RVE size, the number of CNTs (of a known geometry) can be calculated. In order to avoid the CNT-CNT penetration, Brute force algorithm is used. It ensures that the distance of currently generated coordinate from all the previously generated points is greater than a distance d_{min} ($=d_{CNT}$ when all CNTs have same diameter). Several other more efficient algorithms exist in literature to avoid the filler-filler contact, the detail of which can be found elsewhere [78][102]. It can be noted that the parameter d_{min} can also be used to uniformly disperse the CNTs within the RVE. For instance, using a smaller value of d_{min} in a certain region of the RVE can generate the poorly dispersed (agglomerated) CNT fibers in that region. **Fig. 4.4** lays out the algorithm followed to generate the wavy CNT model, while **Table 4.1** lists the description of the parameters used in the algorithm flowchart. **Table 4.2** lists the morphological parameters that are used to generate the RVEs shown in **Fig. 4.8**.

Fig. 4.5a shows the meshed model generated for $v_f=1\%$ with $\theta_{max} = 20^{\circ}$. It can be observed that during the model generation, several values picked from the random distribution are neglected based on the RVE constraints and brute force check. However, the distribution of the chosen waviness angles is preserved to be random uniform as shown in **Fig. 4.5**b.

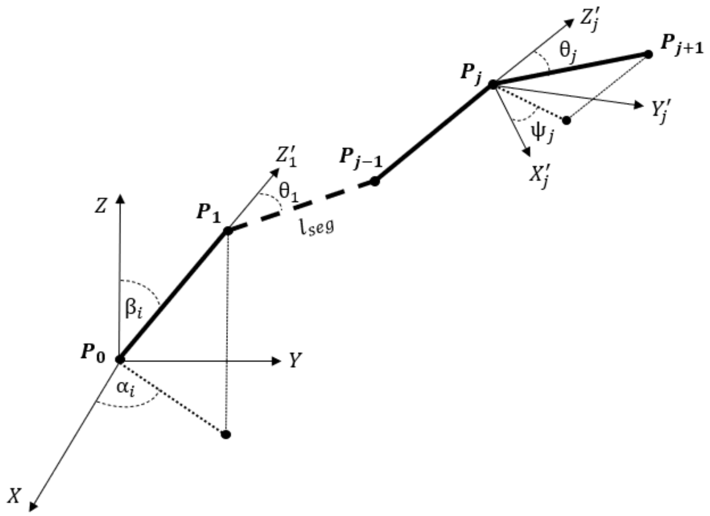

Fig. 4.3 *The schematic diagram of the random curved fiber chain*

Table 4.1 *Description of parameters used in the algorithm*

Parameter	**Description**
L_x, L_y, L_z	x, y, z dimensions of the cubic RVE
α_i, β_i	Azimuth (α_i : (0,2π)) and polar angle (β_i : (0, π)) in global frame of reference, used to define each CNT orientation
θ_{max}	Maximum allowable waviness angle
Ψ_j, θ_j	Azimuth (Ψ_j : (0,2π)) and polar angle (θ_j : ($-\theta_{max}$, θ_{max})) in local frame of reference, used to define each CNT waviness
l_{seg}	CNT segment length/walking distance
N	Number of CNTs to reach certain v_f
v_f	Volume fraction of CNTs inside the RVE
r_{ji}	Relative coordinate vector between two consecutive points of CNT *i*
d_{min}	Minimum distance between two CNT segments (d_{min}=d_{CNT} when all CNTs have same diameter)
W_{max}	Maximum number of iterations to find the next coordinate inside the RVE
I_{max}	Maximum number of iterations to find a way through previously generated CNTs. It is used to avoid the CNT-CNT penetration

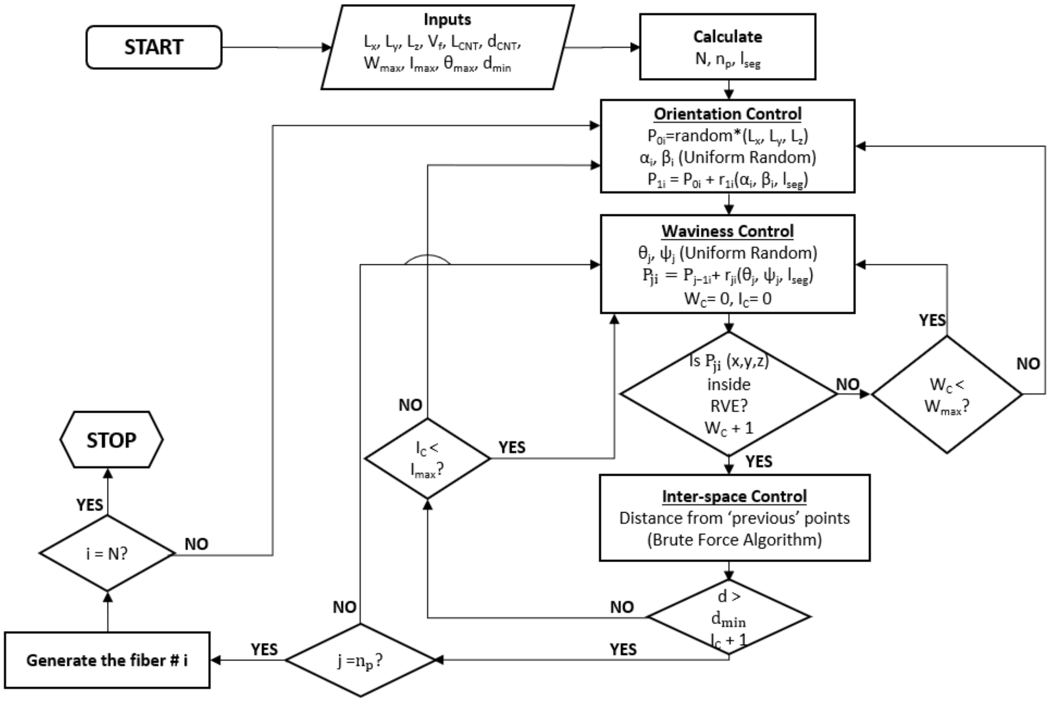

Fig. 4.4 Algorithm flowchart for generating stochastic random fiber chains

Table 4.2 *Morphological Parameters used for the analysis*

Parameter	Distribution	Range			
Diameter (nm)	-	30			
Length (μm)	-	2.1			
Waviness Angles	Uniform Random	Case I	Case II	Case III	Case IV
(θ_{max})		0º	±10º	±20º	±30º
Orientation Angles	Uniform Random	0º-360º (Azimuth angle, α) 0º-180º (Polar angle, β)			
Fiber Dispersion	Uniform	-			

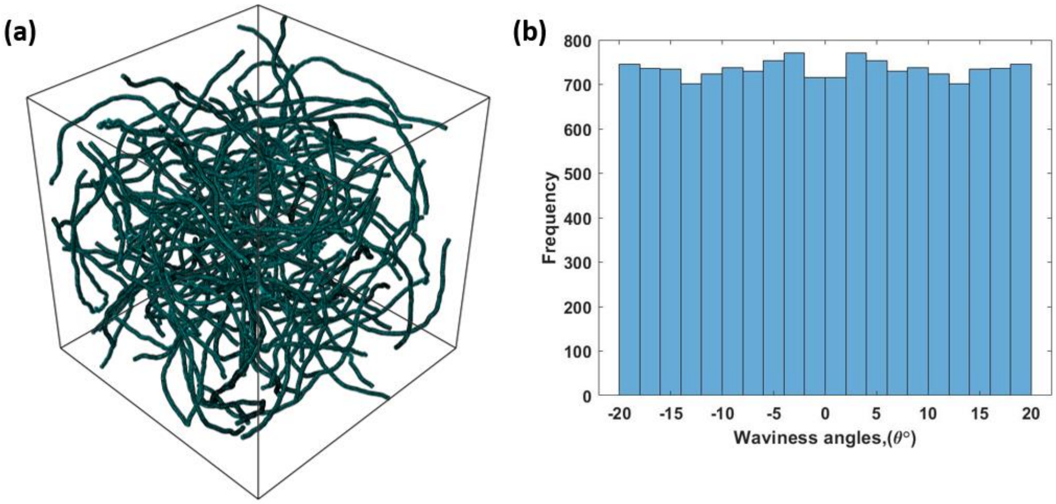

Fig. 4.5 *(a) Meshed wavy CNTs, (b) Histogram of waviness angles used in the model shown on the left*

Based on the available vendor data, the lengths of CNTs can range up to several micrometers. Due to the high computational cost involved in modelling the actual length of CNTs, a parametric analysis can be done to evaluate the critical length, and hence, the critical aspect ratio for the CNTs to be considered for FEA study. The Halpin-Tsai equations modified for the tubular CNT structure [103] can be used to plot the CNT composite modulus as a function of critical CNT aspect ratio (AR=L/D). **Fig. 4.6** shows the dependency of CNT/epoxy nanocomposite on the CNT aspect ratio. It can be reasonably assumed that for a fixed CNT diameter (e.g. d_{cnt} = 30 nm), an aspect ratio equal to or greater than 70 (i.e. 2.1 μm or higher) can efficiently capture the load transfer capacity of the CNTs. The estimated AR value is in good agreement with the previously reported values [94][104].

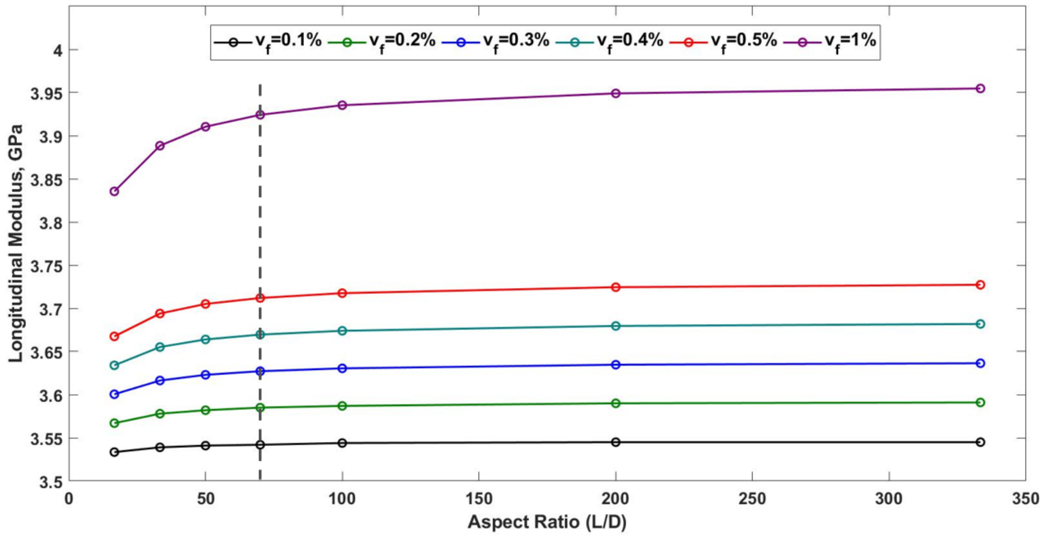

Fig. 4.6 *Effect of CNT aspect ratio on the longitudinal modulus of CNT/epoxy composite*

Finite Element Modelling

2D Random Fiber Mat

We have assumed CNTs to be straight, thin, and isotropic. Furthermore, no distinguished interfaces have been taken into account; there are either fibers or matrix in the model. It is reported that nearly 0.521% volume fraction of CNT in polymer system can lead to rigidity percolation threshold [105][106].We have taken 3.61% fiber volume percentage in present analysis. We chose model (RVE) dimensions to be 151 x 126 pixels.

In order to convert the image (raster form) to FEM readable format (vector format), the obtained image is processed through Scan2CAD [107] and AutoCAD software to convert it to geometry file for Finite Element Analysis (**Fig. 4.7**a). Highlighted part in red color is representing CNTs.

The Final FE model of the RVE (**Fig. 4.7**c) is assembled in ABAQUS 6.16 using Embedded Finite Element Method. This method is used to embed the fibers in matrix.

Embedded elements allow the introduction of CNTs (**Fig. 4.7**a) within a matrix (**Fig. 4.7**b) without removing the matrix material where the fiber resides. This method is convenient since it avoids one to reproduce the complementary matrix part of composite, in case fiber geometry and/or its distribution inside the composite is complex, such as in random fiber composites.

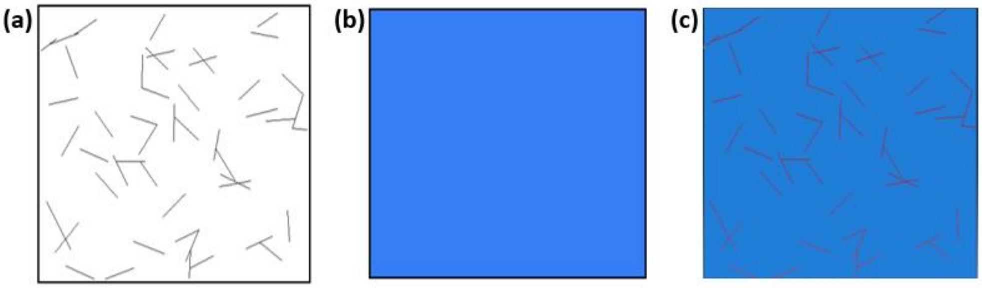

Fig. 4.7 *(a) Random Straight Fibers, (b) Epoxy Matrix, (c) Final Finite Element Analysis Nanocomposite Model*

We chose to use quadratic beam elements for CNTs, and quadratic 8-noded Plane Stress element for matrix to mesh our nanocomposite model. For mesh convergence, 1126, & 36000 elements were sufficient for fibers and matrix, respectively. To increase the mesh density in the vicinity of fibers, partition command is used before meshing. This helps in creating more elements close to fiber/matrix interface in order to capture the response. Input properties of CNTs and Epoxy matrix are listed in **Table 4.3.**

Three-dimensional Computational Model

Three-dimensional representative volume element (RVE) models consisting multiple solid/effective CNT fibers are developed and analyzed to evaluate the elastic properties of CNT/epoxy composites for a given set of morphological parameters shown in **Table 4.2**. The RVE dimensions are chosen to be 2500 nm x 2500 nm x 2500 nm so that finite element models are not computationally intensive but are large enough to represent the CNT composite/accommodate the CNT morphological parameters, such as orientation, waviness, dispersion and distribution.

The wavy fibers are generated using the python script within the Abaqus environment. The matrix of chosen RVE dimensions can be then generated, and the fibers are embedded in the matrix using Embedded Element Method[108]. This method allows to embed the fibers with complex geometries inside the matrix without generating the degenerated matrix geometry. It decreases the complexity of meshing the degenerated matrix. The stiffness matrix of the embedded region is calculated by superimposing the fiber and matrix stiffness for the embedded nodes.

Epoxy is used as a matrix material with E_m = 3.5 GPa and v_m = 0.32. To obtain the elastic properties of CNT fiber, the method proposed by Thostenson et al. [109] is used (Equation (4.3)), which leads to E_{CNT} = 1.1 TPa and v_{CNT} = 0.3. The multiwalled carbon nanotube (MWCNT) is modelled as an effective solid fiber with the same deformation behavior and same length (l) and diameter (d) as that of the MWCNT [109]. It is based on the assumption that an applied external force (F) on the CNT and the effective (solid) fiber will result in the condition of iso-strain.

$$E_{eff} = \frac{d_o^2 - d_i^2}{d_o^2} E_{CNT} \tag{4.3}$$

where d_i is considered to be nearly zero, as MWCNT is assumed to be made of several concentric cylinders with d_o (=~30 nm). Both CNT and matrix are considered to be perfectly bonded together, assuming that for lower strain values the interfacial stresses do not lead to debonding of CNT/epoxy interface [110]. All the phases are assumed to be homogenous, isotropic and linearly elastic.

Non-linear brick (C3D20) and tetrahedral elements (C3D10) are used to discretize the CNTs and matrix, respectively. The mesh convergence study is performed to choose the optimum element size for fibers and matrix. To evaluate the elastic constants, a displacement resulting in 1% strain is applied on the face perpendicular to the direction of calculation of elastic moduli, while keeping the opposite face fixed. Necessary accommodations are made to allow for the poison's ratio effect in the loading in transverse directions. The effective modulus of the composite is obtained from the ratio of average normal stress developed to the applied strain (ΔL/L).

Later, to evaluate the effect of CNT/matrix interphase on the elastic modulus of the composite, a concentric layer of interphase material around each CNT is generated (**Fig.4.9**(b)). The cases of 'hard' (E_i =110%–175% E_m) as well as 'soft' (E_i =10%–75% E_m) interphase are considered. A model with interphase properties (E_i = E_m) equal to the matrix properties is also considered for the sake of comparison. It was assumed that the poison's ratio of the interphase was approximately equal to that of the matrix. As the interphase modulus (E_i) is considered comparable (10%–175% E_m) to the matrix modulus (E_m), the embedded element technique cannot be used [108]. Due to such limitations of embedded element technique, a degenerated matrix has to be generated. Finally, CNTs, interphases and the degenerated matrix (**Fig.4.9**) can be tied in order to generate the three-phase nanocomposite model. The volume fraction of the CNT fibers, interphase and matrix were determined to be nearly 0.1, 0.47, and 99.43%, respectively. Both the CNTs and interphases are meshed using non-linear brick (C3D20), while tetrahedral elements (C3D10) are used to discretize degenerated matrix material. The mesh convergence study is performed to choose the optimum element size for fibers, interphases, and the matrix. In order to maintain the accuracy of the results, a relatively finer mesh is used at the CNT interphases and their vicinity. Previously described boundary conditions are used to calculate the elastic modulus of the three-phase model.

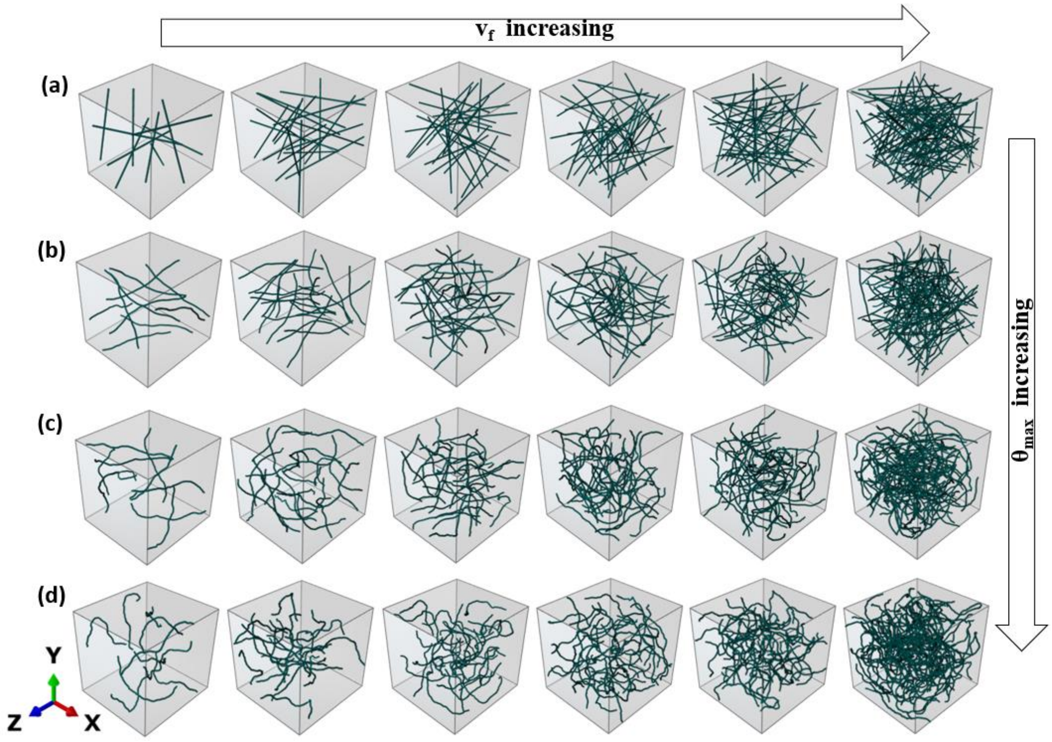

Fig. 4.8 *RVEs generated using Python Script for v_f ranging from 0.1% to 1% at (a) θ_{max} = 0º, (b) θ_{max} = 10º, (c) θ_{max} = 20º and (c) θ_{max} = 30º*

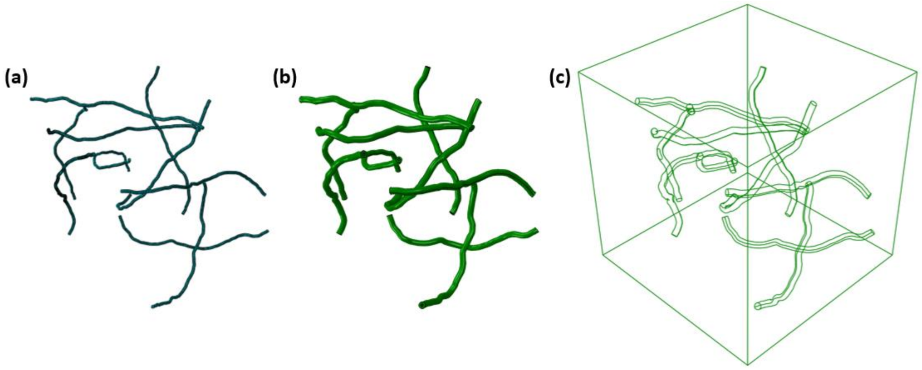

Fig.4.9 (a) *CNT fibers, (b) hollow CNT/epoxy interphases and (c) degenerated matrix*

Results and Discussion

The results obtained from our Computational Model have been compared to the Halpin-Tsai Theoretical Model. Approach is discussed below:

Theoretical Model:

Halpin-Tsai model equations have been used for a long time to predict the properties of composites reinforced with aligned short fibers[111]. These equations were originally developed for continuous-fiber composites [103]. Halpin-Tsai used semi-analytical method to reduce the equations for aligned short fiber composites. Lavengood and Goettler [112] later used stress transformation equations and integrated the equations over a random distribution of fiber orientations and obtained the equations (**4.5**)-(4.7).

For aligned short fiber composites, elastic properties are given as

$$C = C_m \frac{1 + \xi \eta V_f}{1 - \eta V_f} \quad where\ \eta = \frac{C_f / C_m - 1}{C_f / C_m + \xi} \tag{4.4}$$

where

C= Composite Modulus, E_1, E_2, G_{12}

C_f= Fiber Modulus, E_f or G_f

C_m= Matrix Modulus, E_m or G_m

ξ = a parameter depending on the fiber geometry, packing geometry, and loading conditions

For composites reinforced with randomly oriented fibers in 2D plane, the Effective Elastic Moduli are given by Lavengood [112]:

$$\boldsymbol{G_{2D,Random} = \frac{1}{8}E_L + \frac{1}{4}E_T} \quad (4.5)$$

$$E_{2D,random} = \frac{3}{8}E_L + \frac{5}{8}E_T \quad (4.6)$$

$$E_{3D,random} = \frac{1}{5}E_L + \frac{4}{5}E_T \quad (4.7)$$

where E_L and E_T are the longitudinal and transverse modulus obtained from the Halpin-Tsai equations [103].

2D Computational Model:

Appropriate Essential and Natural Boundary Conditions are provided to the complete model to obtain the converged values of desired mechanical properties, such as Young's modulus, Poisson's ratio, and shear modulus. The elastic constants obtained for the RVE from the simulation are given in **Table 4.3**.

Row 5 in **Table 4.3** shows the Elastic constants obtained from Theoretical Model discussed above.

Table 4.3 *Computational and Theoretical Model Results*

Material	**Model**	**V_f (%)**	**E_1 (GPa)**	**E_2 (GPa)**	**ν_{12}**	**ν_{21}**	**G_{12}**
Matrix	-	0	3.5	3.5	0.32	0.32	1.325
CNT	-	0	700	700	0.16	0.16	301.72
Nanocomposite	Computational	3.61	4.08	3.9	0.332	0.315	1.47
Nanocomposite	Theoretical	3.61	5.05	5.05	0.368	0.368	1.846
Error (%)	-	-	19	22.7	9.7	14.4	25.5

It can be observed that the values of elastic constants obtained from Halpin-Tsai equations are slightly higher than that predicted by our nanocomposite model. It might be due to the fact that the Theoretical model used here is formulated based on various assumptions, such as fibers and matrix are perfectly bonded, etc. Halpin-Tsai model was chosen for comparison due to its simplicity. However, other modified models, such as Nielsen Model [113] can be employed, with added complexity.

A two-dimensional random fiber composite can be treated as quasi-isotropic material, i.e., its in-plane properties will be nearly identical in all the directions. It can be observed that properties obtained from FE analysis in 1 direction are practically identical to that in 2 direction.

Young's modulus of nanocomposite is nearly 15 % greater than that of matrix material. Poisson's ratio is slightly unchanged. Error of approximately 9-25 % is observed between the Computational Model and Theoretical Model results.

3D Computational Model

To analyze the effect of CNT waviness on the moduli of the nanocomposite, six different cases with volume fraction varying from 0.1 % to 1 % are chosen. Since the CNTs are oriented in random fashion within the matrix, the elastic modulus in x, y, and z-direction are expected to be nearly equal, i.e., the composite will be quasi-isotropic [112]. **Fig. 4.10** shows the stress-strain response for the model with v_f = 1% and θ_{max}=20º for uniaxial loading in x, y, and z-direction. It can be noticed that the model is quasi-isotropic. The slope of the respective curves represents the effective elastic modulus of the composite in the loading direction. Similar approach is used for other models and the obtained values of effective moduli are plotted in **Fig. 4.11**. **Fig. 4.11** shows that for a given volume fraction, the moduli of the composite decreases as waviness angles increase.

The error scale denotes the deviation of elastic moduli in x, y, & z-directions. The elastic modulus seems to decrease in a non-linear fashion as the θ_{max} is increased. This indicates that for a given volume fraction, a major decrease in the elastic properties is observed when the CNT becomes waviness angle decreases from 0^0. Properties continue to decrease at a reduced rate as the θ_{max} is increased further.

It can be noticed that for the lower θ_{max} values, the higher volume fraction models generated using the current algorithm are slightly deviated from complete randomness in the fiber orientations (**Fig. 4.12**). It is due to the difficulty to insert more number (i.e., high v_f) of randomly oriented and relatively straight fibers of certain length (e.g., 2.1 μm) in a comparable RVE size (here, 2.5 μm). However, as the increase in the waviness of the fibers lead to decrease in the fiber wavelength, more number of fibers of total length comparable to the RVE size can be fitted randomly, which leads to the better quasi-isotropic behavior of the composite even at higher volume fractions (**Fig. 4.11**).

The Halpin-Tsai model equations are used to compare the elastic moduli values obtained from the computational model. The Lavengood-Goettler equations were obtained for two-dimensional random aka “random-in-a-plane” (Equation(4.6)) and three-dimensional random fiber distribution (Equation(4.7)). **Fig. 4.12** compares the values obtained by computational model for straight CNTs with the discussed 2D and 3D random fiber composite theoretical equations.

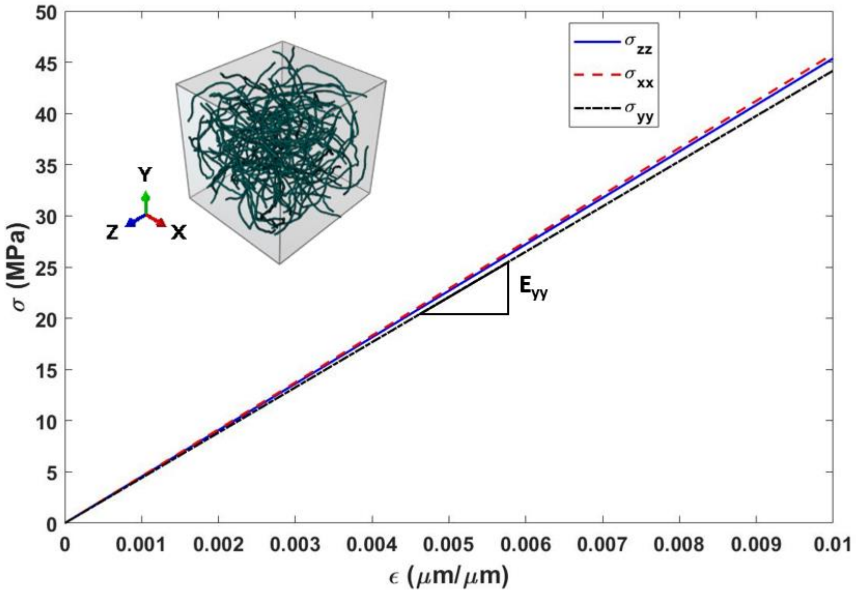

Fig. 4.10 *Stress-strain response for unidirectional loading in x, y and z-direction*

(Model: v_f = 0.1% and θ_{max}=20º)

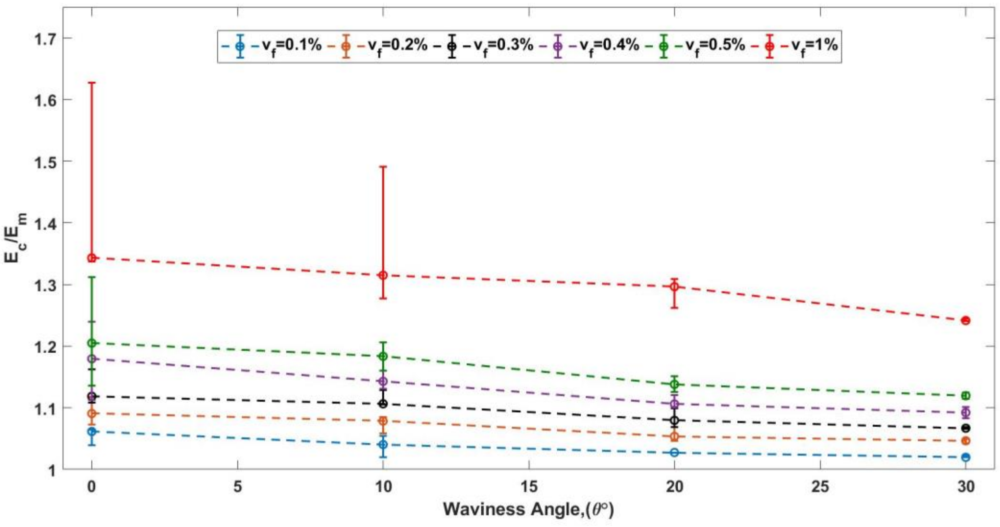

Fig. 4.11 *Effect of waviness angle on the modulus of CNT composites*

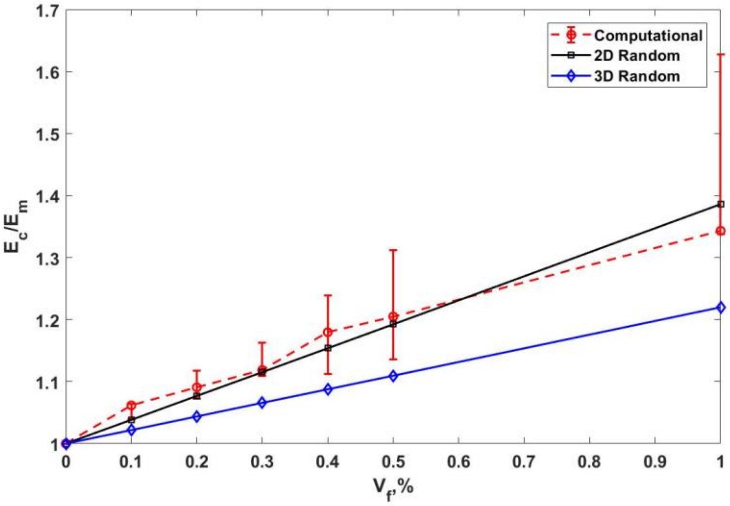

Fig. 4.12 *Comparison of computational and theoretical models*

AFM and SEM studies performed by Bhuyian et al [95] confirmed the presence of voids at the CNT/matrix interphase, which leads to ineffective load transfer from matrix to CNT. They reported the interphase thickness to be nearly 20 nm [94]. In this study, we have considered an interphase layer of 20 nm thickness with the reduced modulus that is inserted between CNT and matrix. To evaluate the effect of interphase modulus on the overall composite modulus, a FEA parametric study has been performed for the case with v_f = 0.1% and θ_{max}=20º (**Fig.4.9**). Interphase modulus is varied from 10%-175% of the matrix modulus. In the case of a 'soft' interphase, it can be noticed that the decrease in effective modulus of the interphase indicates the deterioration of the CNT/epoxy interphase. Whereas for the 'hard' interphase representing the increased polymer density and surface functionalization/modification of the fiber, leads to increase in the effective properties of the composite. **Fig. 4.13** shows the trend of variation in the composite modulus and average stresses developed in CNTs as the interphase modulus is varied. The right axis represents the average stresses developed in the CNT fibers at a given interphase modulus, which is further normalized by the average stresses developed in the CNT fibers when the interphase modulus is same as the matrix modulus (i.e., $E_i/E_m=1$). It can be noticed that the composite modulus decreases abruptly when the interphase modulus is decreased to 75% of E_m due to the decrease in load transfer from matrix to CNTs, which is also indicated by the decrease in the average stresses developed in the CNT fibers. Later with the increase in voids in the interfacial region (i.e. the effective interphase layer modulus decreases), the effective composite modulus further decreases. It can be noticed that for E_i equals 10% of E_m, the effect of CNT reinforcement is barely felt by the composite ($E_C/E_m \sim 1$), while the stress ratio drops down by approximately 52%. On the other hand as the interphase stiffens ($E_i/E_m>1$), the composite modulus increases. **Fig. 4.13** shows the increase in average stress generated in CNT fibers as the interphase stiffens. This confirms that the load transfer from the matrix to the fibers is better as interphase gets stiffer. It can be noticed that the composite modulus is more sensitive to the 'soft' interphase.

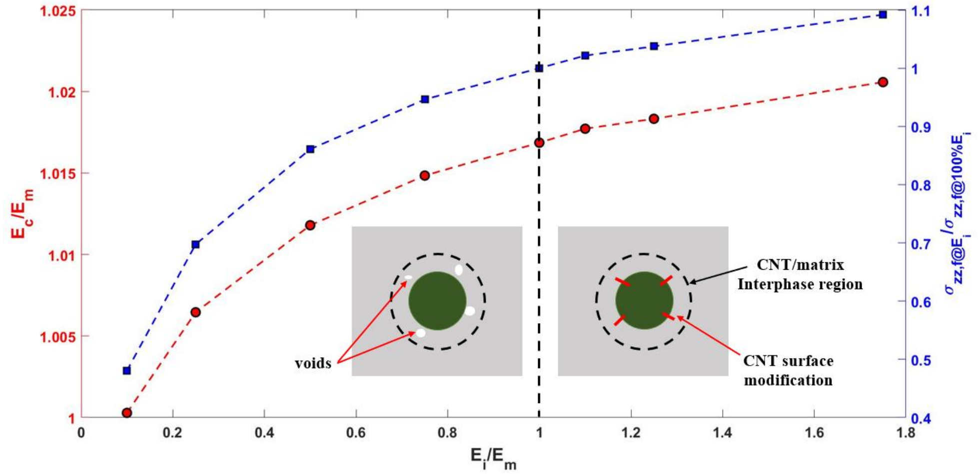

Fig. 4.13 *Effect of CNT/epoxy interphase modulus on (left axis) modulus of CNT composites and (right axis) average normal stresses (σ_{zz}) in the CNT fibers (Model: $v_f = 0.1\%$ and $\theta_{max}=20^o$)*

Conclusion

The study performed in this chapter indicate that MATLAB generated random fiber model can be used computationally in Finite Element Analysis as an excellent tool for predicting elastic constants of CNT reinforced polymer matrix. Young’s modulus of nanocomposite is nearly 15 % greater than that of matrix material. Possion’s ratio is slightly unchanged. Error of approximately 9-25 % is observed between the Computational Model and Theoretical Model results. Quasi-isotropic behavior of random fiber mat is observed. It can be noted that this model can be applicable for any random fiber composite.

In order to build a fully predictive model, further efforts are made to include fiber/matrix interfaces, fiber waviness, etc. These enriched models can be utilized to study the effect of interphase properties and CNT waviness on the composite elastic constants.

Second part of this chapter has been focused on developing a computational method to include stochastic distributions of the CNT waviness and orientation in building finite element predictive models for mechanical properties of random/aligned carbon nanotube composites. Thus far, efforts have been made to study the effect of waviness of CNTs towards the elastic moduli for a set of varied volume fractions of 0.1 % to 1 %. For each volume fraction, finite element models of randomly oriented CNTs for three different θ_{max} values are constructed. These models are analyzed to predict the effect of increase in the waviness angles of the CNT fibers on their mechanical properties. The obtained results suggest that CNT waviness plays a key role in deciding the elastic properties of the CNT based composites. Hence due to their wavy morphology, the inefficient load transfer between CNT fiber and matrix results in the overall decrease in their mechanical properties by 4-8%.

A three-phase interphase model is generated to study the influence of ‘soft’ as well as ‘hard’ interphase on the elastic modulus of the composite. The interphase model suggests that the composite modulus is further compromised as the interphase modulus reduces by up to 2.5% for 0.1% CNT v_f due to the presence of voids at CNT/epoxy interface (‘soft’ interphase). Whereas the composite modulus increases as the interphase becomes a ‘hard’ interphase. It is due to the increase in the load transfer from matrix to the fiber, which resulted in increased average stresses generated in the CNT fibers. It is noticed that the composite modulus is more sensitive to the ‘soft’ interphase.

While in the current study only the effect of CNT waviness and CNT/matrix interphase is emphasized, the developed algorithm can be used to quantify the effect of different morphological parameters, such as CNT agglomeration. Moreover, the present model can be extended by defining weak inter-fiber bonding (cross-links) interactions between the CNTs, which can aid in modelling the CNT network mechanics similar to that studied by Picu et al [114]. This can allow for evaluating the effect of fiber entanglement on the mechanical properties of the CNT composites. However, this is planned as our future work.

CHAPTER 5 THERMAL-MECHANICAL PROPERTIES OF SILICA NANOFIBER NETWORK

Introduction

Silica dioxide (silica, SiO_2) grows naturally on silicon in the presence of oxygen, at room temperature, or under thermally controlled conditions. It possesses excellent mechanical, thermal and optical properties, and hence is routinely used in a wide variety of technological applications. It is a popular material used in manufacturing micro- and nano-electronic devices [115]–[118], optical fibers for telecommunications [24][25], and glass fibers to form fiber-reinforced polymer composites [119]. A fundamental understanding of mechanical properties of silica nanowires can help increase their reliability when integrated into functional nanodevices. Silica has more than 40 different crystalline SiO_2 polymorphs [120][121]. They possess different bond lengths and bond angles, leading to variation in crystal/lattice symmetry and density among them. More details about their crystalline structures can be found elsewhere [122].

In the bulk form, silica is known to be a brittle material [123][124]. However, recent experimental [26] and molecular dynamics [26][27] studies have reported a brittle-to-ductile transition (BDT) in their behavior as the sample diameter reduces towards the nanoscale dimension. A variety of experimental studies available in the literature report different values of the mechanical properties depending upon the methods used to synthesize them. Ni et al [125] used Chemical Vapor Deposition (CVD) to synthesize the silica nanofibers ranging from diameters 50-100 nm and reported their stiffnesses to be $E = 76.6 \pm 7.2$ GPa. Similar values for the modulus E = 68-76 GPa was reported by Silva et al [126]. The nanofibers in this study were manufactured using a 2-step drawing technique. Due to limited availabilities in conducting reliable experiments at the nanoscale, many studies are done using molecular dynamics (MD) simulations. For example, Yuan et al [127] obtained the mechanical properties of silica nanofibers at different state of strains, loading rate, cooling rate used during annealing simulation, and the working temperatures. They have found that the properties of the nanofibers vary significantly on these parameters. Several other groups have studied the mechanical properties of silica nanowires at different diameters using BKS potential [128]. Zhang et al [129] prepared nanofiber models by “cutting” method and used reactive force-field (ReaxFF) to evaluate the elastic modulus of amorphous silica NFs, and reported the Young’s modulus in the range of 19-30 GPa for diameters ranging from 2.23-10.23 nm. It is evident that the “cutting” method used in previous MD studies [130]–[132] can generate more surface coordination defects, which in turn results in the lower mechanical properties. On the contrary, the “casting” method is known to generate more natural and stress-free surface-state [127]. As such, in this study we have opted to use the “casting” simulation method. To the best of our knowledge, no previous study is conducted to evaluate the mechanical properties of silica nanofiber prepared by “casting” method using reactive force field.

Further, the electrospun silica NF mats (**Fig. 5.1**a) can have different arrangement and hence interactions of the NFs, which may contribute towards the overall network constitutive law [133]. Paper, damping materials, bird nests, respiratory mask filters, insulation materials, etc. are the most common examples from the everyday life. In the present study, it is hypothesized that the undercoordinated atoms present on the surface of the NF can form an interface when placed at a certain distance ($d^{\parallel}$) in silica NF mat (**Fig. 5.1**c). Similarly, at the junction of the two or more NFs (**Fig. 5.1**b), a significant load transfer can occur due to the covalent bonding between dangling bonds. The newly-formed interfaces can influence the structure-property relationship of the silica NF mat, which could be difficult to obtain from the experimentation. The load transfer between the two NFs in either configuration can depend on (a) atomic interaction between the two fibers and (b) topology of the nanofibers leading to micromechanical interlocking between the two NFs. Such interfacial load transfer between the silica NFs is a new area of research to be explored in this article. Such arrangement of aligned NFs and NFs junction can ultimately influence the electronic properties [134], mechanical behavior [134], or overall optical properties of the electrospun mat.

ReaxFF force-field [135][136] is based on the bond order/bond length relationship and hence can mimic the chemical reaction by automatic bond breaking and formation. This capability is utilized in the current study to accurately obtain the amorphous structure of bulk silica and silica NF. In addition, ReaxFF also allows for the natural chemical bond formation between the under-coordinated atoms at the NF interface in aligned and junction models, and hence can help characterize the NF interface.

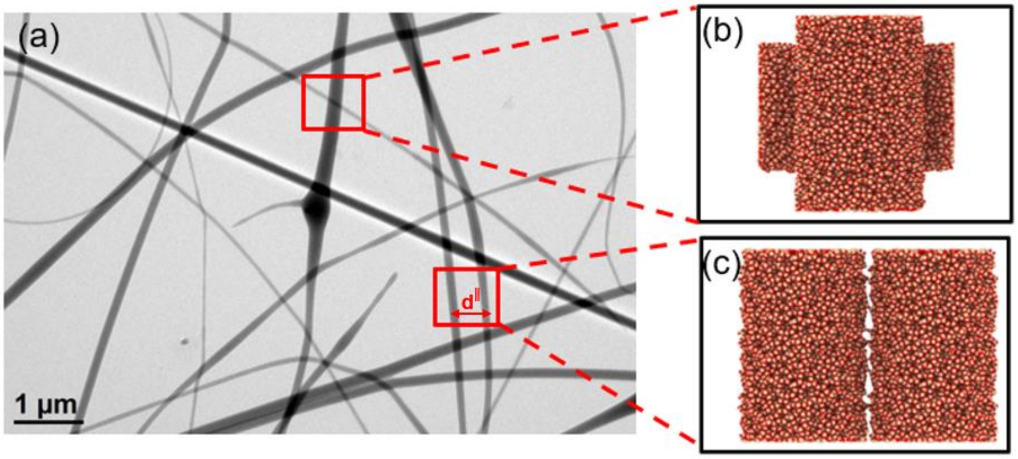

Fig. 5.1 *(a) TEM image of electrospun Silica NF Mat, (b) Molecular model of NFs junction and (c) aligned NFs*

It is also of significance to study the thermal stability of silica NWs to ensure their structural integrity and functionality at raised temperatures which might be encountered during their application. For instance, the severe geomagnetic disturbance (GMD) events of unknown magnitude can induce a significant current in the electrical powerlines, which is sufficient to perturb the thermal and in turn, mechanical stability of the electric transformers, which might lead to their catastrophic failure eventually leading to a safety hazard costing human and capital investments.

Similar to their mechanical properties, size effect in nanomaterials has been reported to influence their thermal stability as well [137][138][139]. Surface energy γ is the excess energy that is supplied to a material when a new surface is created from the bulk. It is associated with the fact that when a surface is created, the atoms at the surface plane experience different atomic arrangement when compared to the interior atoms. Thus, two different states of stress exist across the surface layers and in the remaining bulk material. The stress at the surface is known as "surface stress σ_{ij}" which is required to balance by the interior of the material during equilibrium. It can be noted that as both γ and σ_{ij} are associated with material surfaces, their magnitude is related to the surface/volume ratio of the materials. As at nanoscale this fraction value becomes significant, which leads to the size dependent material behavior. Melting point diffusion (MPD) is a classical example of the "surface effects" in the nanoscale. MPD is the phenomenon that is frequently observed in the nanostructured materials [137][138][139], which implies that due to the "surface effect" the melting temperature (T_m) of the nanowires decreases as their size decreases. This implies that the bulk material usually has higher T_m values compared to that of the nanowires. Such effect has been analytically predicted by Pawlow [138]. While originally developed for spherical particles, it can be generalized for any shape of nanostructured materials with an appropriate geometric factor. Equation (5.1) shows such generalized model for MPD.

$$\frac{T_m(r)}{T_m^{bulk}} = 1 - \left(\frac{1}{r}\right)\frac{B}{H_m^{bulk}\rho_s}\left\{\gamma_s - \gamma_l\left(\frac{\rho_s}{\rho_l}\right)^{\frac{2}{3}}\right\} \tag{5.1}$$

where $T_m(r)$ is the size-dependent melting point of a material with characteristic size *r*, T_m^{bulk} is the bulk melting temperature, *B* is the geometric factor, H_m^{bulk} is the bulk heat of fusion, *ρ* is the density and *γ* is the surface energy. The subscripts *s* and *l* correspond to solid and liquid state of materials, respectively.

Direct heating single-phase method is previously used to evaluate the melting temperature and structure transition of crystalline copper nanorods [140][141] and gold nanowires [137].

The melting temperature calculated using singe-phase method has been reported to be exceedingly greater than the experimental values due to the superheating of the material using MD methods, especially when the surface effect is not considered (homogenous melting). More discussion can be found in [142][143]. The two-phase methods such as Solid-liquid coexistence method has been reported to provide more realistic values[142][144]. However, the latter method is computationally more intense.

Sun et al [145] used single-phase method to step heat the iron nanoparticle and adjusted the results obtained from the MD simulations based on the recommendations from [143]. Other researchers used two different heating rates to melt the crystalline nanowire while accommodating for a smaller heating step near the expected melting region [139][146].

In this study, ReaxFF is used to produce amorphous structure of bulk silica glass and silica nanofiber through annealing process. Tensile tests are conducted to evaluate their mechanical properties at two different strain rates of $\dot{\varepsilon}$= 2.3 x 10^9 s^{-1} and $\dot{\varepsilon}$= 2.3 x 10^{10} s^{-1}. Thereafter, the aligned NF model with varied inter-space distance ($d^{||}$=1.5 Å, 3.5 Å, 6.5 Å) and the junction model is studied. To gain further insight into the load transfer at the interface of two NFs, NF pullout simulations are conducted for aligned NF configurations. Large-scale Atomic/Molecular Massively Parallel Simulator (LAMMPS) [28] code is used to perform the MD simulations. OVITO [58] is used for model visualization.

Computational details

In this study, MD simulations were performed using LAMMPS open source code [28] and the reactive force-field (ReaxFF) parameters developed by Forgarty et al [136][147]. The force-filed parameters have been previously used to generate the amorphous structure of bulk silica material and to further investigate their mechanical properties.

Bulk amorphous silica

Ideally in the crystalline silica, a silicon (Si) atom is connected with four oxygen (O) atoms making a SiO_4 tetrahedral structure. The connecting oxygen atoms are located at the vertices of a tetrahedron with silicon atom at its center. Further, the oxygen atoms are shared among other neighboring tetrahedrons, which yields in net chemical formula of SiO_2 for silica. Such tetrahedrons are packed uniformly inside a box of chosen dimension using Packmol [148] while maintaining 2:1 stoichiometric ratio for silicon to oxygen. To obtain the amorphous structure, the system is heated at 4000 K for 200 pico seconds (ps) using NVT (canonical) ensemble. Further to mimic the annealing process, the bulk silica material is cooled down to 300K at rate of 10 K/ps using NVT time integrator. After this, the system is equilibrated for 150 ps each under NVT and then NPT (isothermal-isobaric) ensemble at 300 K in order to release any build up stresses during the annealing process. Periodic boundary was maintained in all three directions during the described simulation steps. The final model dimensions after NPT equilibrium are 5.05 nm x 5.05 nm x 4.3 nm containing 7056 atoms. Based on a study performed by Chowdhury et al [124], choosing a big enough model size is of particular importance to capture the post-peak behavior of the stress-strain plot.

The final density achieved is 2.14 g/cc, which is in good agreement with the previously reported values using ReaxFF force-field [136][124]. **Fig. 5.2** shows the equilibrated amorphous structure of bulk silica and its radial distribution function (RDF) after NPT equilibrium.

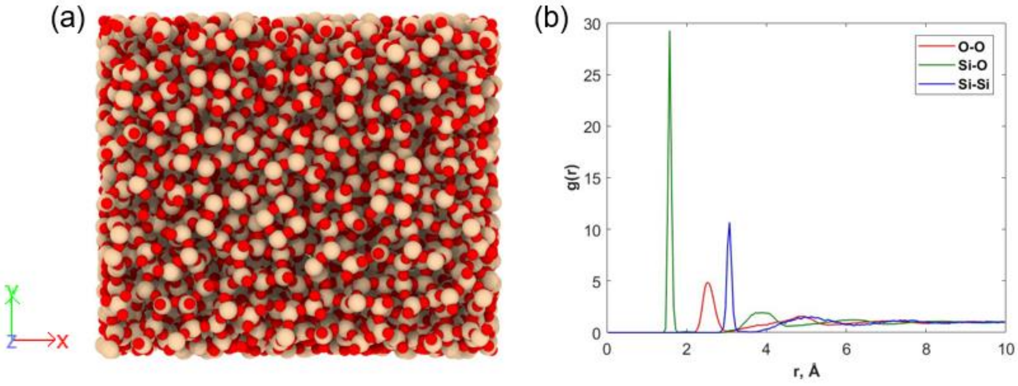

***Fig. 5.2** (a) Amorphous bulk silica (b) radial distribution function at equilibrium*

Unhydrated/Pristine amorphous silica nanofibers

Silica nanowire structure was created by melting the 21681 atoms β-cristobalite silica at 4000 K for 200 ps in a cylindrical container with a repulsive wall to simulate the “casting” method. The periodic boundary is used in the longitudinal direction of the cylinder. An NVT quenching scheme from 4000 K to 300 K was performed to anneal the silica liquid at a cooling rate of 18.5 K/ps. A timestep of 0.5 fs was used. Upon the removal of cylindrical constraint, the sample was equilibrated at 300 K for 150 ps using NPT ensemble at atmospheric pressure condition. This helped reducing the buildup stresses in the material system by allowing a change in its dimensions. After the NPT equilibrium, the average nanowire diameter was nearly 63.73 Å. **Fig.5.3** shows the equilibrated amorphous structure of silica nanofibers. **Table 5.1** provides the details of NF considered in this study. It can be noticed that the density of the nanowire is increasing with the decrease in NF diameter, which is a direct result of increasing surface effect as the NF size goes down [127][128]. Typically as the NF size increases, the surface effect decreases and the density of the NF tends to converge at the corresponding bulk material density ($\rho_{bulk,silica}$ = 2.2 g/cc).

The density obtained with the ReaxFF potential was 2.287 g/cc, which is in good agreement with the previous MD [126][129][136] and experimental value of 2.2 g/cc [149].

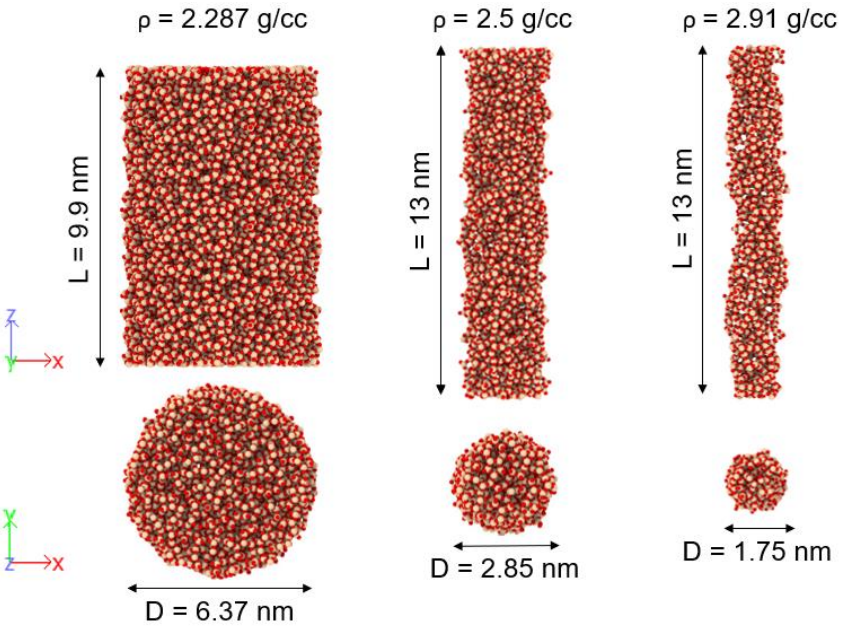

Fig.5.3 *Longitudinal and sectional view of silica nanofibers of varied cross-sections (Color Scheme: CPK)*

Table 5.1 *Atomistic details of silica nanofibers*

Diameter, nm	Atoms	Length, nm	Density, g/cc
6.373	21681	9.9	2.287
2.85	6240	13	2.5
1.75	2772	13	2.91

Hydroxylated amorphous silica NW

In order to hydroxylate/pacify the silica NF, the equilibrated pristine NF structure is allowed to react with the water molecules at 650 K temperature under NVT conditions for 500 ps using a 0.1 fs timestep. It is recommended to use NVT ensemble instead of NPT, as the difference in compressibility of a-SiO_2 and water would lead to unrealistic pressure effects. The elevated temperature (T=650K) is used to promote the hydronium ion (H_3O^+) formation which is critical to the silanol (Si-OH) formation [150]. The simulation was continued until the system maintained thermal equilibrium with the heat bath. The chemical reaction between the water and under-coordinated atoms on silica NF surface took place primarily in the beginning of the simulation, leading to silanol (Si-OH) and hydroxyl (O-H) formation. More detail on the chemical reaction can be found elsewhere [136]. After equilibrating the system using NVT ensemble, the unreacted water molecules were removed, and pacified NF was equilibrated at 650 K to obtain the stable configuration. Thereafter, the system temperature was then brought to 300 K at a cooling rate of 3.5 K/ps for nearly 100 ps. The hydroxylated NF was then equilibrated under NVT and afterwards NPT conditions at 300 K until the thermodynamic equilibrium is reached. Periodic boundary conditions were maintained in all three directions while extending simulation domain in x and y directions. **Fig.5.4** shows the final snapshot of the NPT equilibrated hydroxylated NF. **Fig.5.4**(b) shows the RDF data for Si_{NW}-O_{water}, indicating the bond formation between Si_{NW} and O_{water} (first peak positioned at R_{Si-O} = 1.575 Å). **Fig.5.5** compares the undercoordinated atoms present at the NF surface before and after the hydroxylation. Nearly 90% of the undercoordinated atoms at NF surface are pacified.

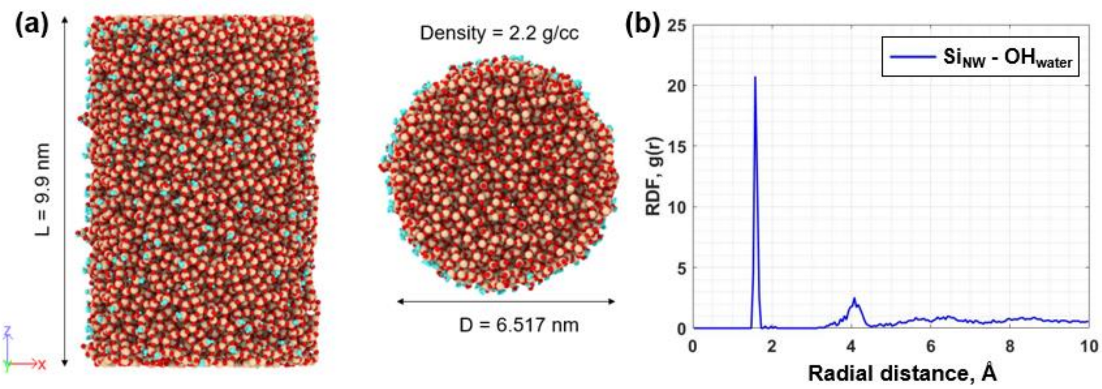

Fig.5.4 *(a)Longitudinal and sectional view of hydroxylated silica nanofiber (Cyan color shows H and O atoms from water), (b)* Si_{NW}*-*O_{water} *RDF at 650 K*

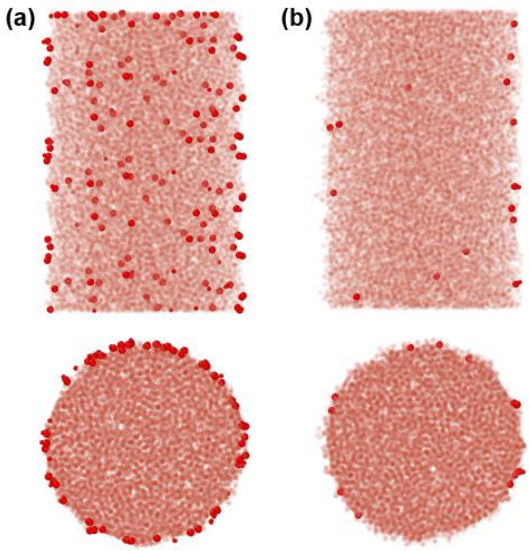

Fig.5.5 *(a) Unhydroxylated/Pristine NF, (b) Hydroxylated NF (Atoms in red represent undercoordinated atoms at the NF surface)*

CALCULATION OF NANOFIBER RADIUS

The average NF diameter can be calculated by dividing it into sections of 0.3 nm thickness in axial direction (z-direction) and identifying the outmost atoms of these sections in x and y-direction to calculate the diameters for each section. Further, the section diameters can be averaged to obtain a final average diameter for the NF [151][152].

Nanofiber Mat

Aligned silica nanofiber mat

Already equilibrated Silica fibers can be arranged in the parallel (**Fig. 5.6**) and perpendicular (**Fig. 5.8**) configuration to represent the arrangement of silica nanofibers in a nanofiber mat.

In order to prepare parallel/aligned nanofiber system, the previously prepared and equilibrated amorphous silica nanofibers are placed at an average distance, $d^{\parallel}$ from each other. The periodic boundary conditions are maintained in all three directions while extending the simulation domain in the X and Y-direction. The system is minimized and then equilibrated for nearly 250 ps in NPT ensemble to allow the bond formation between the dangling bonds or undercoordinated surface atoms in the vicinity of one another. After equilibrium, tensile loading can be applied to the system to observe the stress-strain behavior of the silica nanofibers in the chosen arrangement. Additionally, the pullout simulations will be performed to understand the load transfer between the two nanofibers due to bond formation between the undercoordinated atoms.

As the equilibrium Si-O bond length is reported to be nearly 1.56 Å [136], the values of $d^{\parallel}$ are chosen as 6.5 Å, 3.5 Å, and 1.5 Å. **Fig. 5.6 Fig. 5.6** Longitudinal and sectional view of aligned silica nanofiber mat with average (a) $d^{\parallel}$ = 6.5 Å, (b) $d^{\parallel}$ = 3.5 Å, (c) $d^{\parallel}$ = 1.5 Åshows the final equilibrated structures of the listed cases. For $d^{\parallel}$= 1.5 Å (**Fig. 5.6**c), as the two NFs are placed within the equilibrium value of Si-O bond length, the undercoordinated Si and O atoms at the NF surface can form significant number of covalent bonds at the interface. Whereas for $d^{\parallel}$= 3.5 Å (**Fig. 5.6**b), some level of Si-O bonding is observed due to the surface topology of the NF. Further, it can be noticed that no Si-O bond is formed for the $d^{\parallel}$= 6.5 Å (**Fig. 5.6**a), as the NFs are farther apart.

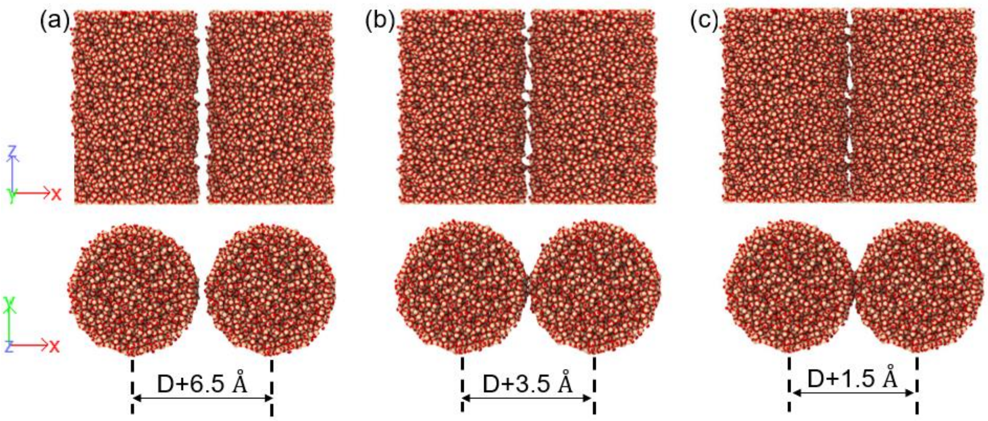

Fig. 5.6 *Longitudinal and sectional view of aligned silica nanofiber mat with average (a) $d^{\parallel}$ = 6.5 Å, (b) $d^{\parallel}$ = 3.5 Å, (c) $d^{\parallel}$ = 1.5 Å*

The RDF between two atomic species (Si and O) is defined as given by equation (5.2).

$$g(r) = \frac{N(r)}{4\pi r^2 \rho \delta r}, \tag{5.2}$$

where *N(r)* is the number of O atoms in the shell between *r* and *r+δr* around the Si atoms and *ρ* is the number density of O atoms, taken as the ratio of the number of atoms to the volume of the simulation cell. **Fig. 5.7** plots two different type of RDF values. **Fig. 5.7**a shows the intra-fiber RDF plot between the Si and O atoms of the same NF within the reaxFF potential cut-off range for non-bonded interactions, i.e. 10 Å [136]. **Fig. 5.7**b shows the inter-fiber RDF plot between Si and O at the interface of two NFs. The latter can also be useful to observe the Si-O bonding at their interface knowing the equilibrium Si-O bond length is nearly 1.56 Å. For $d^{\parallel}$= 1.5 Å, more O atoms are available in the first coordination shell of Si (hence higher RDF value). However due to the surface topology of the nanofiber, the RDF value for $d^{\parallel}$= 3.5 Å is non-zero. Whereas no Si-O bond is formed for the $d^{\parallel}$= 6.5 Å, as the dangling bonds are farther apart.

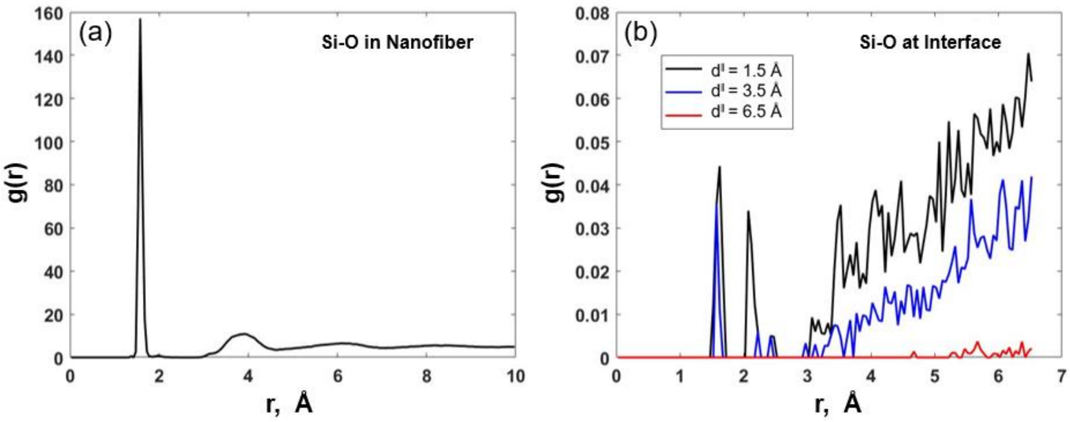

Fig. 5.7 *(a) RDF plot of Si-O bonding in the NF (Intra-fiber RDF), (b) RDF plot of Si-O bonding at the NF interface (Inter-fiber RDF)*

Silica nanofiber junction modelling

Two equilibrated amorphous NFs are placed at an average distance, $d^{\perp}$ ~0 Å from each other in the configuration as shown in **Fig. 5.8**. After energy minimization using conjugate gradient method, the system is further equilibrated for 200 ps to allow for the bond formation between the undercoordinated surface atoms at the junction of two nanofibers. Periodic boundary condition was used in all directions, while extending the simulation domain in X-direction.

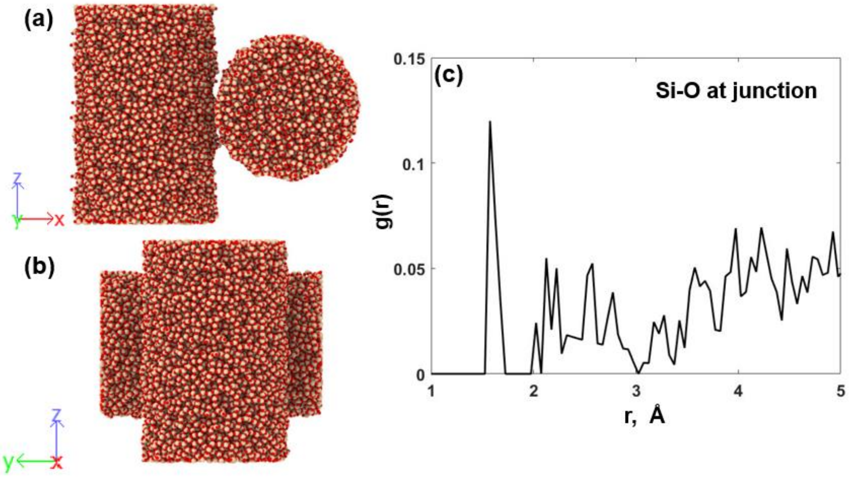

Fig. 5.8 *(a) Longitudinal, (b) side view of NF junction and (c) RDF of Si & O bonding at junction*

Simulation Procedure for NF Melting

The reactive force field uses a bond order/bond distance relation with a polarizable charge description and bond-order-dependent three- and four-body interactions. It also accounts for the van der Waals and Coulombic interactions between both bonded and non-bonded atoms, in order to accurately model the chemical reactions.

In order to simulate the melting process of silica nanofibers, a single-phase step-heating method is employed. Periodic boundary condition is maintained in all three directions while extending the simulation domain size in x and y-direction (lateral direction). Thus, an infinitely long isolated silica nanofiber is considered for the melting simulations. The box size in x and y direction is chosen such that the effect of the periodicity in these directions will not be observed. It is done by leaving the vacuum space greater than the potential cut-off (10 Å) in both directions.

In performing melting simulations, heating rate is an important parameter which can directly affect the accuracy of thermodynamic results. A higher value used for heating rate in an attempt to save the computational cost might lead to *missing or overshooting* the melting point of a material. To choose a *converged* value, a set of different heating rate values (1 K/ps, 0.2 K/ps, 0.1 K/ps) are tried for smaller diameter NW. The MD simulation was performed using NVT time integrator while raising the temperature from 300 K to 3300 K at a heating rate of 0.2 K/ps. It should be noted that even though the volume of the simulation domain is rendered fix by NVT ensemble, the NF volume can change in order to reduce the stresses generated during heating. The temperature of the system is maintained using Nosé-Hoover thermostat [153]. ReaxFF force-field is used to define the interactions between the silica atoms.

In Molecular dynamics, the forces in certain direction can result in advection velocity or aggregate velocity of the whole material system. Temperature of the system is given as kinetic energy divided by some number of degrees of freedom (and the Bolzmann constant). We know that the kinetic energy is a function of particle velocity (advection plus thermal velocity/vibrations). Therefore, the aggregate velocity has to be removed from the temperature calculation, as often thermal vibrations are wanted to compute the temperature. Typically *compute temp* includes the advection component of the velocity while calculating temperature. It is recommended to use *compute temp/com* instead, which removes the advection velocity component from temperature calculation.

Size effect on mechanical properties of silica

Uniaxial tensile test of bulk silica

Uniform tensile strain rates of magnitude lower than the sonic speed are applied to the bulk sample in the X-direction. The simulation box is extended in the loading direction at a specified loading rate while scaling the coordinates of all atoms in the loading direction. All tensile tests are performed at 300 K temperature using NPT ensemble at 1 atm pressure. Poisson's ratio effect is allowed in the Y- and Z- directions in order to obtain the zero-net force in these directions. **Fig. 5.9** shows the mechanical response of the material for the loading rates under consideration. As can be observed, the local voids are formed inside the bulk of the material due to bond breaking at the localized regions (**Fig. 5.9**a-b) when the failure stress is reached for both the strain rates. Later upon exceeding the critical crack length, these voids coalesce leading towards the brittle fracture of the bulk silica glass. Similar observations are made in the work performed by Chowdhury et al [124], Nakano et al [154], Simmons et al [155], Murlidharan et al [156], and Pedone et al [157].

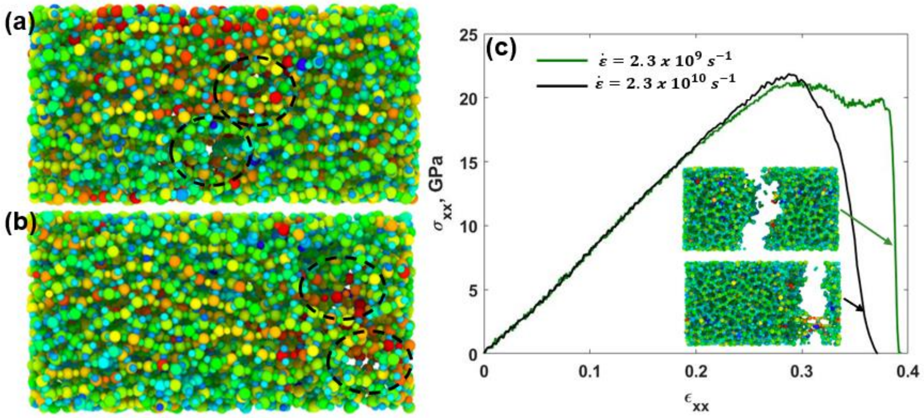

Fig. 5.9 *(a)-(b) Void formation at* $\dot{\varepsilon}$ *= 2.3 x* 10^{9}*, 2.3 x* 10^{10} *(Color plot shows stress per atom), (c) Comparison of stress-strain behavior. Note that the system was loaded along the x-direction.*

The Young's Modulus is evaluated from the linear region (strain state between 0-12%) of the stress-strain plots shown in **Fig. 5.9**c. The mechanical properties obtained from the tensile test simulations are enlisted in **Table 5.2**. It can be observed that strain rate has insignificant effect on the properties of amorphous bulk silica material. Note that the chosen strain rates are both extremely high. This is the known features of MD simulation. As such, the trends in the strain rate effects should not be considered to be valid for all strain rate ranges [124]. The MD snapshots suggest (see **Fig. 5.9**c) that fracture surfaces are essentially perpendicular to the loading direction, indicating that the material fails due to the maximum tensile stress.

***Table 5.2** Mechanical properties of amorphous bulk silica*

Strain rate (s^{-1})	Modulus (GPa)	Strength (GPa)	Strain at maximum stress, ε_{max} (%)
2.3×10^9	65.39	21.25	29.44
2.3×10^{10}	66.73	21.85	29.90

Uniaxial tensile test of silica nanofiber, D = 63.73 Å

To evaluate the elastic modulus of prepared silica nanowire, the uniaxial tensile deformation was applied at a constant strain rate of $\dot{\varepsilon} = 2.3 \times 10^9$ s^{-1} and $\dot{\varepsilon} = 2.3 \times 10^{10}$ s^{-1} by moving the top and bottom 5 Å layer (end-caps) of the nanofiber along the axial z-direction. It can be noted that due to the large vacuum region, the nanofiber can relax laterally and hence can undergo poison's ratio effect. During the loading, atmospheric pressure of 1 atm and room temperature are maintained by Nosé-Hoover barostat and thermostat as implemented in LAMMPS [28].

The coordination defect is present at the surface of the nanofiber due to under-coordinated Si and O atoms. Thus, as can be observed from **Fig. 5.10**a-b, the crack initiates at the surface of the nanofiber for strain rate $\dot{\varepsilon} = 2.3 \times 10^9$ s^{-1} and $\dot{\varepsilon} = 2.3 \times 10^{10}$ s^{-1}, respectively. Afterwards, the crack quickly propagates perpendicular to the loading direction leading to the brittle fracture of the material. Similar to the bulk silica case, the fracture surfaces are nearly perpendicular to the direction of loading, indicating that the nanofiber fails due to maximum tensile stress.

Fig. 5.10e shows stress-strain response of NF at two strain rates. Stress is calculated using stress/atom command in LAMMPS [158], which needs to be divided by the initial volume of the nanofiber in order to obtain the engineering stress developed during loading. The reported strain values are calculated based on the engineering strain definition by dividing change in length of the fiber by its original length. Due to non-linear elastic behavior, the stiffness calculation of silica is very sensitive to the strain state of the system. In particular, the slope of the stress-strain curve becomes steeper when the state of strain reaches to 5%. As such, the calculated value of modulus (i.e. secant modulus) goes up by 85 GPa when calculated based on strain rate 5% or higher. The similar behavior is observed by Yuan et al [159]. A parametric study performed by their group suggested that the accurate estimate of modulus can be obtained from “a third-order polynomial fit to the stress-strain curve in 0-12% strain range, or a linear curve-fit over a very small linear strain range of 0.5 %”.

Fig. 5.10f shows the O-Si-O bond angle (Tetrahedral bond angle) distribution (BAD) at different strain values for $\dot{\varepsilon}= 2.3 \times 10^9 s^{-1}$. Some distinct ‘signatures’ can be observed to characterize the atomic rearrangement as the sample is strained. It can be noticed that at unstrained/relaxed condition, the peaks appear at around 108.5º which is close to the equilibrium O-Si-O bond angle of 109.2º [136]. Upon further loading, the BAD peak shifts to the value of ~103.5º at strain state of 24.75%. Later upon the material fracture, the BAD peak goes back to its equilibrium angle. Based on above observations, it can be concluded that the NF structure is going under transformation in critical regions at high strain values, while the rest of the material recovers upon fracture, which is similar to as reported by Muralidharan et al for bulk amorphous silica [156].

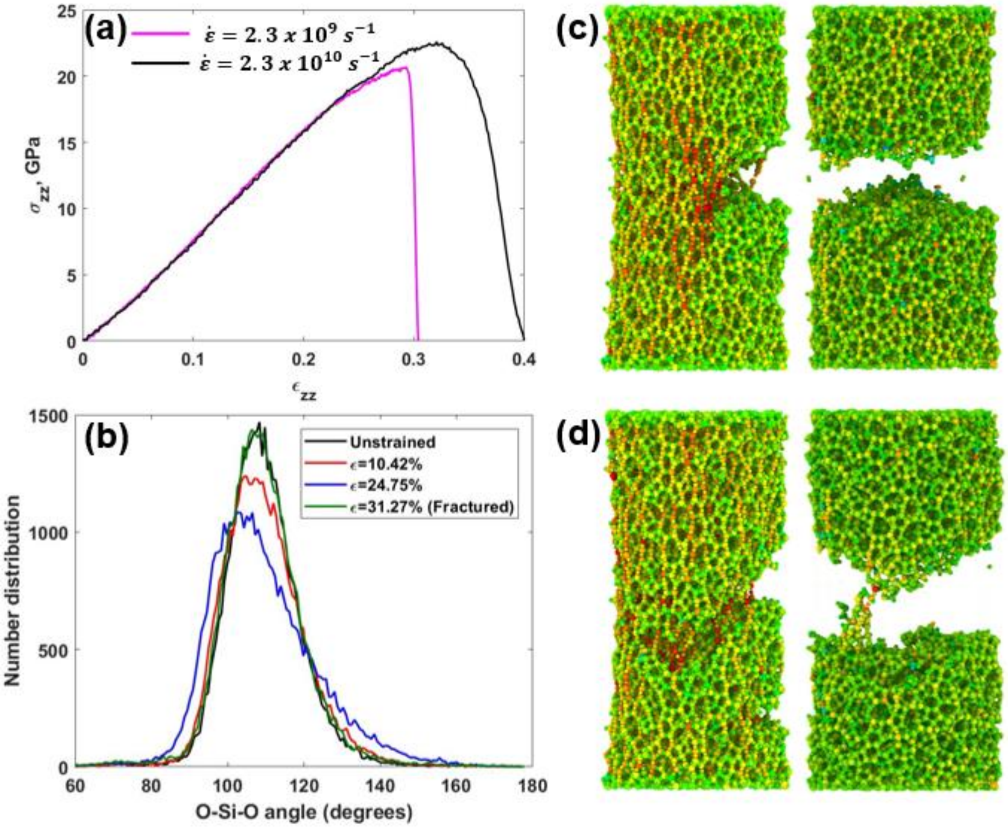

Fig. 5.10 *(a)Comparison of stress-strain behavior, (b) O-Si-O bond angle distribution (BAD) at* $\dot{\varepsilon}$*= 2.3 x* 10^{9}*, (c)-(d) Crack Initiating and fractured NF at* $\dot{\varepsilon}$*= 2.3 x* 10^{9}*, 2.3 x* 10^{10}

Table 5.3 lists and compares the mechanical properties of silica nanofiber at two different strain rates. The values obtained for Young’s modulus are in the range of 66-92 GPa as reported by Davila et al. [130] and Yuan et al [151], who used Garofalini and BKS potential, respectively. According to the available literature, the ultimate tensile strength of amorphous silica NFs increases with the increase of NF diameter. For example, using MD simulations, Zhang et al [129] reported the ultimate strength of NWs (D=2.23-10.23 nm) to be in the range of 8.3-12 GPa, whereas Brambilla and Payne [160] calculated the strength values for NW to be ranging from 15-26 GPa. It can be noticed that the strength values reported in our study are within the range reported in the literature. Moreover, as the "casting" method used to prepare our MD model is considered to generate lesser flaws at the surface of the NF [159], the higher strength values can be expected.

Table 5.3 *Mechanical properties of amorphous silica nanofiber*

Strain rate (s^{-1})	Modulus (GPa)	σ^{ult} (GPa)	ε_{max} (%)
2.3×10^9	62.95	20.70	29.31
2.3×10^{10}	58.49	22.58	32.05

Fig. 5.11a shows and compares the stress-strain behavior of bulk silica and silica NF of different sizes. It can be noticed that for all the NFs, the crack initiates at the surface of the NF and eventually propagates through their cross-section leading to the failure. As the NF structure is more *discrete* in the case of D=1.75 nm, the stress drops upon failure of a ring structure while the rest of the cross-section carries the load as shown in NF geometry ***Fig. 5.11***a. Thereafter, the stretching of remaining rings still carries load which is less than the ultimate stress in the material. Upon further extension, the NF fails in a brittle manner. The properties obtained from the tensile simulation and NF density are shown in ***Fig. 5.11***(b)-(c). It can be noted that the strain at maximum stress and strain to break decreases as the NF diameter decreases. It indicates that there is no brittle-to-ductile behavior shown by the studied NFs, which is more recently discussed in other

studies [26][27]. Elastic modulus of NF tends to decrease as the NF size increases. As such, no trend in NF strength is observed as reported in other literatures [27][128].

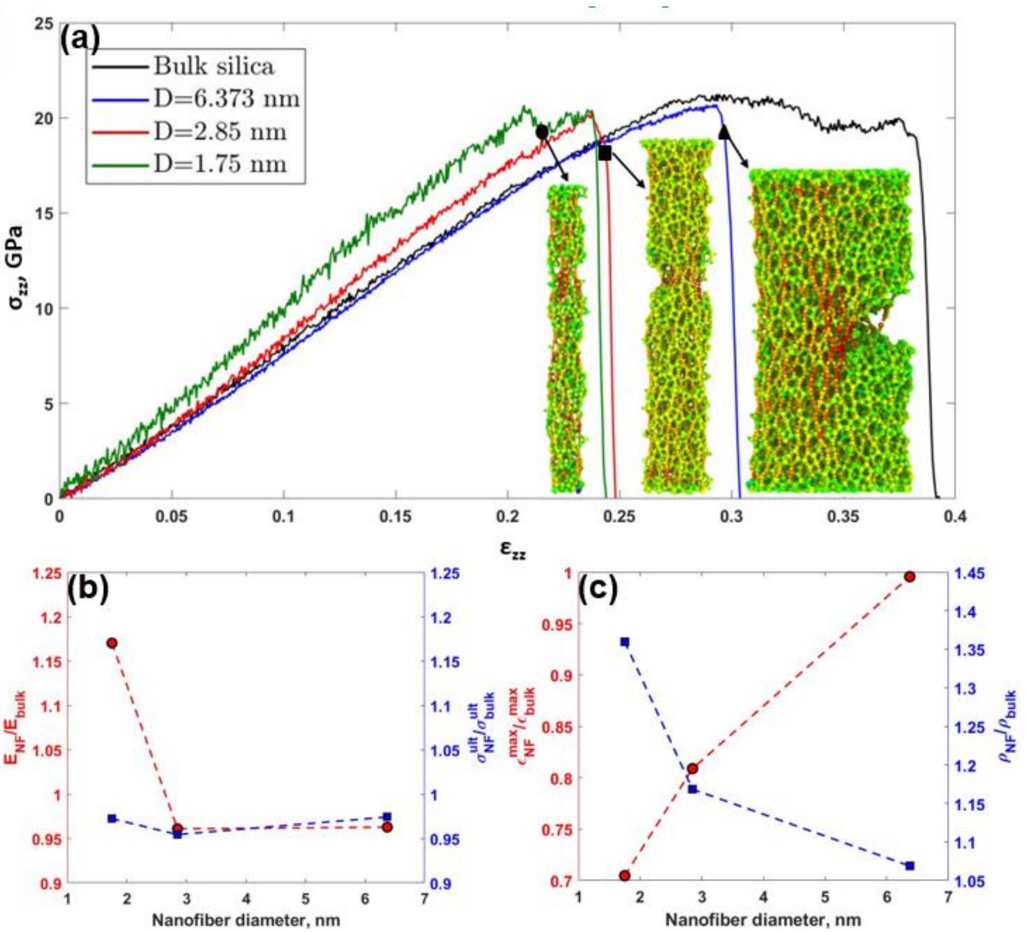

Fig. 5.11 *(a) Stress-strain behavior of bulk silica and NFs of different sizes, (b)-(c) Variation of silica NF properties with diameter*

Effect of Hydroxylation on mechanical properties of silica NW

Similar loading conditions as described for the pristine nanofiber were applied to the equilibrated structure of hydroxylated silica nanofiber models shown in **Fig.5.4**. **Fig. 5.12** shows the stress-strain plot for pristine and hydroxylated NF at both the strain rates. It can be noticed that the crack initiates from the surface of NF as observed in pristine NF tensile test (**Fig. 5.12**). For both the strain rates, the strength of the hydroxylated NF is decreased. It could be explained from the perspective of breaking of ring structures at the fiber surface during silanol formation. More details on it can be found in the study by Yeon et al. [150].

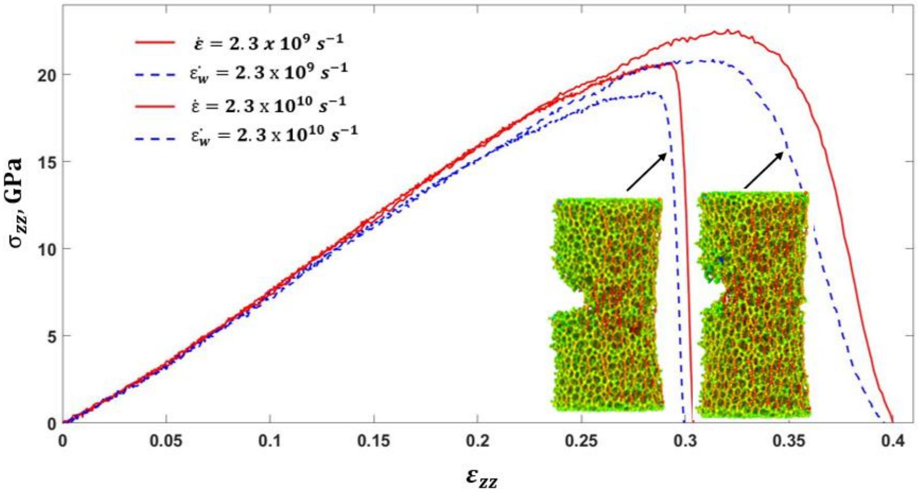

Fig. 5.12 *Comparison of (a)stress-strain behavior, and (b)properties of Pristine and Hydroxylated NW*

Effect of nanofiber interface on overall mechanical properties

Aligned silica NF arrangement

Similar loading conditions as described for the isolated nanofiber are applied to the equilibrated geometries for aligned silica nanofiber models shown in **Fig. 5.6**. The uniaxial tensile deformation was applied by moving the top and bottom 5 Å layer of both the nanofibers along the axial z-direction following the loading conditions described in the previous section. **Fig. 5.13** compares the effect of nanofiber interface for three cases at lower strain rate. For $d^{\parallel}$ = 1.5 Å, the crack initiates from the surface of one nanofiber, as observed in the case of an isolated nanofiber. As the crack continues to propagate normal to the loading direction in this fiber, cracks start to initiate from two different locations at the surface of the 2nd fiber. The final fracture occurs due to the interaction of the crack at the interface of two NFs. Due to the covalent Si-O bonding at the interface of the two NFs, the crack is ‘extended’ to another NF. Both NFs fail in a brittle manner. In the stress-strain plot, the response of the fiber mat (a.k.a the fiber pair) is compared with bulk silica and isolated nanofiber. It can be observed that the overall stress-strain in the mat is very distinct. In particular, the mat appears to exhibit something like a “progressive failure” process. The first failure in the mat is noticed at around 26.32% strain. Beyond this strain state, the stress in the mat reduces from ~21 GPa to ~10.5 GPa. The stress state remains constant, on average, until the strain state equals to 28.4%. Beyond this strain state, the overall stress in the mat reduces to zero. To gain further understanding on the deformation process in the mat, the snapshot of loaded NF mat is also shown in **Fig. 5.13**. It is evident that the at strain state = 26.32%, fiber 1 completely ruptures but the fiber 2 continued to deform without complete failure. The fiber 2, however, completely fails at a strain state = ~28.5%. In theory, both fibers in the mat should have failed at the same states of strain. Nevertheless, this is why the stress state in the mat reduces to half at strain state = 26.32%. The reason why fiber 1 and 2, exhibited slightly different failure strain can be explained from the viewpoint of amorphous structure of the NF. Due to the “extreme random” nature of an amorphous structure, the NF failure have shown a stochastic nature. Based on our simulations, it can be said that NF failure can happen at strain values ranging from nearly 25% to 38% (**Fig. 5.13**).

When the separation distance between the nanofibers is higher, the fracture process is different. The stochastic behavior of ε_{max} is still observed for these cases. It can be observed that when $d^{\parallel} = 3.5$ Å, the separation distance is larger for forming any spontaneous covalent bonding but sufficient to have some level of Si-O bonding. When $d^{\parallel} = 6.5$ Å, the separation distance is so large that fiber-fiber interaction becomes very insignificant. As such, when tensile loading is applied to these two types of nanofiber pairs, the initial cracks are independently formed, grow and propagate. The unique "progressive failure" is observed in both cases when strain rate $\dot{\varepsilon} = 2.3 \times 10^9\ \mathrm{s}^{-1}$. It can be noted that when one of the fibers fails earlier in this range, the stress state in the mat reduced to half as shown in **Fig. 5.14**.

The "progressive failure" mode observed due to stochastic ε_{max} values of NF is completely absent when at $\dot{\varepsilon}$= 2.3 x 10^{10} s^{-1} as shown in **Fig. 5.15**. We believe the at higher strain rate, the loading rate is faster than the crack propagation rate. As such, there is little time gap between fiber 1 and 2 failures. **Fig. 5.16** compares the mechanical properties obtained from the tensile test simulations. It can be observed that for both the strain rates, the values are close to that of the isolated NF.

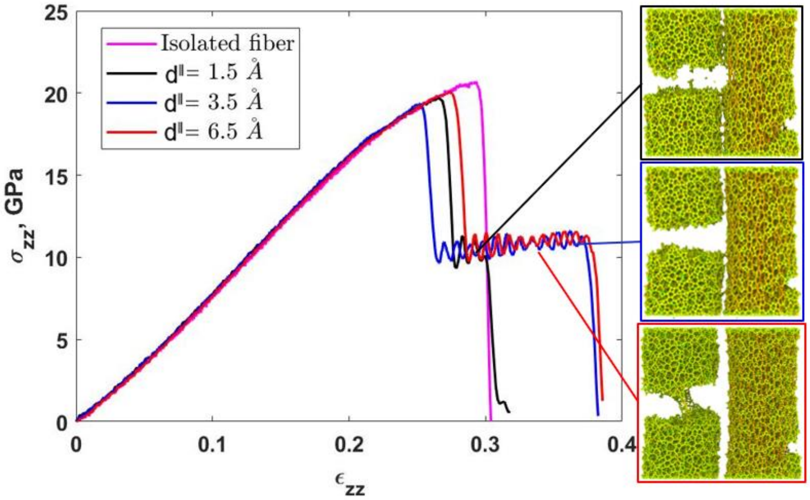

Fig. 5.13 *Effect of Nanofiber interfaces on mechanical behavior of 2-fiber mat at* $\dot{\varepsilon}$= 2.3 x 10^9 s^{-1}

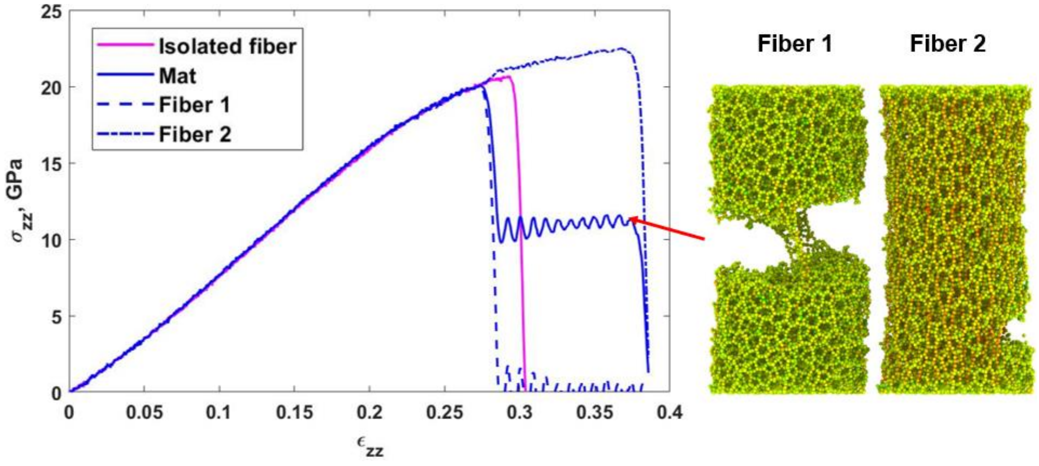

***Fig. 5.14** Stress-strain behavior and atomic configuration of NF mat at $\dot{\varepsilon}$= 2.3 x 10^9 s^{-1} for $d^{\parallel}$ = 6.5 Å*

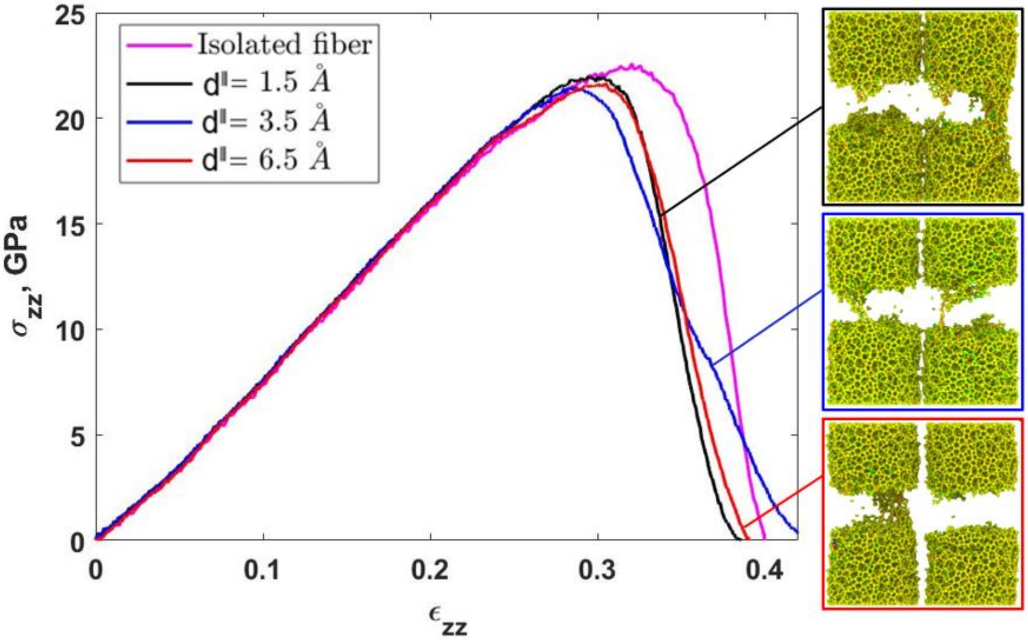

***Fig. 5.15** Effect of Nanofiber interfaces on mechanical behavior of 2-fiber mat at $\dot{\varepsilon}$= 2.3 x 10^{10} s^{-1}*

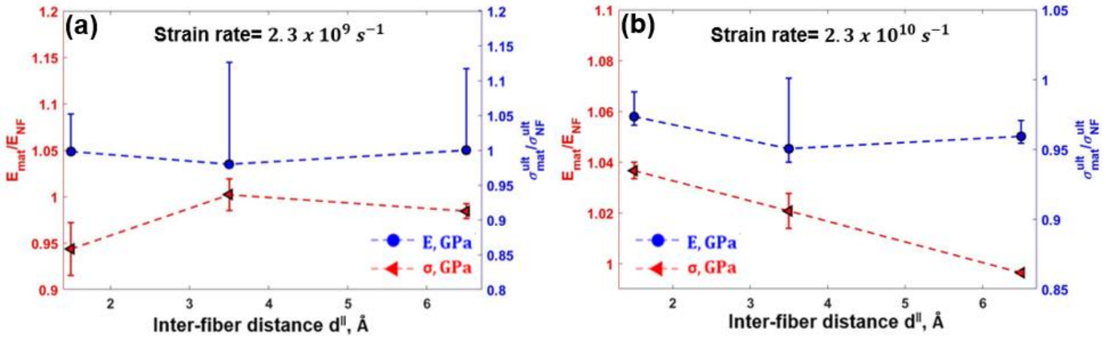

Fig. 5.16 *Effect of inter-fiber distance on mechanical properties at (a)$\dot{\varepsilon}$= 2.3 x 10^{9} s^{-1}, (b)$\dot{\varepsilon}$= 2.3 x 10^{10} s^{-1}*

Silica NF junction

The uniaxial tensile deformation was applied only to the NF oriented in z-direction, while keeping the ends of the undeformed NF (oriented along y-axis) fixed. The loading conditions defined earlier are used to stretch the fiber along z-axis, while the bending stresses generated in the undeformed fiber are calculated to quantify the effect of load transfer from the nanofiber junction. **Fig. 5.17** shows and compares the axial stress (σ_{zz}) developed on the deformed NF for two different strain rates with the isolated NF. It can be observed that the stress-strain response is similar to that of the isolated NF. The response after maximum stress is deviated from that of isolated NF due to the junction interactions. **Fig. 5.17** shows the fractured NF for $\dot{\varepsilon} = 2.3 \times 10^{9}\ s^{-1}$and $2.3 \times 10^{10}\ s^{-1}$. respectively. **Table 5.4** lists the mechanical properties of the silica nanofiber at applied strain rates. It can be noticed that the values are comparable to that of isolated NF at both the strain rates.

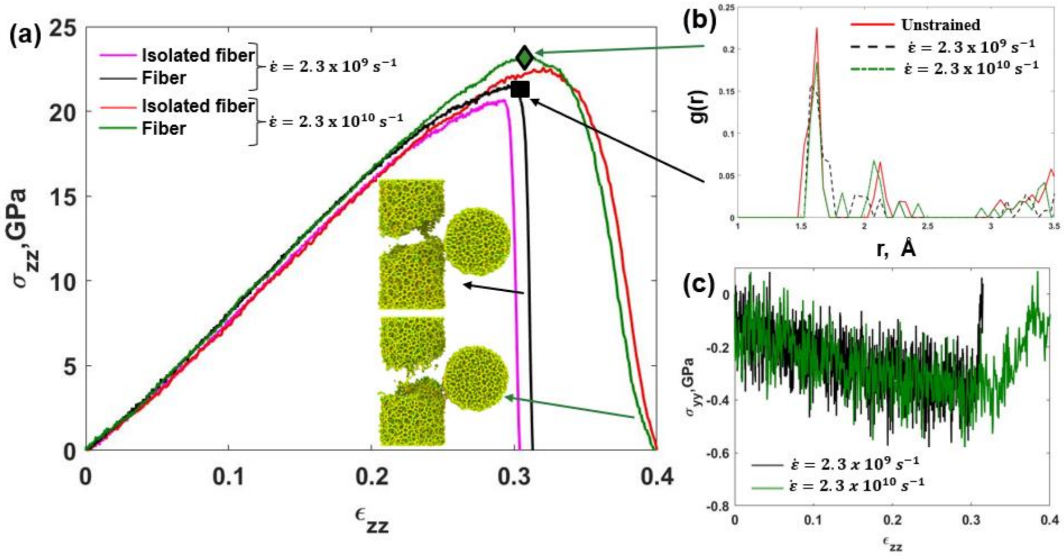

Fig. 5.17*(a) Tensile stress in deformed NF, (b) RDF plot of Si-O at junction at ε_{max} marked on plot (a), (c) Bending stresses generated in still/undeformed NF in junction model*

Fig. 5.17c shows the bending stresses developed in still/undeformed NF at a given loading rate. It can be observed that as junction is staying intact during the tensile loading on the deformed NF (**Fig. 5.17**b), the bending stresses are developed the entire time until the deformed NF breaks. This suggests that the junction between two NFs can be modelled at macroscale as a joint that allows the forces applied by one NF to cause bending in the other NF, i.e. “rotating joint” or “welded joint”[133].

Table 5.4 *Mechanical properties of deformed silica nanofiber in junction model*

Strain rate (s^{-1})	Modulus (GPa)	Strength (GPa)	Strain at maximum stress (%)
2.3 x 10^9	64.34	21.67	30.12
2.3 x 10^{10}	59.12	23.26	30.88

Effect of nanofiber arrangement on interfacial strength

Due to the bond formation between under-coordinated Si and O atoms among the two NFs, it can be of interest to observe the load transfer between them during the loading of the nanofiber mat. In order to characterize the NF interface, pullout simulations can be performed for different NF mat configurations shown in **Fig. 5.6**. The similar approach is popular to evaluate the interfacial shear strength of carbon nanotubes reinforced polymer composites [14]–[16], [48], [81].

To pullout silica nanofiber, nearly 5 Å of the fiber is fixed and a constant pullout velocity of 23 m/s is applied to one of the silica nanofibers in the system, while keeping the ends of other nanofiber fixed. The opposite end of the pulled nanofiber is made rigid, as shown in **Fig. 5.18**a. This is implemented by using *fix rigid* command in LAMMPS, that uses NVE (microcanonical) time integration technique based on Richardson iterations [161] to update the position and velocity of each atom in a rigid body. The total force and the torque on the rigid portion are then computed as the sum of forces and torques on its constituent particles for each time step and are then updated so that the body moves and rotates as a single entity.

The change in potential energy (ΔPE) during the pullout is calculated by subtracting the initial energy before the pullout from the energy at a given pullout displacement. **Fig. 5.18**b shows the ΔPE vs pullout displacement trend for three studied cases. It can be observed that for average $d^{\parallel}$= 6.5 Å, there is no increase in the total potential energy due to lack of bonded interactions (van-der Waals and electrostatic only) between the two NFs (**Fig. 5.7**b). However as observed from **Fig. 5.7**b as well, more bonds between under-coordinated Si and O atoms are formed in the case of $d^{\parallel}$= 3.5 Å. This leads to the increase in total potential energy when the nanofiber is pulled from the system. This is resulted from an increase in the interactions between the two nanofibers as the relative motion happens between them. Similarly, the increase in potential energy is more significant when $d^{\parallel}$= 1.5 Å as increased number of bonds are created at the NF interface (as concluded from **Fig. 5.7**b). Hence even more interactions/resistance is offered by the still nanofiber as the other fiber is pulled out. Due to the resistance (Si-O bond formation and breaking) offered by the undeformed fiber, the pulled-out NF length increases when $d^{\parallel}$= 3.5 Å and $d^{\parallel}$= 1.5 Å. The typical bond breaking and formation during the pullout procedure leads to the fluctuations in the potential energy plot. This is also known as stick-slip mechanism, which has also been observed by Namilae et al [81] during carbon nanotube pullout simulation from the polymer matrix. In the present study, this represents the effective load transfer between the two nanofibers due to the covalent bond formation between their undercoordinated atoms.

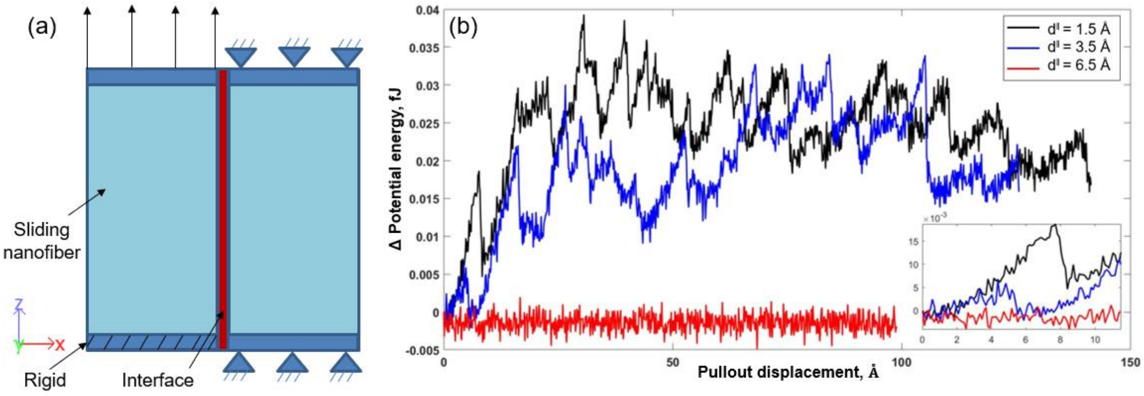

Fig. 5.18 *(a) Schematic of silica nanofiber pullout simulation, (b) Potential energy variation during pullout of silica nanofiber in aligned fiber arrangement. Inset plot shows the zoomed in view of energy needed to break initial interfacial bonding*

In the current study, the initial portion (**Fig. 5.18**b Inset) of the potential energy variation plot may represent the strength of initial interface formed between the NF pair. The corresponding values of pullout displacement and change in potential energy (ΔPE) are reported in

Table 5.5. It is reported that the Si-O bond strength is nearly 1.6022×10^{-4} fJ (621.7 kJ/mol) [162]. It can be observed that the values listed in **Table 5.5** are significantly higher than the reported Si-O bond strength. It is due to multiple Si-O bond formation and breaking at the interface of two NFs. Also, the deformation of two NFs can also be a contributing factor towards the increase in ΔPE values as the NF is being pulled out. Further, as no Si-O bond switching is occurring when $d^{\parallel}$= 6.5 Å, no ΔPE change is observed. It can be evident that for $d^{\parallel}$= 1.5 Å, the higher value of ΔPE may be contributing towards more 'coherent' failure of two NFs during the tensile tests.

***Table 5.5** Comparison of ΔPE for different NF interspace distance*

$d^{\parallel}$, Å	**Pullout displacement, Å**	**ΔPE, $\times 10^{-4}$ fJ**
1.5	7.7	186.608
3.5	4.37	64.926
6.5	-	0

It should be noted that since the values plotted in **Fig. 5.18**b are dependent on the number of bonds formed at the NFs interface, generating NF using "cutting" method can lead to more increase in the potential energy due to more coordination defects present on their surface [129]. Thus, the 'quality' of the interface depends on the NF surface morphology, inter-fiber distance and the number of under-coordinated atoms on the nanofibers surface.

Size-dependent Thermal Stability of Silica Nanofibers

Fig. 5.19(a) shows the potential energy plots at three different heating rates. As informed from it, 0.2 K/ps can be used for the following simulations. Upon heating, the potential energy varies linearly with the temperature until point A on the curve, which corresponds to the start of melting. Upon further heating, the potential energy curve becomes non-linear. It can be noticed that there does not exist a sharp/unique melting temperature for amorphous materials as noticed by other researchers for different amorphous materials [137]. To identify the change in slope of potential energy vs temperature plot, we can look at the secant modulus values in **Fig. 5.19**(b). Secant modulus at a point on the curve is calculated (for non-linear materials) by finding the slope of a line joining that point to the start point, i.e. T=300 K. The atoms at the NW surface are at high energy and thus the melting of NW starts from the surface leading to melting of NW interior. Eventually, the NW takes the form of a spherical bead under vacuum conditions **Fig. 5.19**(d).

The inexistence of an instantaneous melting point (progressive melting) can also be explained from the viewpoint of surface energy. For solid to liquid phase translation, an external energy (by heating) is required that is equal to the latent heat of fusion for that material. The melting of solid occurs at energy level of the values equal to the solid-state internal energy plus the latent heat of fusion. Due to surface tension, the atoms at the surface always remain at higher energy states, which leads to the melting of nanomaterial at lower temperature T_i ($T_i < T_m$) compared to their bulk (T_m) counterparts. Due to the varied energy levels between the NW interior and surface, the melting happens over a range in a progressive manner (hence not instantaneous).

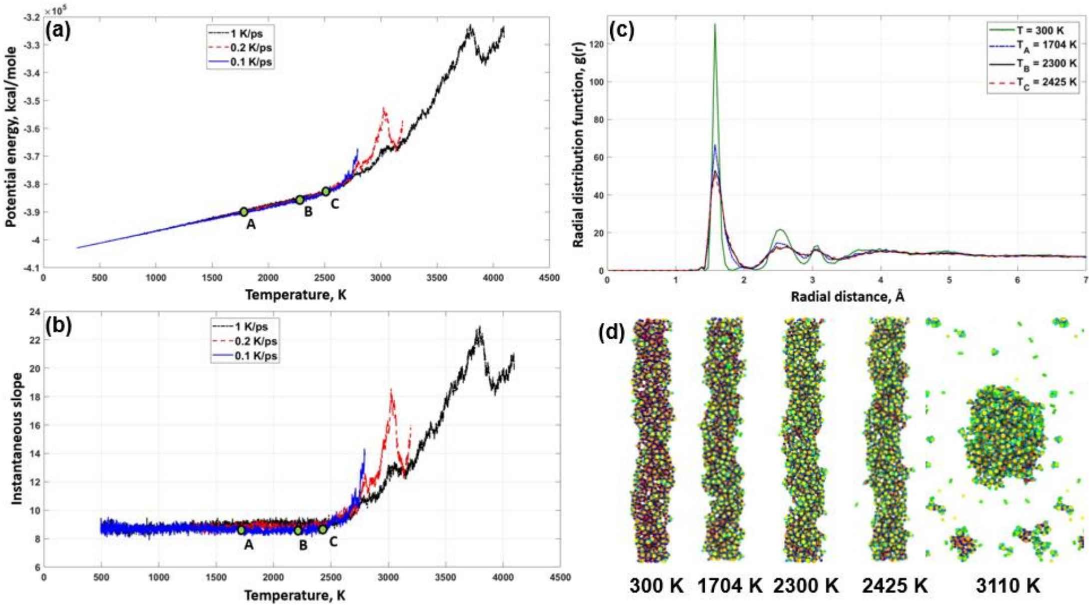

***Fig. 5.19** (a) Variation in Potential energy during heating, (b) Variation in Instantaneous slope during heating, (c) RDF plot at marked temperatures, (d) NW configuration at marked temperatures (color plot shows potential energy/atom)*

Further, it can be of interest to look at the radial distribution function (RDF) plot at different temperatures values as shown in **Fig. 5.19**(c). It can be noticed that the secondary peaks in the RDF plot flattens as the melting of NW starts at T_A=1704 K, which confirms the solid to liquid transition (melting) of a material. In addition to focusing on secondary peaks, the broadening of primary peak can be related to the melting behavior. As suggested by the literature on melting point of ceramic materials, a 10% increase in the bond length and standard deviation of RDF plot might be considered as the melting temperature of the material. At point A in **Fig. 5.19**(c), the standard deviation in RDF plot is more calculated to be increased by 120%, while point B and C shows an increase by 134% compared to the T=300 K. No change in the value of *r* at the RDF peak is observed as it stays focused at 1.575 Å. Similarly, for NF diameter ~3 nm (**Fig.5.20**c), point A and B (and C) corresponds to increase in standard deviation of RDF by 15% and 22%, respectively. As no apparent change in the RDF plots is observed after point B, we may consider point A and B as the initiation and completion of melting of NW.

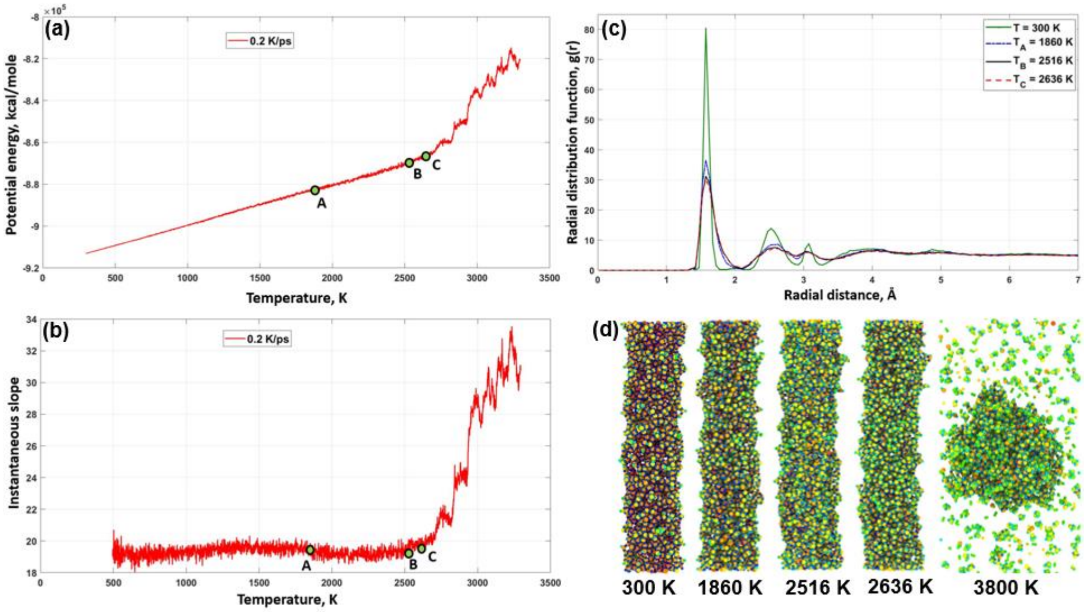

Fig.5.20 *(a) Variation in Potential energy during heating, (b) Variation in Instantaneous slope during heating, (c) RDF plot at marked temperatures, (d) NW configuration at marked temperatures (color plot shows potential energy/atom)*

Conclusion

We investigated the effects of interspace distance and junction formation between silica NFs on their mechanical properties at at strain rates of $2.3 \times 10^{9}\ \mathrm{s}^{-1}$and $2.3 \times 10^{10}\ \mathrm{s}^{-1}$. It is observed that as the elastic modulus depends on the bulk material property, the modulus of NFs does not vary significantly for each studied configuration. Typically, the NF failure is independent of each other when d$^{\parallel}$= 3.5 Å, 6.5 Å. However at strain rate of $2.3 \times 10^{9}\ \mathrm{s}^{-1}$, the crack propagation in two NFs is more coherent for d$^{\parallel}$= 1.5 Å. It is believed to be due to the significant Si-O bonding at the interface when $d^{\parallel}$ decreases. More insight into the interface is gained from the NF pullout simulation. It is noted that more potential energy is needed to break the interface of the NFs for $d^{\parallel}$= 1.5 Å, while the value decreases for $d^{\parallel}$= 3.5 Å, and stays zero in the case of no covalent bonding at the nanofiber interface ($d^{\parallel}$= 6.5 Å). The results from pullout simulation also support the coherent fracture of two NFs when the interspace distance is reduced.

From NF junction model, it can be concluded that load is transferred from the junction of the two NFs due to an intact junction formation between the two fibers. For both the strain rates, the NF junction stays intact during the tensile loading and the deformed NF fails near the junction.

Since different modelling techniques (“cutting”, “casting”) can result in different surface topology of the nanofiber, the values of potential energy to pullout the NF can vary. Additionally, the pacification/hydroxylation of the undercoordinated Si and O atoms at the NF surface can change this value, which are planned to be published as our future research findings.

In this chapter, we also performed ReaxFF MD simulations to study size-dependent melting behavior of amorphous silica (a-SiO_2) NW. The start of melting process in a-SiO_2 NW of diameters nearly 1.75 nm and 2.85 nm was observed at 1704 K and 1860 K, respectively. Melting initiates from the surface of the NW, and as temperature increases, the entire NW structure melts eventually forming a spherical bead. It was found that the size-dependent melting of a-SiO_2 NW occurs in a progressive manner over a range of temperature. Melting Point Depression (MPD) phenomenon is observed as the size of the NW decreases. Instantaneous slopes are used to evaluate the point of start of melting for the NW structure. Also, the standard deviation values from the Radial distribution function (RDF) plot at start of melting were calculated to be increased by 120% and 15% for NW D=1.75 nm and 2.85 nm, respectively.

CHAPTER 6 CONCLUSIONS & FUTURE WORK

Conclusions

This computational study performed in Chapter 3 indicates that there is an effective stress transfer from the epoxy resin to the nanotube. The interfacial bonding was predicted using molecular dynamics simulations based on a cured epoxy resin model, which was constructed by incorporating the three-dimensional cross-links formed with curing agent molecules. Reactive force-field (ReaxFF) is used to consider the bond formation and dissociation during CNT pullout from crosslinked epoxy matrix. The pullout simulations of a SWNT from the epoxy resin showed that the interfacial shear stress was approximately 50 MPa.

The results of the two-dimensional model discussed in Chapter 4 indicate that MATLAB generated random fiber model can be used computationally in Finite Element Analysis as an excellent tool for predicting elastic constants of CNT reinforced polymer matrix. It can be noted that this model can be applicable for any random fiber composite. The second part of Chapter 4 focused on developing a three-dimensional computational method that incorporates stochastic distributions of the CNT waviness and orientation in building finite element predictive models. Mechanical properties of random wavy carbon nanotube composites are then evaluated using Abaqus. It is found that due to CNT waviness, the inefficient load transfer between CNT fiber and matrix results in the overall decrease in their mechanical properties by 4-8%. The ‘three-phase’ model suggests that the composite modulus is further compromised by 2.5% as the interphase modulus reduces by up to 90% for 0.1% CNT v_f due to the presence of voids at CNT/epoxy interface (‘soft’ interphase).

In Chapter 5, the size-dependent mechanical properties of NF (d = 1.75 nm, 2.85 nm, 6.37 nm) are studied. It is found that the NF keep showing brittle behavior as its size go down. The strain to failure is found to have decreased as NF size decreases. Further, effect of hydroxylation (silanol formation) on NF mechanical properties is studied. It is concluded that the mechanical properties of hydroxylated NF degrade due to breaking of 'ring structure' during silanol formation. Also, the effects of interspace distance and junction formation between silica NFs is studied. As the elastic modulus depends on the bulk material property, the modulus of NFs does not vary significantly for each studied configuration. Typically, the NF failure is independent of each other when $d^{\parallel}$= 3.5 Å, 6.5 Å. However, at strain rate of $2.3 \times 10^{9}\ \mathrm{s}^{-1}$, the crack propagation in two NFs is more coherent for $d^{\parallel}$= 1.5 Å. More insight into the interface is gained from the NF pullout simulation, which confirms a relatively stronger interface for $d^{\parallel}$= 1.5 Å. From NF junction model, it can be concluded that load is transferred from the junction of the two NFs due to an intact junction formation between the two fibers. The stochastic nature of ε_{max} values for amorphous silica NF is observed with ε_{max} ranging from 25%-37%.

Later, the NF melting study is performed to evaluate the size-dependent thermal stability of a- SiO_2 NW. NW melting starts at the surface of the NW as the temperature is raised. 0.2 K/ps is found to be an optimum value of heating rate for amorphous silica NW using ReaxFF force-field parameters. The start of melting process in a-SiO_2 NW of diameters nearly 1.75 nm and 2.85 nm was observed at 1704 K and 1860 K, respectively. Melting Point Depression (MPD) phenomenon is observed as the size of the NW decreases.

Future Work

CNT Agglomeration

The effect of CNT agglomeration on the elastic properties of CNT-based nanocomposites can be studied using developed Python algorithm. The dmin parameter described in the flowchart shown in **Fig. 4.1** can be varied between the well-dispersed and agglomerated region of the RVE. Three such models as shown in **Fig. 6.1Error! Reference source not found.** can be considered. Different values of waviness angles are used for agglomerated (θ_{agg}) and well-dispersed region (θ_{unagg}) for RVEs shown in **Fig. 6.1Error! Reference source not found.**(a), (b). **Fig. 6.1Error! Reference source not found.**(a) represents RVE with CNT agglomerate present at the RVE center, while **Fig. 6.1Error! Reference source not found.**(b), (c) shows the CNT agglomerate at the edge of the RVE. Both waviness angle allowable inter-fiber distance are used to represent CNT agglomerate.

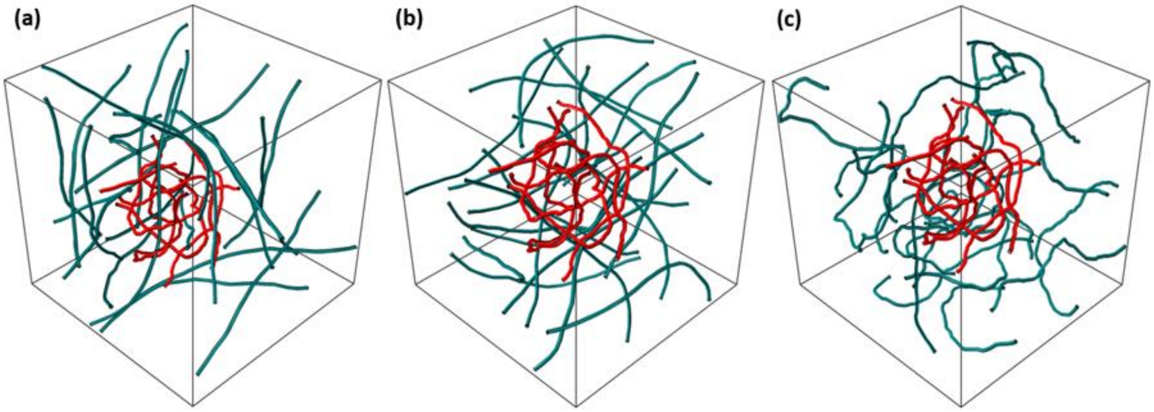

Fig. 6.1 *CNT Models with 0.27% vf with (a)Agglomerate at center of the RVE (θ_{unagg}=10°, θ_{agg}=30°), (b)Agglomerate at RVE edge (θ_{unagg}=10°, θ_{agg}=30°), (c)Agglomerate at RVE edge (θ_{unagg}=30°, θ_{agg}=30°)*

Interface-Driven Failure Properties of CNT/Epoxy Nanocomposites: Spring layer method

An “interface” is a two-dimensional border that separates distinct phases, such as fiber, matrix, interphase, fiber coatings, etc. Whereas “interphase” can be denoted as a region in which the fiber and matrix phases are mechanical or chemically combined, and are otherwise indistinct.

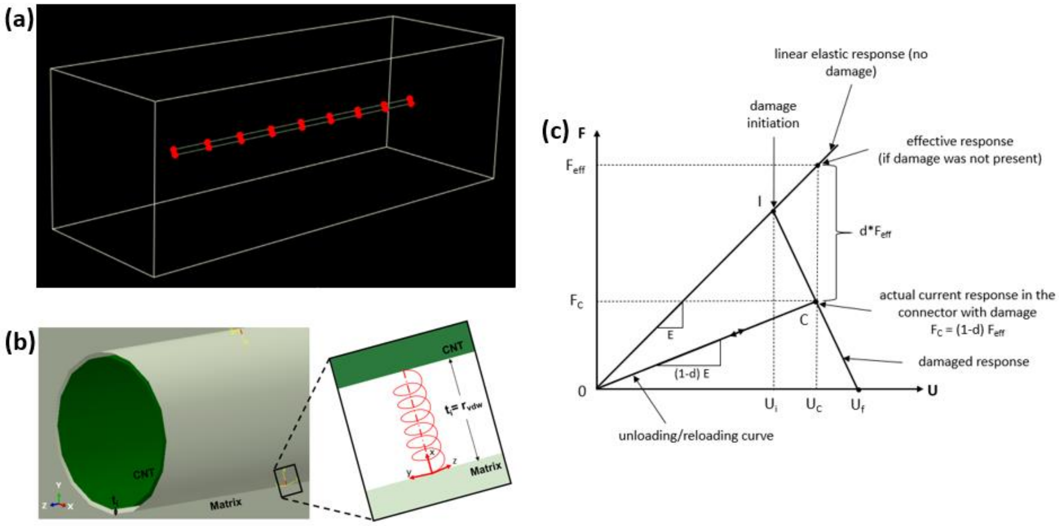

Fig. 6.2 *(a)Spring layer to represent CNT/matrix interface (b)description of spring at interface, (c) Failure criterion*

A CNT/epoxy composite is only as strong as its interface. In the previous chapters, we have considered the CNT/epoxy interface as an ideal interface. It implies that the load transfer from polymer matrix to the CNT fibers is 100%, which is hardly the case observed during experimentations. To represent the discontinuous displacements between CNT and matrix, we used the *interphase layer* method to represent CNT/epoxy interphase. This model is only good enough to evaluate the effect of interphase properties on the effective elastic properties of the composite. Therefore, in order to proceed towards evaluating the failure properties, we discussed *spring layer interphase* method in this chapter. The *spring layer* method consists of replacing the interphase region by an interface (border separating fiber and matrix) of negligible thickness possessing the required strength (**Fig. 6.2**). It can be noted that for a certain value of spring stiffness, the present interface model would coincide with the case of perfect bonding between the CNT and epoxy. In this case, the tractions and displacements will be continuous across the interface.

Multiscale Modelling of Stand-alone Silica NF Mat

The developed Python algorithm as shown in **Fig. 4.1** can be used to construct a three-dimensional stochastic model for stand-alone electrospun silica NF network/mat. **Fig. 6.3** shows one such three-dimensional fiber network.

Apart from the possible mechanical entanglement of NFs, it becomes important to account for inter-fiber interactions in a stand-alone network for the purpose of inter-fiber load transfer. The cross-links are formed between the fibers based on a minimum cut-off distance. Given *N* is the number of fibers in the system, there are *N(N-1)/2* possibilities of cross-links between the fibers. For instance in **Fig. 6.3**, based on a minimum cut-off distance of nearly 290 units, 7 cross-links have been generated. In our case, these interactions can be defined as frictional interactions or elastic springs (**Fig. 6.3**). In Abaqus, CONN3D2 connector element can be used to represent the frictional or spring connection between the two fibers. These elements have two nodes. The position and motion of the second node on the connector element are measured relative to the first node. In such manner, local constitutive response in a network can be captured.

Each spring can be assigned stiffness in translational (3 dof) and rotational (3 dof) direction (K_T and K_θ) to allow for energy penalties during relative translational motion between the inter-connected fibers. Furthermore, displacement or force-based failure criterion as shown in **Fig. 6.2**(c) can be incorporated to allow for the failure of inter-fiber interactions, which can allow for the overall network failure.

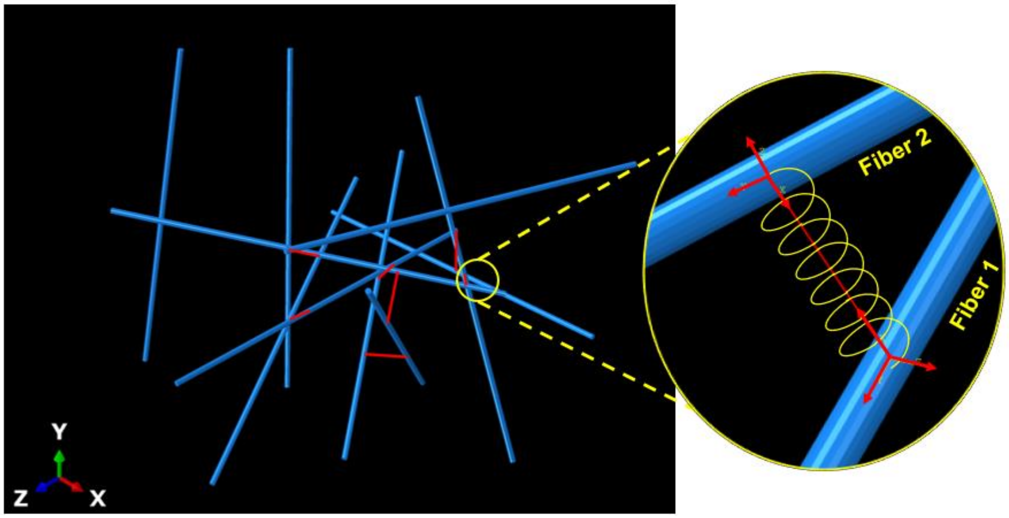

Fig. 6.3 *Three-dimensional stochastic network with inter-fiber interactions defined using elastic springs*

APPENDIX A

SAMPLE SCRIPTS

A1. 2D Random Fiber Network generation using MATLAB [30]

```
%% Rajni Chahal (rajni.chahal@mavs.uta.edu), PhD Student, UT Arlington
% Dr Ashfaq Adnan, Professor, UT Arlington
%% July 20, 2016
% Please contact for any help in code
n=100; % number of fibers
L=400; % x-dimension of RVE
M=300; % y-dimension of RVE
l=L/10; % length of fiber
r1=0.5; %radius of CNTs/fibers
d1=2*r1;
axis([0 L 0 M]);
ax=gca;
th=[];
XX=[]; YY=[];
for i=1:n
    x=rand*L;
    y=rand*M;
```

```
    t=rand*2*pi;

    th=[th;t];

    X=[x-(l/2)*cos(t) x+(l/2)*cos(t)];

    Y=[y-(l/2)*sin(t) y+(l/2)*sin(t)];

    figure(1);

    line(X,Y,'Color',[0 0 0],'LineWidth',d1); % to generate thin fibers, put 1 in place of d1

    axis off

    set(gca,'units','pixels','position',[50 50 L M]);

end
```

A2. Sample LAMMPS script for NF tensile simulation in CHAPTER 5

```
# ------------------------ INITIALIZATION ----------------------------

units           real

dimension       3

boundary        p p s

atom_style      charge


neighbor     2.0 nsq
```

```
neigh_modify   every 10 delay 0 check no


# ----------------------- ATOM DEFINITION ----------------------------

read_data         geometryfile.txt


# ------------------------ FORCE FIELDS ------------------------------

pair_style     reax/c NULL           # reaxc.control

pair_coeff     * * ffield.reax.alphaquartz Si O


# ------------------------- SETTINGS ---------------------------------

compute       peratom all pe/atom

compute       myPress all stress/atom NULL

compute       13 all reduce sum c_myPress[3]


# ------------------------- GRIPS TO APPLY LOADING --------------------------------

region        bottom block INF INF INF INF INF 3.53

region        top block INF INF INF INF 91.8 INF

group         bottom region bottom

group         top region top
```

```
fix         freeze1 bottom setforce 0.0 0.0 0.0

fix         freeze2 top setforce 0.0 0.0 0.0

velocity      bottom set 0.0 0.0 0.0

velocity      top set 0.0 0.0 0.0


# ------------------------ APPLY DEFORMATION --------------------------------

timestep 0.5


fix         1a all npt temp 300 300 100 x 1.0 1.0 1000 y 1.0 1.0 1000

fix         rffqeq all qeq/reax 1 0.0 10.0 1.0e-6 reax/c


velocity      bottom set NULL NULL -0.000115

velocity      top set NULL NULL 0.000115


# ------------------------ FILES FOR OVITO VISUALIZATION --------------------------------

dump              1 all custom 2000 dump.tensilef4pps_L10D6_e9.cfg mass type xs ys zs
fx fy fz vx vy vz c_peratom c_myPress[1] c_myPress[2] c_myPress[3] c_myPress[4]
c_myPress[5] c_myPress[6]
```

```
# ------------------------- THERMO TO OUTPUT VALUES ---------------------------------

thermo  200

thermo_style     custom step lx ly lz temp ke pe press pxx pyy pzz c_13 vol

thermo_modify  flush yes



run              400000
```

APPENDIX B

MD SIMULATION COMPUTATION TIME SUMMARY

TACC Simulations:

Simulations performed in CHAPTER 3 used computational resources from Texas Advanced Computing Center (TACC).

Model	Supercomputer	No. of atoms	Nodes	Cores/node	Time to run	Simulation time
CNT/Epoxy Model	Stampede2	11160	4	32	98 hrs	700 ps
CNT Pullout	Lonestar	11960	4	32	20 hrs	80 ps

INL Simulations:

Simulations performed in CHAPTER 5 and **Error! Reference source not found.** used High Performance Computing resources from Idaho National Laboratory.

Model	Supercomputer	No. of atoms	Nodes	Cores/ node	Time to run	Simulation time
Single Silica NF Tensile test (D = 6.4 nm)	Falcon	21681	7	36	24 hrs	200 ps
Paired (2) Silica NF Tensile test	Falcon	43362	13	36	18 hrs	200 ps
Paired (2) Silica NF Pullout test	Falcon	43362	13	36	48 hrs	200 ps
Silica NF Melting (D = 1.75nm, HR = 0.1 K/ps)	Sawtooth	2227	1	48	21 days	30 ns
Silica NF Melting (D = 2.85nm, HR = 0.2 K/ps)	Sawtooth	6240	3	48	20 days	17.5 ns

ACKNOWLEDGEMENTS

The authors acknowledge the Texas Advanced Computing Center (TACC) at The University of Texas at Austin for providing HPC resources that have contributed to the research results reported within Chapter 3. URL: http://www.tacc.utexas.edu

The authors would like to thank Institute for Predictive Performance Methodologies (IPPM) at The University of Texas at Arlington Research Institute (UTARI) for providing the computational resources for the work discussed in Chapter 4.

“The research work reported in Chapter 5 made use of the resources of the High Performance Computing Center at Idaho National Laboratory, which is supported by the Office of Nuclear Energy of the U.S. Department of Energy and the Nuclear Science User Facilities under Contract No. DE-AC07-05ID14517.” http://hpcweb.hpc.inl.gov/home/about#publications

REFERENCES

[1] S. Gong, Z. H. Zhu, and S. A. Meguid, “Carbon nanotube agglomeration effect on piezoresistivity of polymer nanocomposites,” *Polymer (Guildf).*, vol. 55, no. 21, pp. 5488–5499, 2014.

[2] A. Chakrabarty and T. Çağin, “Thermo-mechanical properties of a piezoelectric polyimide carbon nanotube composite: Assessment of composite theories,” *Comput. Mater. Sci.*, vol. 92, pp. 185–191, 2014.

[3] B. Hu *et al.*, “Numerical simulations on piezoresistivity of nanofiller and polymer based nanocomposites,” *ECCOMAS 2012 - Eur. Congr. Comput. Methods Appl. Sci. Eng. E-b. Full Pap.*, pp. 7162–7175, 2012.

[4] N. Koratkar, B. Q. Wei, and P. M. Ajayan, “Carbon Nanotube Films for Damping Applications,” *Adv. Mater.*, vol. 14, no. 13–14, pp. 997–1000, 2002.

[5] P. M. Ajayan, J. Suhr, and N. Koratkar, “Utilizing interfaces in carbon nanotube reinforced polymer composites for structural damping,” *J. Mater. Sci.*, vol. 41, no. 23, pp. 7824–7829, 2006.

[6] R. E. Swain, K. L. Reifsnider, K. Jayaraman, and M. El-Zein, “Interface / Interphase Concepts in Composite Material Systems,” *J. Thermoplast. Compos. Mater.*, vol. 3, no. January, pp. 13–23, 1990.

[7] S. Iijima, “Helical microtubules of graphitic carbon,” *Nature*, vol. 354, no. 6348, pp. 56–58, 1991.

[8] L. S. Schadler, S. C. Giannaris, and P. M. Ajayan, “Load transfer in carbon nanotube epoxy composites,” *Appl. Phys. Lett.*, vol. 73, no. 26, p. 3842, 1998.

[9] P. M. Ajayan, L. S. Schadler, S. C. Giannaris, and A. Rubio, “Single-walled carbon nanotube-polymer composites: Strength and weakness,” *Adv. Mater.*, vol. 12, no. 10, pp. 750–753, 2000.

[10] M. S. P. Shaffer and A. H. Windle, “Fabrication and characterization of carbon nanotube/poly(vinyl alcohol) Composites,” *Adv. Mater.*, vol. 11, no. 11, pp. 937–941, 1999.

[11] P. Sharma and P. Ahuja, “Recent advances in carbon nanotube-based electronics,” *Mater. Res. Bull.*, vol. 43, no. 10, pp. 2517–2526, 2008.

[12] H. Sun, J. Ren, and X. Qu, “Carbon Nanomaterials and DNA: From Molecular Recognition to Applications,” *Acc. Chem. Res.*, vol. 49, no. 3, pp. 461–470, 2016.

[13] M. H. Al-Saleh and U. Sundararaj, “Electromagnetic interference shielding mechanisms of CNT/polymer composites,” *Carbon N. Y.*, vol. 47, no. 7, pp. 1738–1746, 2009.

[14] S. J. V Frankland and V. M. Harik, “Analysis of carbon nanotube pull-out from a polymer matrix,” *Mater. Res. Soc. Symp. Proc.*, vol. 733 E, pp. 86–91, 2006.

[15] R. Chahal, A. Adnan, and A. Roy, “Molecular dynamics study of carbon nanotube/epoxy interfaces using ReaxFF,” in *American Society of Composites 32nd Technical Conference*, 2017.

[16] J. Gou, B. Minaie, B. Wang, Z. Liang, and C. Zhang, “Computational and experimental study of interfacial bonding of single-walled nanotube reinforced composites,” *Comput. Mater. Sci.*, vol. 31, no. 3–4, pp. 225–236, 2004.

[17] F. T. Fisher, R. D. Bradshaw, and L. C. Brinson, “Fiber waviness in nanotube-

reinforced polymer composites-I: Modulus predictions using effective nanotube properties," *Compos. Sci. Technol.*, vol. 63, no. 11, pp. 1689–1703, 2003.

[18] M. A. Bhuiyan, R. V. Pucha, J. Worthy, M. Karevan, and K. Kalaitzidou, "Understanding the effect of CNT characteristics on the tensile modulus of CNT reinforced polypropylene using finite element analysis," *Comput. Mater. Sci.*, vol. 79, pp. 368–376, 2013.

[19] R. Chahal, A. Adnan, and A. Roy, "Elastic constants of carbon nanotube reinforced polymer nanocomposites," *32nd Tech. Conf. Am. Soc. Compos. 2017*, vol. 3, no. October 2017, 2017.

[20] R. Chahal, A. Adnan, and A. Roy, "Effect of Carbon Nanotube (CNT) Waviness on Elastic Modulus of CNT/Epoxy Nanocomposites," in *American Society of Composites 34th Technical Conference*, 2019.

[21] B. C. Edwards, "Design and deployment of a space elevator," *Acta Astronaut.*, vol. 47, no. 10, 2000.

[22] A. Hadhazy, "Resetting expectations for carbon nanotubes," *Aerospace America AIAA*, pp. 30–37, Nov-2020.

[23] J. L. Reeves and B. C. Vaagensmith, "SILICA NANOFIBER MATERIALS , ARTICLES INCLUDING SUCH MATERIALS , AND RELATED METHODS," US 2019/0368638 A1, 2019.

[24] C. M. DeCusatis and C. J. Sher DeCusatis, "Fiber Optic Essentials," *Fiber Opt. Essentials*, 2006.

[25] C. R. Kurkjian, J. T. Krause, and M. J. Matthewson, "Strength and Fatigue of

Silica Optical Fibers," *J. Light. Technol.*, vol. 7, no. 9, pp. 1360–1370, 1989.

[26] J. Luo *et al.*, "Size-Dependent Brittle-to-Ductile Transition in Silica Glass Nanofibers," *Nano Lett.*, vol. 16, no. 1, pp. 105–113, 2016.

[27] S. Bonfanti, E. E. Ferrero, A. L. Sellerio, R. Guerra, and S. Zapperi, "Damage Accumulation in Silica Glass Nanofibers," *Nano Lett.*, vol. 18, no. 7, pp. 4100–4106, 2018.

[28] S. Plimpton, "Short-Range Molecular Dynamics," *J. Comput. Phys.*, vol. 117, no. 6, pp. 1–42, 1997.

[29] R. Chahal, A. Adnan, and A. Roy, "Molecular dynamics study of carbon nanotube/epoxy interfaces using ReaxFF," *Am. Soc. Compos. 32nd Tech. Conf.*, 2017.

[30] A. Chahal, R., Adnan, A., Roy, "Generating Representative Volume Element (RVE) for Finite Element Analysis of Random Fiber Composites/Nanocomposites." 2017.

[31] R. Chahal and A. Adnan, "Three - Dimensional Stochastic Modelling of Wavy Carbon Nanotube Reinforced Epoxy Nanocomposites," *Multiscale Sci. Eng.*, 2020.

[32] R. Chahal *et al.*, "Thermal Stability of Silica Nanofibers and their mats: A Molecular Dynamics and Experimental Investigation," 2021.

[33] R. Chahal, William, G. Pawar, A. Adnan, T. Ring, and B. C. Vaagensmith, "Three-dimensional Stochastic Modelling of Electrospun Silica Nanofiber Mat," 2021.

[34] R. Chahal, G. Pawar, A. Adnan, B. C. Vaagensmith, and J. Reeves, "Investigation

of the Atomic Scale Nanofiber Material Interfaces," 2021.

[35] D. C. Rapaport, *The Art of Molecular Dynamics Simulation*, 2nd ed., vol. 4, no. 1. Cambridge University Press, 2004.

[36] D. J. Evans and B. L. Holian, "The Nose–Hoover thermostat," *J. Chem. Phys.*, no. 83, pp. 4069–4074, 1985.

[37] H. J. C. Berendsen, J. P. M. Postma, W. F. Van Gunsteren, A. Dinola, and J. R. Haak, "Molecular dynamics with coupling to an external bath," *J. Chem. Phys.*, vol. 81, no. 8, pp. 3684–3690, 1984.

[38] A. C. T. Van Duin, S. Dasgupta, F. Lorant, and W. A. Goddard, "ReaxFF: A reactive force field for hydrocarbons," *J. Phys. Chem. A*, vol. 105, no. 41, pp. 9396–9409, 2001.

[39] T. P. Senftle *et al.*, "The ReaxFF reactive force-field: Development, applications and future directions," *npj Comput. Mater.*, vol. 2, no. September 2015, 2016.

[40] F. Costanzo, G. L. Gray, and P. C. Andia, "On the definitions of effective stress and deformation gradient for use in MD: Hill's macro-homogeneity and the virial theorem," *Int. J. Eng. Sci.*, vol. 43, no. 7, 2005.

[41] P. C. Andia, F. Costanzo, and G. L. Gray, "A classical mechanics approach to the determination of the stress-strain response of particle systems," *Model. Simul. Mater. Sci. Eng.*, vol. 14, no. 4, 2006.

[42] M. Zhou, "A new look at the atomic level virial stress: On continuum-molecular system equivalence," *Proc. R. Soc. A Math. Phys. Eng. Sci.*, vol. 459, no. 2037, 2003.

[43] S. Shen and S. N. Atluri, “Atomic-level stress calculation and continuum-molecular system equivalence,” *C. - Comput. Model. Eng. Sci.*, vol. 6, no. 1, 2004.

[44] E. J. Barbero, *Finite element analysis of composite materials using AbaqusTM*. Boca Raton, FL: CRC Press, 2013.

[45] F. Komuves, A. D. Kelkar, R. Mohan, and V. A. Kelkar, “Prediction of mechanical properties of EPON 862 (DGEBF) cross-linked with curing agent W (DETDA) and SWCNT using MD simulations,” in *Collection of Technical Papers - AIAA/ASME/ASCE/AHS/ASC Structures, Structural Dynamics and Materials Conference*, 2010.

[46] R. Zhu, E. Pan, and A. K. Roy, “Molecular dynamics study of the stress-strain behavior of carbon-nanotube reinforced Epon 862 composites,” *Mater. Sci. Eng. A*, vol. 447, no. 1–2, pp. 51–57, 2007.

[47] K. Liao and S. Li, “Interfacial characteristics of a carbon nanotube–polystyrene composite system,” *Appl. Phys. Lett.*, vol. 79, no. 25, p. 4225, 2001.

[48] S. C. Chowdhury and T. Okabe, “Computer simulation of carbon nanotube pull-out from polymer by the molecular dynamics method,” *Compos. Part A Appl. Sci. Manuf.*, vol. 38, no. 3, pp. 747–754, 2007.

[49] Y. Li, Y. Liu, X. Peng, C. Yan, S. Liu, and N. Hu, “Pull-out simulations on interfacial properties of carbon nanotube-reinforced polymer nanocomposites,” *Comput. Mater. Sci.*, vol. 50, no. 6, pp. 1854–1860, 2011.

[50] “MOLECULAR DYNAMICS MODEL OF CARBON NANOTUBES IN EPON 862 / DETDA POLYMER By Guttormur Arnar Ingvason A Thesis Submitted to the College of Engineering , Department of Aerospace Engineering for the partial

fulfillment of the requirements of the degree of Ma," no. December, 2013.

[51] G. M. Odegard, B. D. Jensen, S. Gowtham, J. Wu, J. He, and Z. Zhang, "Predicting mechanical response of crosslinked epoxy using ReaxFF," *Chem. Phys. Lett.*, vol. 591, pp. 175–178, 2014.

[52] L. Liu, Y. Liu, S. V. Zybin, H. Sun, and W. A. Goddard, "ReaxFF-lg: Correction of the ReaxFF reactive force field for London dispersion, with applications to the equations of state for energetic materials," *J. Phys. Chem. A*, vol. 115, no. 40, pp. 11016–11022, 2011.

[53] W. Smith, C. W. Yong, and P. M. Rodger, "DL_POLY: Application to molecular simuation," *Mol. Simul.*, vol. 28, no. 5, pp. 385–471, 2002.

[54] R. G. De Villoria, A. Miravete, J. Cuartero, A. Chiminelli, and N. Tolosana, "Mechanical properties of SWNT/epoxy composites using two different curing cycles," *Compos. Part B Eng.*, vol. 37, no. 4–5, pp. 273–277, 2006.

[55] M. R. Loos, S. H. Pezzin, S. C. Amico, C. P. Bergmann, and L. A. F. Coelho, "The matrix stiffness role on tensile and thermal properties of carbon nanotubes/epoxy composites," *J. Mater. Sci.*, vol. 43, no. 18, pp. 6064–6069, 2008.

[56] A. Montazeri, A. Khavandi, J. Javadpour, and A. Tcharkhtchi, "Viscoelastic properties of multi-walled carbon nanotube/epoxy composites using two different curing cycles," *Mater. Des.*, vol. 31, no. 7, pp. 3383–3388, 2010.

[57] L. Ci and J. B. Bai, "The reinforcement role of carbon nanotubes in epoxy composites with different matrix stiffness," *Compos. Sci. Technol.*, vol. 66, no. 3–4, pp. 599–603, 2006.

[58] A. Stukowski, “Visualization and Analysis of Atomistic Simulation Data with OVITO-the Open Visualization Tool.” Modelling and Simulation in Material Science Engineering, 2010.

[59] R. Chahal *et al.*, “Molecular dynamics for the prediction of the interfacial shear stress and interface dielectric properties of carbon fiber epoxy composites,” in *American Society of Composites 33rd Technical Conference*, 2018.

[60] C. C. Chamis, “Mechanics of Load Transfer At the Interface.,” 1972.

[61] M. Narkis, E. J. H. Chen, and R. B. Pipes, “Review of methods for characterization of interfacial fiber-matrix interactions,” *Polym. Compos.*, vol. 9, no. 4, pp. 245–251, 1988.

[62] K. Liao and S. Li, “Interfacial characteristics of a carbon nanotube-polystyrene composite system,” *Appl. Phys. Lett.*, vol. 79, no. 25, pp. 4225–4227, 2001.

[63] G. Pal and S. Kumar, “Modeling of carbon nanotubes and carbon nanotube-polymer composites,” *Progress in Aerospace Sciences*, vol. 80. Elsevier Ltd, pp. 33–58, 01-Jan-2016.

[64] S. Imani Yengejeh, S. A. Kazemi, and A. Öchsner, “Carbon nanotubes as reinforcement in composites: A review of the analytical, numerical and experimental approaches,” *Comput. Mater. Sci.*, vol. 136, pp. 85–101, 2017.

[65] Y. Liu and S. Kumar, “Polymer/carbon nanotube nano composite fibers-A review,” *ACS Appl. Mater. Interfaces*, vol. 6, no. 9, pp. 6069–6087, 2014.

[66] R. Khare and S. Bose, “Carbon Nanotube Based Composites- A Review,” *J. Miner. Mater. Charact. Eng.*, vol. 4, no. 1, pp. 31–46, 2005.

[67] J. Chen, B. Liu, X. Gao, and D. Xu, “A review of the interfacial characteristics of polymer nanocomposites containing carbon nanotubes,” *RSC Adv.*, vol. 8, no. 49, pp. 28048–28085, 2018.

[68] I. Chung and M. Cho, “Recent Studies on the Multiscale Analysis of Polymer Nanocomposites,” *Multiscale Sci. Eng.*, vol. 1, no. 3, pp. 167–195, 2019.

[69] F. T. Fisher, R. D. Bradshaw, and L. C. Brinson, “Effects of nanotube waviness on the modulus of nanotube-reinforced polymers,” *Appl. Phys. Lett.*, vol. 80, no. 24, pp. 4647–4649, 2002.

[70] S. Herasati and L. Zhang, “A new method for characterizing and modeling the waviness and alignment of carbon nanotubes in composites,” *Compos. Sci. Technol.*, vol. 100, pp. 136–142, 2014.

[71] M. A. Bhuiyan, R. V. Pucha, and K. Kalaitzidou, “3D RVE models able to capture and quantify the dispersion, agglomeration, and orientation state of CNT in CNT/PP nanocomposites,” *Front. Mater.*, vol. 3, no. February, pp. 1–13, 2016.

[72] D. Qian, E. C. Dickey, R. Andrews, and T. Rantell, “Load transfer and deformation mechanisms in carbon nanotube-polystyrene composites,” *Appl. Phys. Lett.*, vol. 76, no. 20, pp. 2868–2870, 2000.

[73] B. Natarajan *et al.*, “The Evolution of Carbon Nanotube Network Structure in Unidirectional Nanocomposites Resolved by Quantitative Electron Tomography,” *ACS Nano*, vol. 9, no. 6, pp. 6050–6058, 2015.

[74] I. Y. Stein, D. J. Lewis, and B. L. Wardle, “Aligned carbon nanotube array stiffness from stochastic three-dimensional morphology,” *Nanoscale*, vol. 7, no. 46, pp. 19426–19431, 2015.

[75] I. Y. Stein and B. L. Wardle, “Mechanics of aligned carbon nanotube polymer matrix nanocomposites simulated via stochastic three-dimensional morphology,” *Nanotechnology*, vol. 27, no. 3, 2015.

[76] I. Y. Stein and B. L. Wardle, “Packing morphology of wavy nanofiber arrays,” *Phys. Chem. Chem. Phys.*, vol. 18, no. 2, pp. 694–699, 2015.

[77] J. Jung, S. Lee, N. M. Pugno, and S. Ryu, “Orientation Distribution Dependence of Piezoresistivity of Metal Nanowire-Polymer Composite,” *Multiscale Sci. Eng.*, vol. 2, no. 1, pp. 54–62, 2020.

[78] F. Dalmas, R. Dendievel, L. Chazeau, J. Y. Cavaillé, and C. Gauthier, “Carbon nanotube-filled polymer composites. Numerical simulation of electrical conductivity in three-dimensional entangled fibrous networks,” *Acta Mater.*, vol. 54, no. 11, pp. 2923–2931, 2006.

[79] Y. Liu, “Three-dimensional visualization of carbon networks in nanocomposites,” *Nanotechnology*, vol. 26, no. 44, 2015.

[80] M. A. Bhuiyan, R. V. Pucha, and K. Kalaitzidou, “3D RVE Models Able to Capture and Quantify the Dispersion, Agglomeration, and Orientation State of CNT in CNT/PP Nanocomposites,” *Front. Mater.*, vol. 3, no. February, pp. 1–13, 2016.

[81] S. Namilae and N. Chandra, “Multiscale model to study the effect of interfaces in carbon nanotube-based composites,” *J. Eng. Mater. Technol. Trans. ASME*, vol. 127, no. 2, pp. 222–232, 2005.

[82] N. Chandra, “Cohesive Zone Approach to Multiscale Modelling of Nanotube Reinforced Composites,” 2007.

[83] F. Gou and C. Ke, “Theoretical Predictions of the Interfacial Stress Transfer in Nanotube-Reinforced Polymer Nanocomposites by Using a Strain-Hardening Shear-Lag Model,” *Multiscale Sci. Eng.*, vol. 1, no. 3, pp. 236–246, 2019.

[84] G. P. Carman and K. L. Reifsnider, “Micromechanics of short-fiber composites,” *Compos. Sci. Technol.*, vol. 43, no. 2, pp. 137–146, 1992.

[85] A. Haque and A. Ramasetty, “Theoretical study of stress transfer in carbon nanotube reinforced polymer matrix composites,” *Compos. Struct.*, vol. 71, no. 1, pp. 68–77, 2005.

[86] A. Hernández-Pérez and F. Avilés, “Modeling the influence of interphase on the elastic properties of carbon nanotube composites,” *Comput. Mater. Sci.*, vol. 47, no. 4, pp. 926–933, 2010.

[87] H. Wan, F. Delale, and L. Shen, “Effect of CNT length and CNT-matrix interphase in carbon nanotube (CNT) reinforced composites,” *Mech. Res. Commun.*, vol. 32, no. 5, pp. 481–489, 2005.

[88] J. Tsai and C. T. Sun, “Effect of Platelet Dispersion on the Load Transfer Efficiency in Nanoclay Composites,” *J. Compos. Mater.*, vol. 38, no. 7, pp. 567–579, 2004.

[89] G. P. Carman, R. C. Averill, K. L. Reifsnider, and J. N. Reddy, “Optimization of Fiber Coatings to Minimize Stress Concentrations in Composite Materials,” *J. Compos. Mater.*, vol. 27, no. 6, pp. 589–612, 1993.

[90] A. Adnan, C. T. Sun, and H. Mahfuz, “A molecular dynamics simulation study to investigate the effect of filler size on elastic properties of polymer nanocomposites,” *Compos. Sci. Technol.*, vol. 67, no. 3–4, pp. 348–356, 2007.

[91] G. M. Odegard, T. C. Clancy, and T. S. Gates, “Modeling of the mechanical properties of nanoparticle/polymer composites,” *Polymer (Guildf).*, vol. 46, no. 2, pp. 553–562, 2005.

[92] M. S. Radue and G. M. Odegard, “Multiscale modeling of carbon fiber/carbon nanotube/epoxy hybrid composites: Comparison of epoxy matrices,” *Compos. Sci. Technol.*, vol. 166, pp. 20–26, 2018.

[93] Y. Li and G. D. Seidel, “Multiscale modeling of the interface effects in CNT-epoxy nanocomposites,” *Comput. Mater. Sci.*, vol. 153, no. February, pp. 363–381, 2018.

[94] M. A. Bhuiyan, R. V. Pucha, J. Worthy, M. Karevan, and K. Kalaitzidou, “Defining the lower and upper limit of the effective modulus of CNT/polypropylene composites through integration of modeling and experiments,” *Compos. Struct.*, vol. 95, pp. 80–87, 2013.

[95] M. A. Bhuiyan, R. V. Pucha, M. Karevan, and K. Kalaitzidou, “Tensile modulus of carbon nanotube/polypropylene composites - A computational study based on experimental characterization,” *Comput. Mater. Sci.*, vol. 50, no. 8, pp. 2347–2353, 2011.

[96] T. Mori and K. Tanaka, “Average stress in matrix and average elastic energy of materials with inclusions misfitting,” *Acta Metall.*, vol. 21, no. 5, pp. 571–574, 1394.

[97] T. Mura, *Micromechanics of defects in solids*. The Hague: Martinus Nijhoff, 1982.

[98] K. Yanase, S. Moriyama, and J. W. Ju, “Effects of CNT waviness on the effective elastic responses of CNT-reinforced polymer composites,” vol. 1364, pp. 1351–

1364, 2013.

[99] F. T. Fisher, R. D. Bradshaw, and L. C. Brinson, “Effects of nanotube waviness on the modulus of nanotube-reinforced polymers,” *Appl. Phys. Lett.*, vol. 80, no. 24, pp. 4647–4649, 2002.

[100] N. F. Dow, “STUDY OF STRESSES NEAR A DISCONTINUITY IN A FILAMENT-REINFORCED COMPOSITE METAL,” Space Mechanics Memo. 102, General Electric Space Sciences Lab, 1963.

[101] O. Kallmes and H. Corte, “Statistical Geometry of a Fibrous Network,” *Tappi J.*, vol. 43, no. 9, pp. 737–752, 1960.

[102] J. L. Worthy III, “DESIGN TOOL FOR SIMULATION OF NANOCOMPOSITE MATERIAL PROPERTIES,” Thesis (Undergraduate Research), Georgia Institute of Technology, 2013.

[103] W. Patterson and A. Force, “The Halpin-Tsai Equations: A Review,” vol. 16, no. 5, 1976.

[104] P. Papanikos, D. D. Nikolopoulos, and K. I. Tserpes, “Equivalent beams for carbon nanotubes,” *Comput. Mater. Sci.*, vol. 43, no. 2, pp. 345–352, 2008.

[105] A. Martone, C. Formicola, M. Giordano, and M. Zarrelli, “Reinforcement efficiency of multi-walled carbon nanotube/epoxy nano composites,” *Compos. Sci. Technol.*, vol. 70, no. 7, pp. 1154–1160, 2010.

[106] I. O’Connor, H. Hayden, S. O’Connor, J. N. Coleman, and Y. K. Gun’ko, “Polymer reinforcement with kevlar-coated carbon nanotubes,” *J. Phys. Chem. C*, vol. 113, no. 47, pp. 20184–20192, 2009.

[107] “Scan2CAD.” .

[108] A. Matveeva, V. Romanov, S. Lomov, and L. Gorbatikh, “Application of the embedded element technique to the modelling of nano-engineered fiber-reinforced composites,” *ICCM Int. Conf. Compos. Mater.*, vol. 2015-July, no. July, pp. 19–24, 2015.

[109] E. T. Thostenson and T. W. Chou, “Erratum: On the elastic properties of carbon nanotube-based composites: Modelling and characterization (J. Phys. D: Appl. Phys. 36 2003 (573)),” *J. Phys. D. Appl. Phys.*, vol. 47, no. 7, 2014.

[110] H. W. Wang, H. W. Zhou, R. D. Peng, and L. Mishnaevsky, “Nanoreinforced polymer composites: 3D FEM modeling with effective interface concept,” *Compos. Sci. Technol.*, vol. 71, no. 7, pp. 980–988, 2011.

[111] H. Tsai and J. L. Kardos, “The Halpin-Tsai Equations,” *Polym. Eng. Sci.*, vol. 16, no. 5, 1976.

[112] R. E. Lavengood and L. A. Goettler, “Stiffness of non-aligned fiber reinforced composites,” U.S. Government R&D Reports, AD886372, National Technical Information Service, Springfield, Virginia, 1971.

[113] L. E. Nielsen, “Generalized Equation for the Elastic Moduli of Composite Materials,” *J. Appl. Phys.*, vol. 41, no. 11, p. 4626, 1970.

[114] S. Deogekar and R. C. Picu, “On the strength of random fiber networks,” *J. Mech. Phys. Solids*, vol. 116, pp. 1–16, 2018.

[115] I. I. Slowing, B. G. Trewyn, S. Giri, and V. S. Y. Lin, “Mesoporous silica nanoparticles for drug delivery and biosensing applications,” *Adv. Funct. Mater.*,

vol. 17, no. 8, pp. 1225–1236, 2007.

[116] P. Wang, S. M. Zakeeruddin, P. Comte, I. Exnar, and M. Grätzel, “Gelation of ionic liquid-based electrolytes with silica nanoparticles for quasi-solid-state dye-sensitized solar cells,” *J. Am. Chem. Soc.*, vol. 125, no. 5, pp. 1166–1167, 2003.

[117] M. Yanilmaz, Y. Lu, J. Zhu, and X. Zhang, “Silica/polyacrylonitrile hybrid nanofiber membrane separators via sol-gel and electrospinning techniques for lithium-ion batteries,” *J. Power Sources*, vol. 313, pp. 205–212, 2016.

[118] F. Erogbogbo, K. T. Yong, I. Roy, G. X. Xu, P. N. Prasad, and M. T. Swihart, “Biocompatible luminescent silicon quantum dots for imaging of cancer cells,” *ACS Nano*, vol. 2, no. 5, pp. 873–878, 2008.

[119] F. T. Wallenberger and P. A. Bingham, “Fiberglass and Glass Technology,” *Fiberglass Glas. Technol.*, 2010.

[120] N. R. Keskar and J. R. Chelikowsky, “Structural properties of nine silica polymorphs,” *Phys. Rev. B*, vol. 46, no. 1, pp. 1–13, 1992.

[121] N. R. Keskar and J. R. Chelikowsky, “Calculated thermodynamic properties of silica polymorphs,” *Phys. Chem. Miner.*, vol. 22, no. 4, pp. 233–240, 1995.

[122] M. Schaible, *Empirical molecular dynamics modeling of silicon and silicon dioxide: A review*, vol. 24, no. 4. 1999.

[123] A. A. Griffith, “The phenomena of rapture and flow in soilds,” *Philosophical Transactions of the Royal Society of London*, vol. 221. pp. 163–198, 1920.

[124] S. C. Chowdhury, B. Z. (Gama. Haque, and J. W. Gillespie, “Molecular dynamics simulations of the structure and mechanical properties of silica glass using

ReaxFF," *J. Mater. Sci.*, vol. 51, no. 22, pp. 10139–10159, 2016.

[125] H. Ni, X. Li, and H. Gao, "Elastic modulus of amorphous SiO 2 nanowires," *Appl. Phys. Lett.*, vol. 88, no. 4, pp. 1–3, 2006.

[126] E. C. C. M. Silva, L. Tong, S. Yip, and K. J. Van Vliet, "Size effects on the stiffness of silica nanowires," *Small*, vol. 2, no. 2, pp. 239–243, 2006.

[127] F. Yuan and L. Huang, "Size-dependent elasticity of amorphous silica nanowire: A molecular dynamics study," *Appl. Phys. Lett.*, vol. 103, no. 20, pp. 10–15, 2013.

[128] C. Tang and L. P. Dávila, "Anomalous surface states modify the size-dependent mechanical properties and fracture of silica nanowires," *Nanotechnology*, vol. 25, no. 43, 2014.

[129] C. Zhang, F. Duan, and Q. Liu, "Size effects on the fracture behavior of amorphous silica nanowires," *Comput. Mater. Sci.*, vol. 99, pp. 138–144, 2015.

[130] L. P. Dávila, V. J. Leppert, and E. M. Bringa, "The mechanical behavior and nanostructure of silica nanowires via simulations," *Scr. Mater.*, vol. 60, no. 10, pp. 843–846, 2009.

[131] H. Liang, M. Upmanyu, and H. Huang, "Size-dependent elasticity of nanowires: Nonlinear effects," *Phys. Rev. B - Condens. Matter Mater. Phys.*, vol. 71, no. 24, pp. 1–4, 2005.

[132] H. S. Park, W. Cai, H. D. Espinosa, and H. Huang, "Mechanics of crystalline nanowires," *MRS Bull.*, vol. 34, no. 3, pp. 178–183, 2009.

[133] R. C. Picu, "Mechanics of random fiber networks - A review," *Soft Matter*, vol. 7, no. 15, pp. 6768–6785, 2011.

[134] A. Buldum and J. P. Lu, “Modeling and simulations of carbon nanotubes and their junctions on surfaces,” *Appl. Surf. Sci.*, vol. 219, no. 1–2, pp. 123–128, 2003.

[135] A. C. T. Van Duin, A. Strachan, S. Stewman, Q. Zhang, X. Xu, and W. A. Goddard, “ReaxFFSiO reactive force field for silicon and silicon oxide systems,” *J. Phys. Chem. A*, vol. 107, no. 19, pp. 3803–3811, 2003.

[136] J. C. Fogarty, H. M. Aktulga, A. Y. Grama, A. C. T. Van Duin, and S. A. Pandit, “A reactive molecular dynamics simulation of the silica-water interface,” *J. Chem. Phys.*, vol. 132, no. 17, 2010.

[137] A. Adnan and C. T. Sun, “Effect of surface morphology and temperature on the structural stability of nanoscale wavy films,” *Nanotechnology*, vol. 19, no. 31, 2008.

[138] P. Pawlow, “Ueber den Einfluß der Oberfläche einer festen Phase auf die latente Wärme und die Temperatur des Schmelzens,” *Zeitschrift für Chemie und Ind. der Kolloide*, vol. 7, no. 1, pp. 37–39, 1910.

[139] W. H. Moon, H. J. Kim, and C. H. Choi, “Molecular dynamics simulation of melting behavior of GaN nanowires,” *Scr. Mater.*, vol. 56, no. 5, pp. 345–348, 2007.

[140] J. Zhang *et al.*, “Molecular dynamics simulation of the melting behavior of copper nanorod,” *Comput. Mater. Sci.*, vol. 143, pp. 248–254, 2018.

[141] J. W. Kang and H. J. Hwang, “Molecular dynamics simulation study of the melting of ultra-thin copper nanowires,” *J. Korean Phys. Soc.*, vol. 40, no. 5, pp. 946–948, 2002.

[142] A. B. Belonoshko, “Molecular dynamics of MgSiO3 perovskite at high pressures:

Equation of state, structure, and melting transition," *Geochim. Cosmochim. Acta*, vol. 58, no. 19, pp. 4039–4047, 1994.

[143] A. B. Belonoshko, N. V. Skorodumova, A. Rosengren, and B. Johansson, "Melting and critical superheating," *Phys. Rev. B - Condens. Matter Mater. Phys.*, vol. 73, no. 1, pp. 1–3, 2006.

[144] A. B. BELONOSHKO and L. S. DUBROVINSKY, "Molecular dynamics of stishovite melting," *Gecchimica Cosmochim. Acta*, vol. 59, no. 9, pp. 1883–1889, 1995.

[145] J. Sun, P. Liu, M. Wang, and J. Liu, "Molecular Dynamics Simulations of Melting Iron Nanoparticles with/without Defects Using a Reaxff Reactive Force Field," *Sci. Rep.*, vol. 10, no. 1, pp. 1–11, 2020.

[146] Y. Jing, Q. Meng, and W. Zhao, "Molecular dynamics simulations of the tensile and melting behaviours of silicon nanowires," *Phys. E Low-Dimensional Syst. Nanostructures*, vol. 41, no. 4, pp. 685–689, 2009.

[147] H. M. Aktulga, J. C. Fogarty, S. A. Pandit, and A. Y. Grama, "Parallel reactive molecular dynamics: Numerical methods and algorithmic techniques," *Parallel Comput.*, vol. 38, no. 4–5, pp. 245–259, 2012.

[148] A. Allouche, "Software News and Updates Gabedit — A Graphical User Interface for Computational Chemistry Softwares," *J. Comput. Chem.*, vol. 32, pp. 174–182, 2012.

[149] R. Brückner, "Properties and structure of vitreous silica. I," *J. Non. Cryst. Solids*, vol. 5, no. 2, pp. 123–175, 1970.

[150] J. Yeon and A. C. T. Van Duin, “ReaxFF Molecular Dynamics Simulations of Hydroxylation Kinetics for Amorphous and Nano-Silica Structure, and Its Relations with Atomic Strain Energy,” *J. Phys. Chem. C*, vol. 120, no. 1, pp. 305–317, 2016.

[151] F. Yuan and L. Huang, “Size-dependent elasticity of amorphous silica nanowire: A molecular dynamics study,” *Appl. Phys. Lett.*, vol. 103, no. 20, 2013.

[152] K. Zheng *et al.*, “Electron-beam-assisted superplastic shaping of nanoscale amorphous silica,” *Nat. Commun.*, vol. 1, no. 3, 2010.

[153] W. G. Hoover, “Canonical dynamics: Equilibrium phase-space distributions,” *Phys. Rev. A*, vol. 31, no. 3, 1985.

[154] P. Vashishta *et al.*, “Million atom molecular dynamics simulations of materials on parallel computers,” *Curr. Opin. Solid State Mater. Sci.*, vol. 1, no. 6, pp. 853–863, 1996.

[155] T. P. Swiler, J. H. Simmons, and A. C. Wright, “Molecular dynamics study of brittle fracture in silica glass and cristobalite,” *J. Non. Cryst. Solids*, vol. 182, no. 1–2, pp. 68–77, 1995.

[156] K. Muralidharan, K. D. Oh, P. A. Deymier, K. Runge, and J. H. Simmons, “Molecular dynamics simulations of atomic-level brittle fracture mechanisms in amorphous silica,” *J. Mater. Sci.*, vol. 42, no. 12, pp. 4159–4169, 2007.

[157] A. Pedone, G. Malavasi, M. Cristina Menziani, U. Segre, and A. N. Cormack, “Molecular dynamics studies of stress-strain behavior of silica glass under a tensile load,” *Chem. Mater.*, vol. 20, no. 13, pp. 4356–4366, 2008.

[158] A. P. Thompson, S. J. Plimpton, and W. Mattson, “General formulation of

pressure and stress tensor for arbitrary many-body interaction potentials under periodic boundary conditions,” *J. Chem. Phys.*, vol. 131, no. 15, 2009.

[159] F. Yuan and L. Huang, “Molecular dynamics simulation of amorphous silica under uniaxial tension: From bulk to nanowire,” *J. Non. Cryst. Solids*, vol. 358, no. 24, pp. 3481–3487, 2012.

[160] G. Brambilla and D. N. Payne, “The ultimate strength of glass silica nanowires,” *Nano Lett.*, vol. 9, no. 2, pp. 831–835, 2009.

[161] L. F. Richardson, “The Approximate Arithmetical Solution by Finite Differences of Physical Problems Involving Differential Equations, with an Application to the Stresses in a Masonry Dam,” *Philos. Trans. R. Soc. A*, vol. 210, no. 459–470, pp. 307–357, 1911.

[162] P. Jutzi and U. Schubert, *Silicon Chemistry: From the Atom to Extended Systems*. Wiley-VCH: Weinheim and Cambridge, 2003.

BIOGRAPHICAL INFORMATION

Rajni Chahal was born on October 26, 1992 in Punjab, India. She spent her childhood in her hometown and finished her high-school education from Sant Sarwan Dass Model School, Phagwara in Punjab. In 2011, she moved to Jalandhar, Punjab to attend Dr. B.R. Ambedkar National Institute of Technology (NIT), Jalandhar, which is considered one of the top engineering institutes in India. In June 2015, she earned bachelor's in technology in Mechanical Engineering from NITJ. Thereafter, in Fall 2015, she joined The University of Texas at Arlington (UTA) to earn a Master's in Aerospace engineering. She joined the Multiscale Science and Engineering Lab (MMPL) in March 2016 to pursue her master's thesis under the supervision of Dr. Ashfaq Adnan. Later in Fall 2016, she converted her program to Doctorate in Aerospace engineering. The work performed on the Multiscale Modelling of Carbon Nanotube/Epoxy Nanocomposites has been continued since March 2016. In June 2019, she joined Idaho National Laboratory (INL) as a Graduate Research Intern and started working on the second part of this study on Multiscale Stochastic Modelling of Electrospun Silica Nanofiber Network/Mat. After January 2020, this study was continued at UTA as part of sub-contract provided by INL. This study was mentored by Dr. Adnan, Dr. Gorakh Pawar and Dr. Bjorn Vaagensmith. The details of the subject matter from both the studies are contained in this dissertation.